Comprehensive Control Strategies for a Seven Degree of Freedom Upper Limb Exoskeleton Targeting Stroke Rehabilitation

Levi Makaio Miller

A dissertation submitted in partial fulfillment of
the requirements for the degree of

Doctor of Philosophy

University of Washington

2012

Reading Committee:

Jacob Rosen, Chair

Blake Hannaford

Martin Berg

Duane Storti

Program Authorized to Offer Degree:
Mechanical Engineering

University of Washington

Abstract

Comprehensive Control Strategies for a Seven Degree of Freedom Upper Limb Exoskeleton Targeting Stroke Rehabilitation

Levi Makaio Miller

Chair of the Supervisory Committee:
Professor Jacob Rosen
Computer Engineering

In this dissertation control algorithms are developed and tested for the EXO-UL7 towards a control strategy for stroke rehabilitation. EXO-UL7 is a seven degree of freedom (Dof) powered upper limb exoskeleton that was initially designed at the University of Washington and further refined at the University of California Santa Cruz. Admittance control, swivel angle prediction and neural control of the device have been implemented and subjects tested performance of the device and control strategy. After an initial summery of the state of the art and details of the existing system. Each control strategy and performance from testing is explored.

Admittance control uses force sensors on EXO-UL7 to control the movement of the device by moving in the direction that user pressed on the device. Because EXO-UL7 is a redundant manipulator and supports the entire configuration of the arm, a single force sensor on the device end effector is not enough to fully define the movement. Additional force sensors on the device that are located at each attachment point of the machine interface allows for the full configuration of the device to be specified. This turns the under defined problem into an over defined problem (too many force signals for the number of Dof). Two strategies are developed to project the signals onto a seven degree subspace. The first adds the force vectors in task space then uses

the Inverse kinematics to develop joint trajectories. The second uses the Jacobian transpose to map the forces first to instantaneous joint torques. Then the torques are added in joint space and finally joint trajectories are developed from joint torques. Six subjects performed a peg in hole experiment and it was found that task based admittance control had about 11% lower interaction energy required to do the task. It was also shown that with both admittance controllers the subjects did the tasks slower than with no control at all. Kinematic and dynamic constraints reduced the bandwith of the system. To improve the bandwith, predictive algorithms are employed.

Swivel angle prediction is the first predictive algorithm implements to improve the performance of the device. With this control strategy the configuration of the redundant space is related to the end effector position. by observing human behavior it was noted that one of the fundamental task preformed by the human arm was to bring food to the mouth. By maximizing the manipulability of the device in the direction of the mouth, a simple stable closed form prediction of the configuration of the device was achived. Comparing movement from motion capture to predicted motion showed a good correlation and testing of the algorithm on the exoskeleton device was conducted. 4 subjects conducted a peg in hole task. An 11.22% reduction of interaction energy was achieved when compared to Admittance control alone. This algorthm can be used for motion folowwing as in the current set up, or to predict what the arm configuration should be when working with disabled populations. Although this method predicted motion very well, it only provided prediction of the one Dof redundant space of the arm.

To further extend the prediction capability and motion following of the device, neural control was implemented in which electro-myography (EMG) is used to read the nerve impulses to the muscle. Although this signal only relates muscle force to isometric muscle contraction, using other system parameters read from Exo-UL7 such

as the joint, position and velocity, a Hill based muscle model predicts the muscle force and ultimately the muscle torque. Due to an inherent delay between when the nerve impulse can first be detected and when the muscle contracts (somewhere on the order of 50-100 ms) the motion can be predicted before the arm begins to move. The model has many variables that need to be predicted for each individual so before each subject test an parameter fitting is conducted. Four subjects preformed a peg-in-hole test. It was shown that the interaction power increased compared to admittance control, but the completion time decreased. With further examination it was noted that the interaction force and energy when using the neural control was the same as with the admittance control. This implies that with the same force we achieved a higher velocity, which means that the system had a higher overall gain. The performance gains were not uniform through out all the subjects. The parameter fit conducted for each subject did not guarantee convergence to even a local minimum and there are still opportunities to improve the system performance.

Admittance control did a good job of motion following and neural and swivel prediction improved upon this control scheme. There is still further work to be done on the system. Currently using the systems that were built in this dissertation, a clinical trial for stroke rehabilitation is under way at the University of California San Francisco.

TABLE OF CONTENTS

Page

LIST OF FIGURES

Figure Number Page

LIST OF TABLES

Table Number Page

Chapter 1

INTRODUCTION

Integrating capabilities of humans and robotic-machines into a unified system offers numerous opportunities for developing a new generation of assistive technology. Potential applications could benefit members of both healthy and disabled populations. For many physical tasks, human performance is limited by muscle strength. Similarly, muscle weakness is the primary cause of disability for persons with a variety of neuromuscular diseases including stroke, spinal cord injury, muscular dystrophies, and other neuro-degenerative disorders. Opposite this limitation in muscular strength, humans possess specialized and complex algorithms for control of movement, involving both higher and lower neural centers. These algorithms enable humans to perform very complicated tasks such as locomotion and arm movement, while at the same time avoiding object collisions. In contrast, robotic manipulators can be designed to perform tasks requiring large forces or moments, depending on their structure and on the power of their actuators. However, the control algorithms that govern their dynamics lack the flexibility to perform in a wide range of conditions while preserving the same quality of performance as humans. It seems therefore that combining these two entities, the human and the robot, into one integrated system under the control of the human, may lead to a solution which will benefit from the advantages of each subsystem. The mechanical power of the machine, integrated with the inherent human control system, could allow efficient performance of tasks requiring higher forces than the human could otherwise produce. At the heart of this human-machine integration lie two fundamental scientific and technological issues: (i) the exoskeleton (orthotic device) mechanism itself and its biomechanical integration with the human body, and (ii) the human machine interface (HMI). These two key issues will determine the quality of the integration between the human and the exoskeleton in terms of how natural it will be for the operator to control the exoskeleton device as a biological extension of his/her body.

With an exoskeleton device it is possible to track motion of the user as well as influence their motion by application of forces to the user's body. Additionally, the device can apply forces to the environment. This type of device has the potential to be very advantageous for a disabled population, both as a device for assessment and treatment, as well as an assistive device for daily living. This potential can only be achieved if both the interface for the device and control allow for the user to easily and naturally control the device.

1.1 Background

Throughout the last several decades, different designs of exoskeletons for human power amplification have been developed and evaluated. In studying the evolution of these systems, some basic types with different Human Machine Interfaces (HMI) seem to emerge, which may be defined as generations. The first exoskeleton generation was developed based on the mission profile of the US Department of Defense that defined the exoskeleton as a powered suit to augment the lifting and carrying capabilities of soldiers. It was originally named man-amplifier. The primary intent was to develop a system that would greatly increase the strength of a human operator while maintaining human control of the manipulator. The first generation prototype, known as Hardiman, was the first attempt to mechanically design a man-amplifying exoskeleton using a hydraulically powered articulating frame worn by an operator [59, 10, 11, 54]. The position-controlled architecture led to poor responsiveness and instability. The second generation of exoskeletons placed the HMI at the dynamics level, utilizing the direct contact forces (measured by force sensors) between the human and the machine as the main command signals to the exoskeleton. The human wore the extender, in a way that linked them together mechanically. The operator was in full physical contact with the exoskeleton throughout its manipulation [92, 39, 40, 37, 38, 36, 78]. Several experimental extender prototypes were designed and built in order to study issues associated with this mode of control. The third generation placed the interface at the neuromuscular level, e.g., surface electromyography (sEMG) [73, 74]; and forth generations devices placed the control directly with the brain, e.g., noninvasive electroencephalogram (EEG) or invasive action potential signal measured directly from the motor cortex [16].

The third generation of interfaces uses the the body's own signals as a primary control input for the system. There exists an electromechanical delay (EMD) from when these signals can first be detected to when the muscle actually begins to contract. This delay gives time for the controller to predict the motion that will be created by the muscle contraction and move the device with the user rather then reacting to the user's movements as with other methods (e.g., kinematic and dynamic interfaces). If the EMD can be exploited in the control algorithm of the exoskeleton, a noninvasive and seamless integration between the human operator and the exoskeleton can be achieved in such a way that the device becomes a natural extension of the operators own body. Third generation scheme will be used to develop an exoskeleton control system used for stroke rehabilitation.

The rehabilitation-induced recovery of motor function in chronic stroke patients has attracted great interest due to its importance for the patient's quality of life[32][31]. Recent improvement in brain mapping techniques such as TMS, PET, and fMRI give researchers the tools needed to have a deeper understanding of the brain's plasticity. The most interesting and important result from this line of research is that injury-related motor cortex reorganization in patients can be significantly affected by post-stroke motor experience durring the chronic stroke phase[70][71]. Choosing the appropriate types of rehabilitative training administered after stroke can improve the plasticity of the brain. The proper intervention strategies based on sound motor recovery can provide maximal recovery with chronic stroke patients [32][31][71][9].

Recently the advent of robot-assisted rehabilitation treatment has shown that the robotic system can be a useful tool for the patients suffering from a wide spectrum of neuromuscular disorders such as stroke, spinal cord injury, and muscular dystrophy[67][62][47][91]. The MIT-MANUS[47, 46] is possibly one of the most successful rehabilitation robots and is widely used in clinical research. Considering a safe, stable and compliant operation for the patient suffering neuromuscular diseases [47], MANUS adopted backdrivable hardware and impedance control as distinguishing features of the robot control system. At the University of Leeds, UK, iPAM a duel robotic system is used where two, six DoF robots support the arm, with one an attachment point at the upper arm and the other at the lower arm. Each attachment point has 3 active translational degrees of freedom and 3 passive rotational degrees. [14, 15, 29, 30]. Both the MIT-MANUS and iPAM are non anthropomorphic in there operation, several other systems have been developed using an anthropomorphic exoskeleton architecture.

ARMin is an exoskeleton developed by ETH Zurich and The University Zurich. There have been several prototypes of ARMin with it supporting seven DoF operation since the second prototype[62]. This robot provides a visual, acoustic and haptic interfaces together with cooperative control strategies to facilitate the patient's active participation in a game. The robot has a simple passive gravity compensation schemes and supports unilateral types of therapy [62]. The length of the upper arm, the lower arm, the hand and the height of the device are adjustable for the different patients. For easy access to the rehabilitation site a patient can approach to the system while sitting in a wheel chair.

Pneu-WREX is an six DoF exoskeleton robot developed in UC Irvine. This robotic system adopted pneumatic actuators[68, 86]. Although the pneumatic actuator is harder to control due to its non-linear characteristics, it produces relatively large forces with a low on-board weight[53]. The robot interacts with the virtual-reality game T-WREX based on a Java Therapy 2.0 software system[86]. Another distinguishing feature of this robot its assist-as-needed control scheme[68, 86]. In this adaptive control scheme, the controller detects the patient's intention so that only a small amount of assistance is applied to the patient during therapy.

Arizona State University researchers developed a robotic arm, RUPERT (Robotic Upper Extremity Repetitive Therapy) targeting cost-effective and light weight stroke patient rehabilitation[26, 25]. The device provides the patient with assistive force to facilitate fluid and natural arm movement essential for the activities of daily living. The controller for the pneumatic muscles can be programmed for each user to improve their arm and hand flexibility as well as strength by providing a repetitive exercise pattern.

Many other systems exist for robotic assisted therapy [24, 88, 22]. Regardless of the successful work in many of the research area, there are a few areas that still need to be explored:(1) to the best of our knowledge there is no seven DOF upper limb exoskeleton robot developed to provide bilateral as well as unilateral movement training, (2) the assistive control schemes in the rehabilitation program do not consider the redundant nature of human arm motion and (3) there is no objective evaluation metric that can measure the rehabilitation progress on a fine-scale. At the University of Washington and University of California Santa Cruz, a 7 Dof exoskeleton, EXO-UL7, was developed to address these issues [76, 57, 66, 64, 75, 67, 65, 58, 42, 41]. This system is the hardware platform used to develop control algorithms described in this work.

1.2 Human Upper Limb Model

The upper limb is composed of segments linked by articulations with multiple degrees of freedom. It is a complex structure that is made up of both ridged bone and soft tissue. This soft tissue moves and slides relative to the the bone during movements and interactions with the environment. Additionally, muscle contractions cause changes to their shape and the over all stiffness of the arm. Although much of the complexity of the soft tissue is difficult to model, the overall arm movement can be represented by a much simpler model composed of ridge links connected by joints.

Three ridged segments, consisting of the upper arm, lower arm and hand connected by frictionless joints make up the simplified model of the human arm. Placing a reference frame at the shoulder, the upper arm and torso are rigidly attached by a ball and socket joint. This joint is responsible for shoulder abduction-adduction (abd-add), shoulder flexion-extension (flx-ext) and shoulder internal-external (int-ext) rotation. The upper and lower arm segments are attached by a single rotational joint at the elbow, creating elbow flx-ext. Finally, the lower arm and hand are connected by a three axis spherical joint resulting in pronation-supination (pron-sup), wrist flx-ext, and wrist radial-ulnar (rad-uln) deviation.

Korein [45] was one of the first to study this seven DOF model for the human arm. Since then, many other researches have used it to study human arm movement for computer graphics [33] [49], redundant robots [28], upper limb exoskeletons [66] [67] [75] [81], biomechanics [83] [90] [89], and much more. The seven DOF model does neglects translational and rotational motion of the scapula and clavicle, for this reason, others have used five [13] or even seven DOF [55] models of the shoulder resulting in nine and eleven DOF models of the arm. The seven DOF arm model gives a good combination of motion accuracy while reducing the model complexity to a manageable level. This model of the arm is a redundant model. Knowing the position and orientation of the hand is not enough to fully constrain the configuration of the arm, an additional degree of freedom is need to fully constrain the arm. This redundant degree will be discussed in section 1.4.

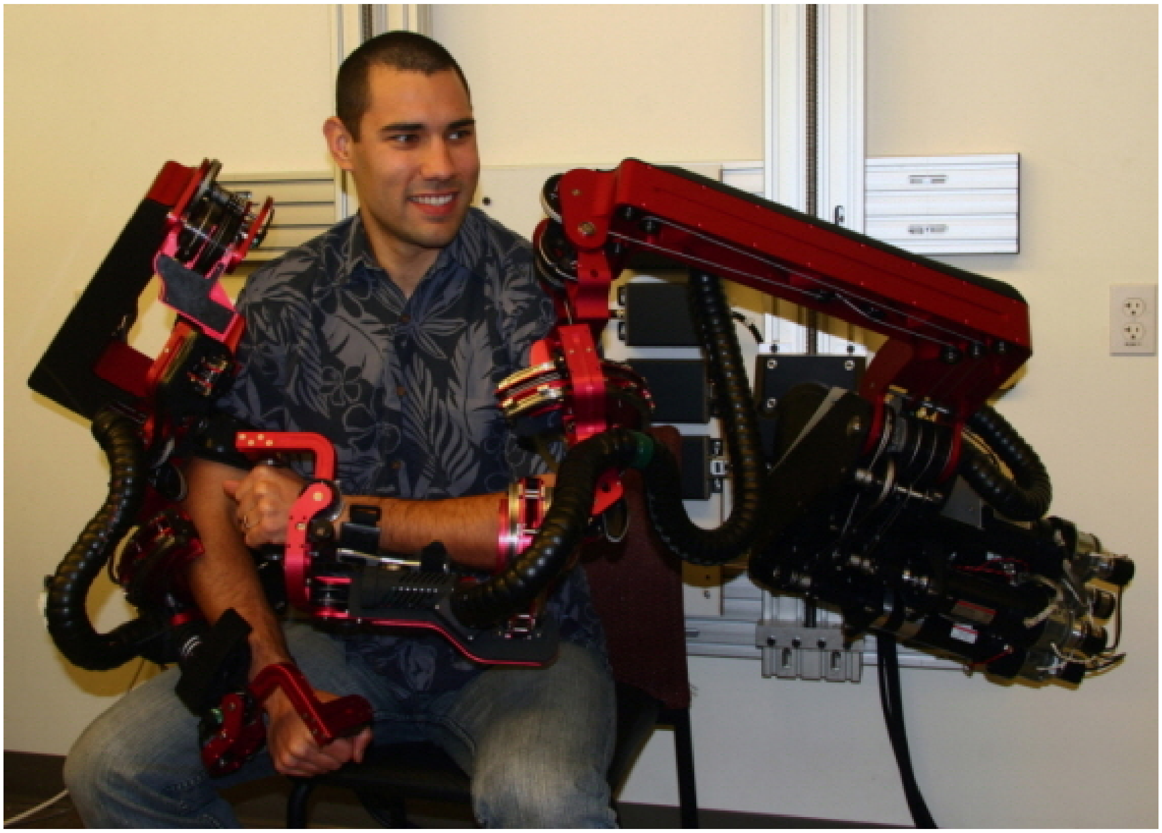

Figure 1.1: The seven degree of freedom exoskeleton supports 99% of the ranges of motion required to preform daily activities

1.3 Exoskeleton Design

The design of the exoskeleton is driven by its role as an externally worn device. It is a seven DOF open chain articulated arm. The seven degrees of freedom match each DOF of the human arm: three DOF at the shoulder, one DOF at the elbow, and three at the wrist. The kinematics and dynamics of the human arm during activities of daily living (ADL) were studied in part to determine the engineering specifications for the exoskeleton design [Fig. 1.1][76]. Using these specification, two exoskeletons were developed, each including seven DOFs. Each exoskeleton arm is actuated by seven DC brushed motors (Maxon) that transmit the appropriate torque to each joint utilizing a cable based transmission. The mechanisms are attached to a frame mounted on the wall, which allows both height and distance between the arms to be adjusted. Articulation of the exoskeleton is achieved about seven single axis revolute joints: One for each shoulder abd-add, shoulder flx-ext, shoulder int-ext rotation, elbow flx-ext, forearm pron-sup, wrist flx-ext, and wrist rad-uln deviation. The exoskeleton joints are labeled 1 through 7 from proximal to distal in the order shown in Fig. 1.2. With seven joint rotations, there is one redundant degree of freedom. This redundant degree is the same as the human arm model and will be discussed in section 1.4.

The fundamental principal in designing the exoskeleton joints is to align the rotational axis of the exoskeleton with the anatomical rotations axes. If more then one axis is at a particular anatomical joint (e.g. shoulder and wrist) the exoskeleton joints emulate the anatomical joint interaction at the center of the anatomical joint. Consistent with other work, the glenohumeral (G-H) joint is modelled as a spherical joint composed of three intersection axes [17]. The elbow modelled by a single axis orthogonal to the third shoulder axis, with a joint stop to preventing hyperextension. Exoskeleton pron-sup takes place between the elbow and the wrist as it does in the physiological mechanism. And finally, two intersecting orthogonal axes represent the

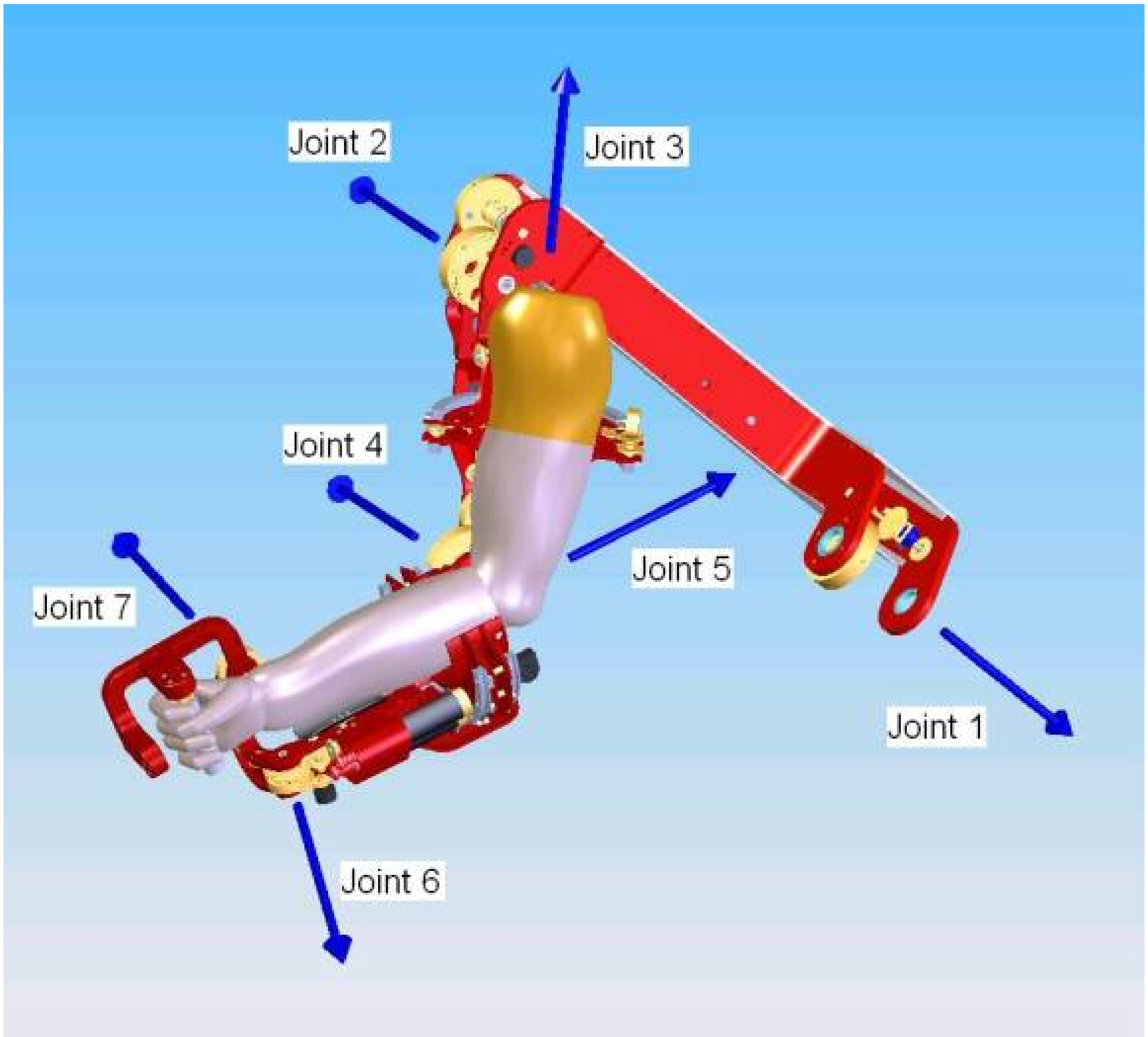

Figure 1.2: Exoskeleton axes assignment relative to the human arm. Positive rotations about each joint produce the following motion 1) combined flx/adb, 2) combined flx/add, 3) int rotation, 4) elbow flx, 5) forearm pron, 6)wrist ext, and 7) wrist rad dev.

wrist. Comparing the range of motion of the exoskeleton shows that the exoskeletons joints support 99% of the ranges of motion required to perform daily activities [67].

A result of representing the ball and socket joint of the shoulder as three intersecting joins, is the introduction of singularities that are not present in the human arm model. A significant consideration in exoskeleton design is placement of singularities [75]. A singularity is a device configuration where a DOF is lost or compromised as a result of the alignment of two rotational axes. In the development of a three DOF spherical joint, the existence or nonexistence of singularities will depend entirely on the desired reachable workspace. Spherical work-spaces equal to or larger than a hemisphere will always contain singular positions. The challenge is to place the singularity in an unreachable, or near-unreachable location, such as the edge of the workspace. For the exoskeleton arm, singularities occur when joints 1 and 3 or joints 3 and 5 align. To minimize the frequency of this occurrence, the axis of joint 1 is positioned such that singularities with joint 3 take place only at locations that are anthropometrically hard to reach. For the placement shown in Fig. 1.3(a), the singularity can be reached through simultaneous extension and abduction of the upper arm by 47.5° and 53.6° respectively [Fig. 1.3(b)]. Similarly, the same singularity can be reached through flexion and adduction by 132.5° and 53.6°, respectively [Fig. 1.3(c)]. The singularity between joints 3 and 5 naturally occurs only in full elbow extension, i.e., on the edge of the forearm workspace [Fig. 1.3(d)]. With each of these singularity vectors at or near the edge of the human workspace, the middle and majority of the workspace is free of singularities [66] [67].

Torque transmission from the motors to the joints is achieved using a cable system. Each cable begins at a motor capstan and terminates at a reduction pulley. A series of pulleys route each cable around proximally located joints and links that are between the motor and the reduction pulley. A second cable runs from the reduction pulley back to the motor capstan creating a loop, ensuring positive tension in the cables at all times. A second very short loop runs from the reduction pulley to the joint. The

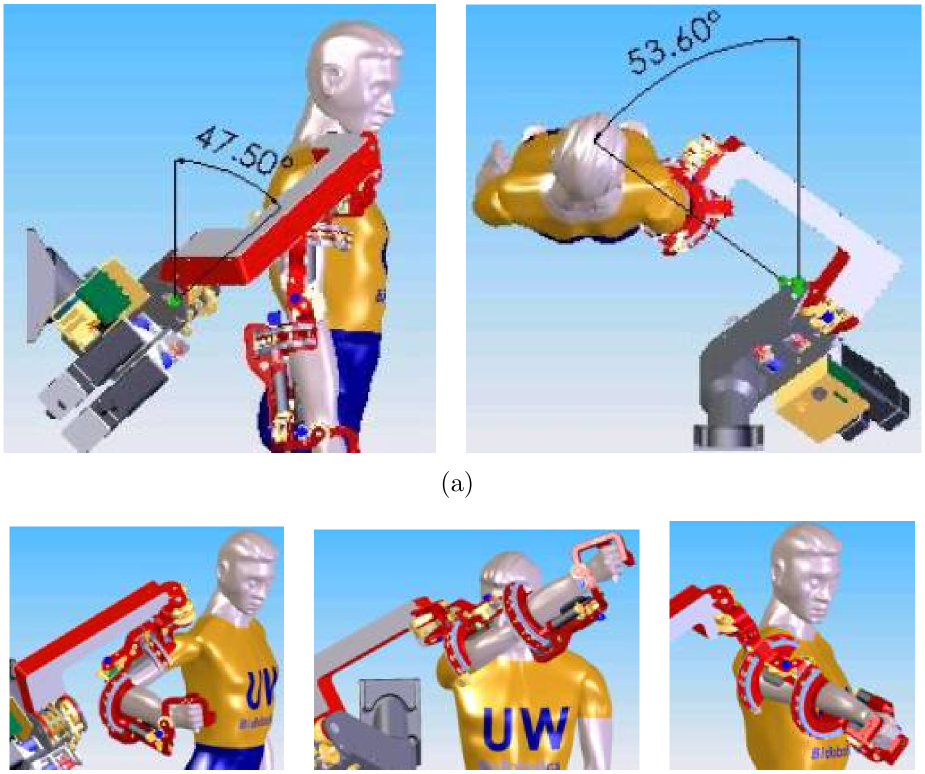

(a)

(b) (c) (d)

Figure 1.3: Two singularities exist in the exoskeleton device, one when joints 1 and 3 align and the other when joints 3 and 5 align. **a)** The orientation of joint 1 places the singularity at the shoulder in an anthropomorphically difficult place to reach. **b)** Joints 1 and 3 align with simultaneous extension and abduction of the upper arm by 47.5° and 53.6° **c)** Similarly, the same singularity can be reached through flexion and adduction by 132.5° and 53.6° **d)** Alignment of joints 3 and 5 naturally occurs only in full elbow extension

short loop is high tension with low travel and the long loop is low tension with high travel. This reduces position error due to cable stretch and increases safety.

As a cable travels through a proximal joint, it is routed around the joint by a pulley and does not travel through the joint's center of rotation. This is necessary in order to create positive tension in the cables for all robot configurations and to avoid physical barriers such has the human arm. As a result, the position and torque outputs of a motor are no longer directly proportional to the position and torque of the joint it is attached to. Instead the position and torque of the joints are linear combination of the position and torque of the motors. Chapter 3 relates the motor and joint position and torques.

There are eight frame assignments for each exoskeleton, one global frame and a local frame for each of the seven links. The origin of the global frame is located at the intersection of the first two joint rotations. This location corresponds to the center of the shoulder's ball joint and is stationary with respect to the base of the robot. The axes are oriented such that x points to the right of the user, z points up opposite the gravitational vector, and y points forward following the right hand rule. The local frame origins are located at the center of mass of each link. Their axes are coincident with the global frame when the joints are in the initial position. The initial configuration of the robot corresponds to the arm at the side with the palm facing the body. Figure 1.4 shows the global reference frame with the device in its initial position.

The user is in contact at three attachment points on the exoskeleton. One attachment point is for the upper arm, one is for the lower arm and the last is for the hand. The hand connection consists of a handle, the upper and lower arm attachments consists of a pressure distributive structural pad that securely strapped to the mid-distal portion of each respective arm segment. Compliance of relaxed musculature in proximal regions of the limb, as well as non-uniform transformations during muscular contraction, reduce interfacial stiffness and produce higher non-linear

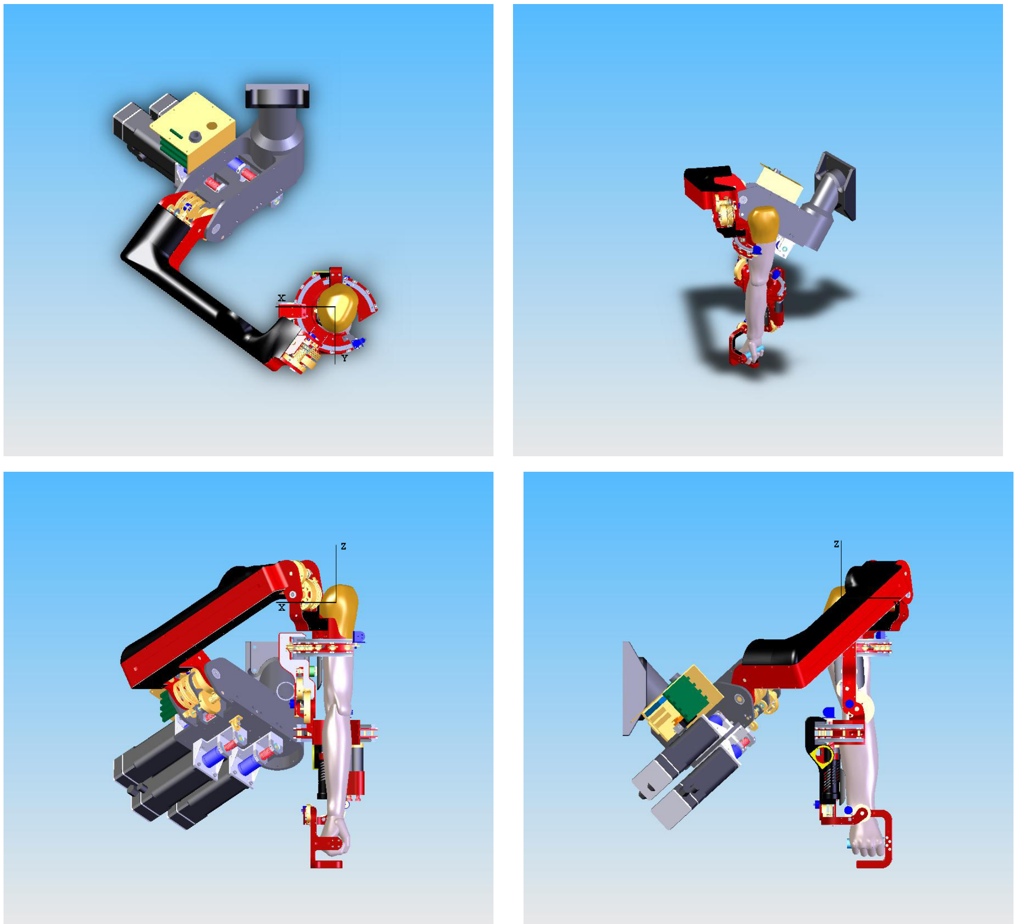

Figure 1.4: The global reference frame for the exoskeleton is located at the intersection of the first two joint rotations. This corresponds to the center of the shoulder ball and socket joint. The device is show in its initial position, with the arm straight down at the side and the palm facing the body.

disturbances in force measurements, which would ultimately result in reduced bandwidth of performance. Cross section of distal parts of limb segments are less variable in magnitude and experience fewer underlying skeletal transformations, making them better attachments. Each interface is rigidly attached to a 6-axis force/torque sensor (ATI Industrial Automation, model - Mini 40) that is in turn rigidly attached to the exoskeleton. These sensors allow every force and torque interactions between the exoskeleton and the user to be measured. Additionally there is a 4th force/torques sensor at the tip of the exoskeleton allowing measurement of force and torque interactions between the exoskeleton and the environment, or an external load.

1.4 Redundant Degree of Freedom

The seven DOF human arm model that we are using is a redundant model. This means that knowing the position and orientation of the hand does not fully specify the configuration of the entire arm. For an exoskeleton device where the entire arm is supported by the mechanism, knowing the full configuration of the arm is important in order to support natural and comfortable movement. By additionally specifying the position of the elbow, the arm configuration is fully defined. However, the addition of the elbow position introduces three additional variables where only one additional variable is needed. Besides adding additional redundant variables, it is possible to specify a combination of hand position/orientation with an elbow position that can't be mutually satisfied.

With the position and orientation of the hand specified, it is possible to parameterize the elbow position as a function of a single variable. To do this we must understand the redundancy in the model. The arm creates a triangle with one point at the shoulder (P_s) one point a that the elbow (P_e) and the last point at the wrist (P_w). Both the shoulder joint and wrist joint are spherical, and allow rotation of point P_e around the vector ($P_w - P_s$) without changing the orientation or position of the hand [Fig. 1.5(a)].

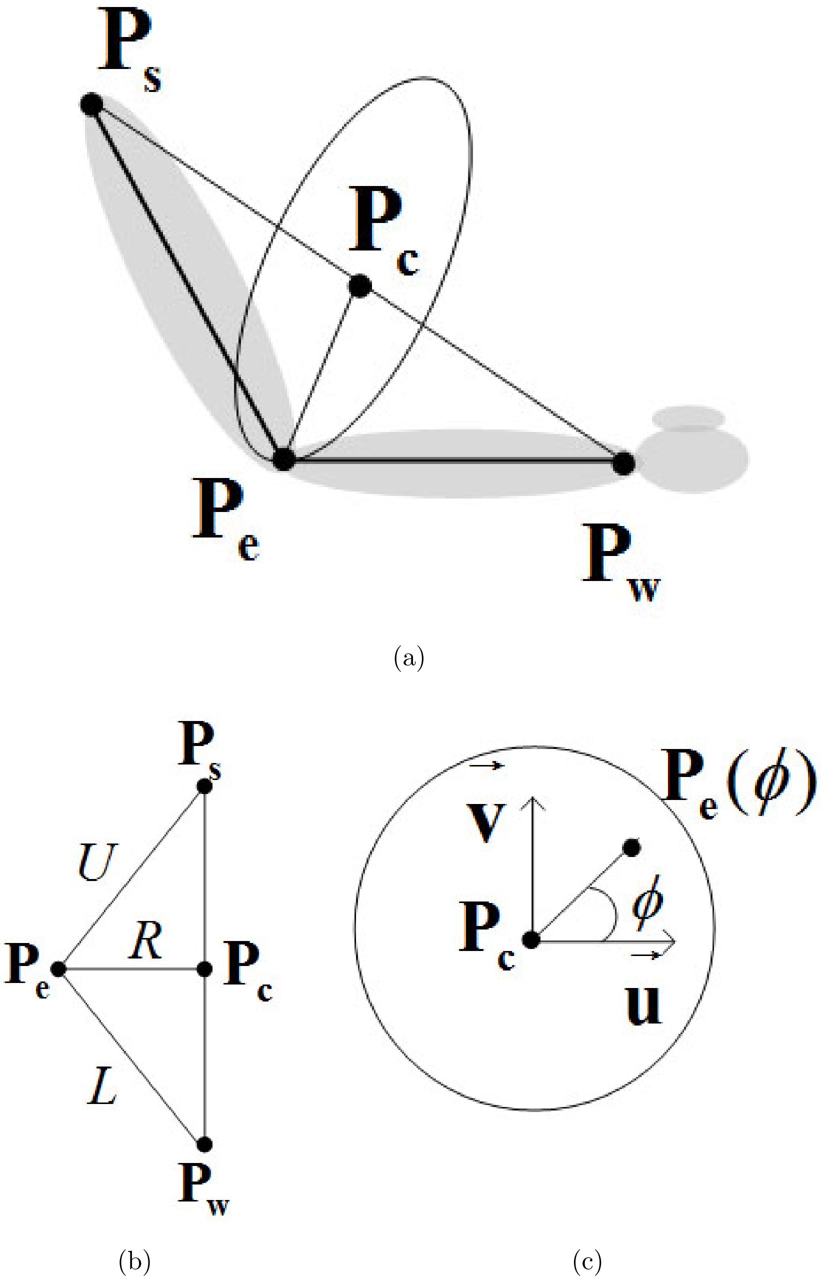

(a)

(b)

(c)

Figure 1.5: **a)** The extra degree of freedom of the arm is defined by a rotation axis that goes from the shoulder to the wrist. **b)** The shoulder, elbow and wrist form the triangle $P_sP_eP_w$. **c)** By creating a coordinate frame at the center of the elbow circle the swivel angel can be defined allowing the parameterizations of the elbow position by a single variable

Creating a local coordinate system at the center of the elbow circle (P_c), gives a reference to measure the swivel angle (ϕ) of the elbow. First create a normal vector that points in the same direction as ($P_w - P_s$).

$$\vec{n} = \frac{P_w - P_s}{||P_w - P_s||} \tag{1.1}$$

Next project and normalize a vector onto the plane normal to $\vec{n}$

$$\vec{u} = \frac{\vec{a} - (\vec{a} \cdot \vec{n})\vec{n}}{||\vec{a} - (\vec{a} \cdot \vec{n})\vec{n}||} \tag{1.2}$$

where $\vec{a}$ can be selected as any vector. Badler and Torlani [2] suggest the selection of $\vec{a}$ to be the $-\vec{z}$ vector. This is an intuitive selection because it has real physical meaning. When ϕ is equal to zero, the elbow is in its lowest possible point for the particular position of the hand. Furthermore the height continually increases for larger angles until $\phi = \pi$ when the elbow is in its highest position. A mathematical singularity occurs when ever the vectors $\vec{n}$ and $\vec{a}$ are parallel. If $\vec{a}$ is chosen to be equal to $-\vec{z}$, then every time the desired position of the hand has x and y component that are both equal to zero, equation (1.2) will be singular. This is a bad placement of the singularity because it will be reached every time the arm is at the side in a rest position. With a ball and socket joint, the human arm has no singularities, however the exoskeleton device does have singularities, so we will place the mathematical singularity of equation (1.2) in the same location as the exoskeleton's singularity. This is achieved by selecting $\vec{a}$ to point in the direction of the rotation axis of joint one.

Choosing $\vec{a}$ to be pointing in the same direction as joint one of the exoskeleton places the mathematical singularity of equation (1.2) on the edge of the anthropomorphic workspace at the expense of an intuitive meaning for ϕ. However it is a simple matter to find what angle of ϕ corresponds to the lowest point of the elbow. The elbow will be in the lowest position when ϕ is equal to the following:

$$atan2\left[(\vec{u} \times \vec{b}_z) \cdot \vec{n}\,,\; \vec{u} \cdot \vec{b}_z\right] \tag{1.3}$$

Where $\vec{b}_z$ is the projection of the $-\vec{z}$ vector onto the plane of the elbow circle.

$$\vec{b}_z = -\vec{z} + (\vec{z} \cdot \vec{n})\vec{n} \tag{1.4}$$

To create the last vector of the coordinate system, take the cross product of $\vec{n}$ and $\vec{u}$.

$$\vec{v} = \vec{n} \times \vec{u} \tag{1.5}$$

Vectors $\vec{n}$, $\vec{u}$ and $\vec{v}$ form an orthonormal coordinate system. Where $\vec{u}$ and $\vec{v}$ are in the plane of the elbow circle [Fig. 1.5(c)]. The the radius (R) and center (P_c) of the circle are easily found through geometry.

$$\begin{aligned} R &= U \sin(\alpha) && (1.6) \\ P_c &= P_s + U\cos(\alpha) \cdot \vec{n} && (1.7) \\ \cos(\alpha) &= \frac{U^2 - L^2 - ||P_w - P_s||^2}{-2L^2||P_w - P_s||} && (1.8) \end{aligned}$$

Where U and L are the length of the upper and lower arm segments [Fig. 1.5(b)]. Now the position of the elbow can now be expresses as a parametrization of ϕ [80].

$$P_e(\phi) = R\left[\cos(\phi)\vec{u} + \sin(\phi)\vec{v}\right] + P_c \tag{1.9}$$

It is also possible to solve for ϕ given P_e. First project $P_e - P_s$ onto the plane of the elbow circle

$$\vec{p}_e = [(P_e - P_s) - (\vec{n}\vec{n}^T)(P_e - P_s)]$$

Then:

$$\phi = atan2\left[\vec{n}^T(\vec{u} \times \vec{p}_e)\,,\,\vec{u}^T\vec{p}_e\right] \tag{1.10}$$

1.5 Controller Overview

Just as important as the physical hardware of the system is the control scheme that is used to drive it. Figure 1.6 shows the block diagram of the control system for the exoskeleton device. The user interacts with the exoskeleton and forces are exchanged between the user and the device through the HMI. The controller takes readings from the force sensors, EMG sensors, and position sensors to determine the required motor torque. Due to coupling of the system, the controller is wrapped with position and torque decoupling. The desired joint positions are determined by a combination of EMG prediction, swivel prediction, admittance control and teleoperation controllers. The desired position is then put through the inverse kinematics, and a PID control along with friction and a gravity compensator is used to calculate the required joint torque to achieve the desired position. Additionally there is a haptic interface for the user and a therapist interface to switch between treatment modes. The following sections give a brief over view of the decoupling scheme, gravity compensator, admittance control, and EMG Control with a more complete description in the body of this work. Teleoperation, and the haptic and therapist interfaces are teated in the future work section.

1.5.1 Decoupling

The cable transmission system of the robot creates coupling between the torque and position of the robot's motors and joints. Spinning one motor will cause motion and torque to be applied to multiple joints. With the assumption that the cable system is frictionless and does not stretch, the mapping from joint space to motor space is one to one and onto. The decoupling controller subsystem takes one of four inputs: 1) motor torque, 2) motor position, 3) joint torque or 4) joint position and returns

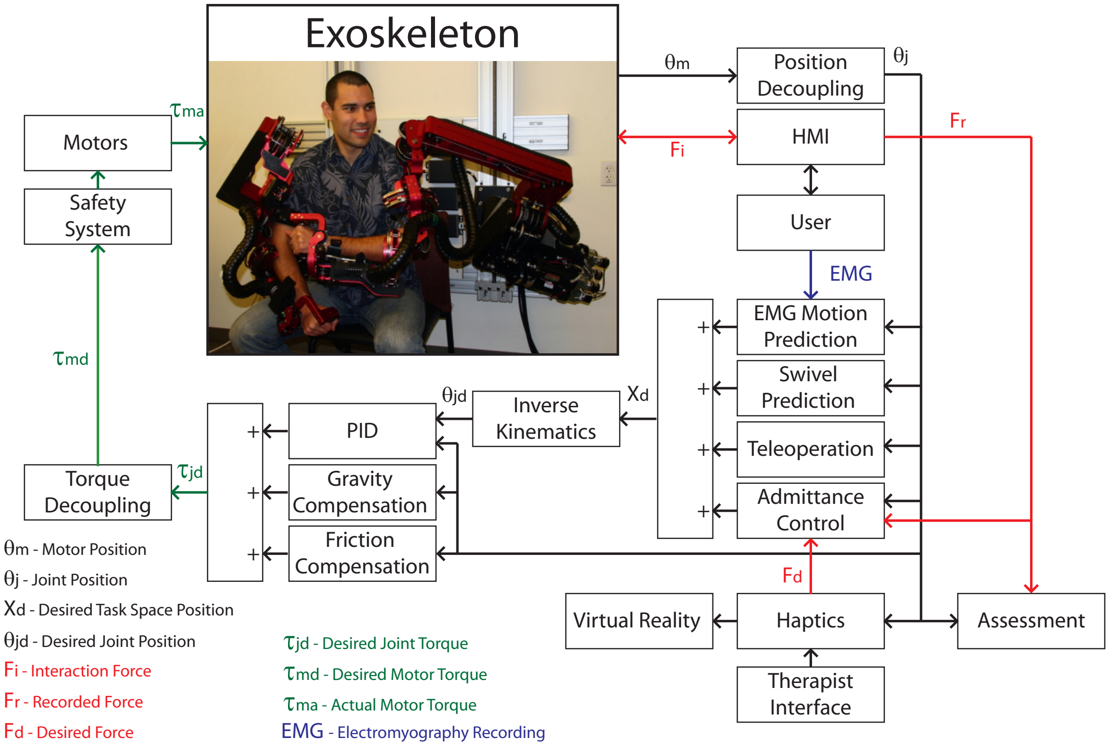

Figure 1.6: Block Diagram

one of four outputs: 1) joint torque, 2) joint position, 3) motor torque, or 4) motor position respectively. For a detailed discussion of the decoupling algorithm refer to chapter 3

1.5.2 Gravity Compensation

The weight of the exoskeleton system is unacceptably high especially for someone with a disability. The purpose of the gravity compensator compensator is to allow the motors of the device to produce exactly the right amount of torque to counter act the torque caused by gravity. The gravity compensator is a model based feed-forward controller with its parameters fit experimentally. It does a reasonably good job of compensating for the gravity, but because it is feed-forward and not feedback, no corrections for modeling errors are made. The gravity compensator calculates the required torque that each joint requires to support the weight of the device. The joint position is taken as an input to the system. The output of the system is the joint torque. For a detailed review of the gravity compensator model refer to my masters thesis [57].

1.5.3 Admittance Control

Admittance control is a feedback controller that tracks the user's movement in free space, and can render forces to the user's arm in virtual reality. Taking force readings from the four force sensors that are embedded in the system, this controller attempts to regulate the force to a prescribed value. For motion tracking the desired interaction force will be zero, for interaction with virtual objects the force will be non-zero. This control closes the loop on the user's intent and provides feedback to counteract modeling errors from the other feed-forward control models. The admittance controller is a reactive system; you push, then it moves, resulting in a finite delay, limiting the bandwidth of the system. Current joint position and interaction forces are taken as an input to the controller, and desired joint positions are returned as an output. For a detailed review of the controller refer to chapter 4.

1.5.4 Swivel Prediction

The human arm model presented in section 1.2 and the exoskeleton device presented in 1.3 are redundant. Section 1.4 shows that the redundancy is characterized by the swivel angle ϕ. With the hand position/orientation, and the swivel angle specified, the configuration of the arm is full defined. For task based motions, the hand position/orientation is defined by the task. It has been observed that the value of swivel angel is repeatably formed by human subjects, implying that there is an underlying optimization for the redundancy. It has been hypotheized that the swivel angle is chosen to optimize the retraction of the hand to the mouth. Swivel Prediction takes the position/orientation of the hand as an input and the swivel angle is returned as an output. For a detailed review of the controller refer to chapter 5

1.5.5 EMG Control

EMG control used the electromyography to predict the intended motion of the user. With surface electrodes, the nerve impulses in the muscles are measured and a hill based muscle model predicts the force the muscle will produce. Due to an inherent delay from when the impulse can first be measured, and the electro-chemical-mechanical process that causes muscle contraction, the motion of the user can be predicted be before it occurs. This system is predictive not reactive and is feed-forward. The model uses neural activation, muscle length, muscle velocity, and arm configuration to predict the muscle force, the arm configuration to calculate the moment arm of the muscle, and the two together can be used to calculate joint torque. Because humans are biological systems, a parameter fit has to be preformed on each subject. The inputs for this controller are the current exoskeleton joint positions, and the raw EMG signals from the user. The out put is desired joint position. For a deatiled revire of this controller refer to chapter 6

Chapter 2

KINEMATIC CONSIDERATION

The forward and inverse kinematics are important mappings between task space and joint space for all the controller designs of the exoskeleton. The left and right side devices each have their own global frame where the origin is located at the shoulder joint intersection, the z axis points up and is normal to the transverse plane, the x axis point to the users right and is normal to the sagittal plane, and the y axis point forward and is normal to the frontal plane [Fig 1.4].

There are three points on each device where the joint rotations intersect. The first point is the at the shoulder (P_s), the second point is at the elbow (P_e) and the last point is at the wrist (P_w). The initial location of each of these points are defined when the exoskeleton is in its initial position ($\vec{\theta} = \vec{0}$), Table 2.1 defines these values. Note that the initial joint intersection locations for the left and right side have same value but are represented in each devices respective frame.

The initial direction of the vectors that define each rotation axes is also defined when the device is in its initial position. The left and right side exoskeletons are mirrors of one another about the sagittal plane, the sign of the rotation axes are chosen such that the two devices produce a mirrored pose when the joint angle of the two devices are equal. Table 2.2 defines the values for the rotation axes. With the

Table 2.1: Initial Joint intersection locations (m)

$$\begin{array}{rcl} P_s & = & [\ 0,\ 0,\ 0\ ] \\ P_{e_0} & = & [\ 0,\ 0,\ -0.3036\ ] \\ P_{w_0} & = & [\ 0,\ 0,\ -0.5806\ ] \end{array}$$

Table 2.2: Joint rotation axes for the right and left exoskeleton arms

Right Arm	**Left Arm**
$\vec{\omega}_{R1} = [\ 0.7071, -0.5213, -0.4777\ ]$	$\vec{\omega}_{L1} = [\ 0.7071, 0.5213, 0.4777\ ]$
$\vec{\omega}_{R2} = [\ 0.5934, 0.8089, 0\ ]$	$\vec{\omega}_{L2} = [\ 0.5934, -0.8089, 0\ ]$
$\vec{\omega}_{R3} = [\ 0, 0, 1\ ]$	$\vec{\omega}_{L3} = [\ 0, 0, -1\ ]$
$\vec{\omega}_{R4} = [\ 1, 0, 0\ ]$	$\vec{\omega}_{L4} = [\ 1, 0, 0\ ]$
$\vec{\omega}_{R5} = [\ 0, 0, 1\ ]$	$\vec{\omega}_{L5} = [\ 0, 0, -1\ ]$
$\vec{\omega}_{R6} = [\ 0, 1, 0\ ]$	$\vec{\omega}_{L6} = [\ 0, -1, 0\ ]$
$\vec{\omega}_{R7} = [\ 1, 0, 0\ ]$	$\vec{\omega}_{L7} = [\ 1, 0, 0\ ]$

joint intersection positions and rotation directions, is it possible to define the forward kinematics using the Product of Exponential (POE) method [60].

2.1 Forward Kinematics

The forward kinematic map transforms points from one link frame to another. The transformation matrix going from link i to link $i-1$ has the form:

$$T_i = \begin{bmatrix} R_i & P_i \\ 0 & 1 \end{bmatrix} \tag{2.1}$$

where R_i is the 3×3 rotation matrix about the axis $\vec{\omega}_i$ and is equal to:

$$R_i = I + \hat{\omega}_i \sin(\theta_i) + \hat{\omega}_i{}^2 \cos(\theta_i) \tag{2.2}$$

and P_i is the 3×1 translation vector and is equal to:

$$P_i = P_{q_i} - R_i P_{q_i} \tag{2.3}$$

Where P_q is a point that the axis of rotation passes through. For joints 1, 2 and 3 $P_q = P_s$, for joint 4, $P_q = P_{e_0}$, and for joint 5, 6 and 7 $P_q = P_{w_0}$. Appendix E has the transformation matrix for each joint rotation. Now the mapping from the base to the tip and base to the elbow can be computed as follows:

$$T_1T_2T_3T_4T_5T_6T_7g_{st} = g_d \tag{2.4}$$

$$T_1T_2P_{e_0} = P_e(\phi) \tag{2.5}$$

Where g_{st} is the transformation from the seventh joint frame to the tool frame, g_d is the desired location of the tool frame, P_{e_0} is the initial position of the elbow and is defined in table 2.1 and $P_e(\phi)$ is the desired position of the elbow as a function of the swivel angle which is defined in equation 1.9

2.2 Inverse Kinematics

With seven degrees of freedom, the exoskeleton is a redundant manipulator. There are several methods to do inverse kinematics on redundant manipulators [4, 5]. Many of them use the pseudoinverse of the jacobian where the null space is used to achieve secondary objectives [3]. In our case we are going to specify the swivel angle making the problem no longer redundant. With the exception of θ_4, all the joint angles are solved by manipulating (2.4) and (2.5) into the following forms.

$$T_iP_0 = P_d \tag{2.6}$$

$$T_iT_jP_0 = P_d \tag{2.7}$$

Where P_0 is an initial starting position and P_d is the desired final position of a point. The rotation axes ω_i and ω_j in equation (2.7) intersect. The solution to these two subproblems are well defined and examined in [60] and [87]. The solution to (2.6) can be found in Appendix C and the solution to (2.7) can be found in Appendix D

Solution for θ_4

The angle θ_4, of the elbow , is just a function of the wrist position, and can easily be solved by application of the law of cosine.

$$\theta_{R4} = \pi \pm \arccos\left(\frac{L^2 + U^2 - ||P_w - P_s||^2}{2LU}\right) \quad (2.8)$$

$$\theta_{L4} = \pi \pm \arccos\left(\frac{L^2 + U^2 - ||P_w - P_s||^2}{2LU}\right) \quad (2.9)$$

There are two solutions for θ_4, to maintain natural arm configuration chose the bottom sign in (2.8) and (2.9).

Solution for θ_1 and θ_2

Equation (2.5) is already in the form of equation (2.7) with $P_0 = P_{e_0}$ and $P_d = P_e(\phi)$, and allows for the immediate solution for θ_1 and θ_2.

$$\theta_{R1} = -atan2\left(\mp P_d \cdot \vec{\omega}_{R2}\ ,\ \mp P_d \cdot (\vec{\omega}_{R1} \times \vec{\omega}_{R2})\right) \quad (2.10)$$

$$\theta_{R2} = atan2\left(-P_d \cdot \vec{\omega}_{R1}\ ,\ \pm\sqrt{U^2 - (P_d \cdot \vec{\omega}_{R1})^2}\right) + acos(\vec{\omega}_1 \cdot \vec{\omega}_{R3}) - \frac{\pi}{2} \quad (2.11)$$

$$\theta_{L1} = -atan2\left(\pm P_d \cdot \vec{\omega}_{L2}\ ,\ \pm P_d \cdot (\vec{\omega}_{L1} \times \vec{\omega}_{L2})\right) \quad (2.12)$$

$$\theta_{L2} = atan2\left(P_d \cdot \vec{\omega}_{L1}\ ,\ \pm\sqrt{U^2 - (P_d \cdot \vec{\omega}_{L1})^2}\right) + acos(\vec{\omega}_{L1} \cdot \vec{\omega}_{L3}) - \frac{\pi}{2} \quad (2.13)$$

There are two solutions for θ_1 and θ_2, for natural arm configurations the top sign in (2.10), (2.11), (2.12) and (2.13) should be chosen.

Solution for θ_3

To solve for θ_3, premultiply equation (2.4) by $(T_1T_2)^{-1}$ and postmultiply by g_{st}^{-1}.

$$T_3T_4T_5T_6T_7 = (T_1T_2)^{-1}g_d g_{st}^{-1} \quad (2.14)$$

Next, postmultiply by P_{w_0}, the initial position of the wrist and an eigne vector of T_5, T_6 and T_7. Because the associated eigne value is equal of one, $T_5T_6T_7P_{w_0} = P_{w_0}$ and

$$T_3T_4P_{w_0} = (T_1T_2)^{-1}g_dg_{st}^{-1}P_{w_0} \tag{2.15}$$

This is now in the form of equation (2.6) with $P_0 = T_4P_{w_0}$ and $P_d = (T_1T_2)^{-1}g_dg_{st}^{-1}P_{w_0}$.

$$\theta_{R3} \quad = \quad atan2(-(P_0)_y(P_d)_x\ ,\ (P_0)_y(P_d)_y) \tag{2.16}$$

$$\theta_{L3} \quad = \quad atan2((P_0)_y(P_d)_x\ ,\ (P_0)_y(P_d)_y) \tag{2.17}$$

Solution for θ_5 and θ_6

To solve for θ_5 and θ_6, being by premultiplying equation (2.4) by $(T_1T_2T_3T_4)^{-1}$ and post multiply by g_{st}^{-1}.

$$T_5T_6T_7 = (T_1T_2T_3T_4)^{-1}g_dg_{st}^{-1} \tag{2.18}$$

Next select a point that is on the rotation axis of joint 7 but is not on the rotation axis of joints 5 and 6 ($P_7 = \omega_7 + P_{w_0}$). This point is an eigne vector of T_7 with an eigne value of one, so $T_7P_7 = P_7$ and

$$T_5T_6P_7 = (T_1T_2T_3T_4)^{-1}g_dg_{st}^{-1}P_7 \tag{2.19}$$

This is now in the form of equation (2.7) when $P_0 = P_7$ and $P_d = (T_1T_2T_3T_4)^{-1}g_dg_{st}^{-1}P_7$.

$$\begin{aligned}\theta_{R5} &= -atan2(\mp(P_d)_y, \pm(P_d)_x) && (2.20)\\ \theta_{R6} &= atan2\left(-((P_d)_z + U + L), \pm\sqrt{(P_0)_x^2 - ((P_d)_z + U + L)^2}\right) && (2.21)\end{aligned}$$

$$\theta_{L5} = -atan2(\pm(P_d)_y, \pm(P_d)_x) \tag{2.22}$$

$$\theta_{L6} = atan2\left(((P_d)_z + U + L), \pm\sqrt{(P_0)_x^2 - ((P_d)_z + U + L)^2}\right) \tag{2.23}$$

The solution for θ_5 and θ_6 has two solutions. For natural arm configurations select the top sign in equations (2.20), (2.21), (2.22) and (2.23).

Solution for θ_7

To solve for θ_7, begin by premultiplying (2.4) by $(T_1T_2T_3T_4T_5T_6)^{-1}$ and postmultiplying by g_{st}^{-1}

$$T_7 = (T_1T_2T_3T_4T_5T_6)^{-1} g_d g_{st}^{-1} \tag{2.24}$$

Next, select any point that is not on the rotation axis of joint 7, point P_s for instance, to achieve the form of equation (2.6).

$$T_7 P_s = (T_1T_2T_3T_4T_5T_6)^{-1} g_d g_{st}^{-1} P_s \tag{2.25}$$

where $P_0 = P_s$ and $P_d = (T_1T_2T_3T_4T_5T_6)^{-1} g_d g_{st}^{-1} P_s$

$$\theta_{R7} = atan2(-(P_d)_y, (P_d)_z + U + L) \tag{2.26}$$

$$\theta_{L7} = atan2(-(P_d)_y, (P_d)_z + U + L) \tag{2.27}$$

Chapter 3

DECOUPLING

For control, we need to work with positions and torques in joint space. However, the position signals we collect and torque values we command are in motor space. Because of coupling caused by the cable system, the motors are related by linear combinations of the joints. To control the system, a mapping from motor space to joint space must be used to preprocess motor encoder signals. Also a mapping from joint space to motor space must be used to postprocess joint torque commands.

3.1 Position

The cables in the mechanism create position coupling between the motors and joints. To control the exoskeleton, a mapping from motor space to joint space is needed. Under the assumptions that the cables can not stretch and always have positive tension, this mapping will be one to one and onto.

For this mechanism, each cable run begins at a motor capstan and runs through intermediate joints to the reduction pulley at its terminating joint. In each cable run, there are three locations where the length of the cable wrap can change: the capstan,

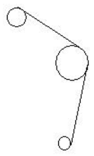

Figure 3.1: Each cable begins at the capstan, runs through intermediate pulleys and ends at a reduction pulley

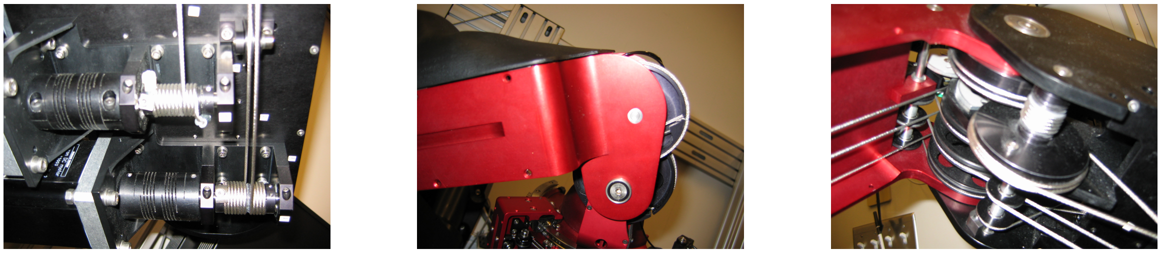

(a) (b) (c)

Figure 3.2: **a)** Capstan **b)** Intermediate Pulley **c)** Reduction Pulley

intermediate joints and reductions pulley. The change of length of the cable on each of the three elements can be related to the change in angle of the joints and motors by the physical parameters of the system (i.e. pulley radius, gear ratio, etc.).

The change in cable length around the i^{th} capstan (δL_i^C) is related to the change in the i^{th} motor angle ($\delta\theta_i^M$) by the radius of the capstan plus the cable that is around it (r_i^C), and the motor's gear ratio (η_i).

$$\delta L_i^C = \pm\frac{r_i^C}{\eta_i} \times \delta\theta_i^M \tag{3.1}$$

The sign of the change is determined by the direction the cable is wrapped around the capstan relative to the defined positive rotation.

The change in cable length around a pulley that is attached to the i^{th} joint and has the j^{th} cable around it (δL_{ij}^P) is related to the change in the joint's angle ($\delta\theta_i^J$) by the radius of the pulley plus the cable that is around it (r_{ij}^P) for an intermediate joint. If it is a reduction pulley (i.e. $i = j$), the pulley reduction ratio (γ_i) is also needed.

$$\delta L_{ij}^P \;=\; \pm\begin{cases} r_{ij}^P \times \delta\theta_i^J & \text{if } i \neq j \\ \frac{r_{ij}^P}{\gamma_i} \times \delta\theta_i^J & \text{if } i = j \end{cases} \tag{3.2}$$

Again, the sign of the change is determined by the direction the cable is wrapped around the pulley relative to the defined positive rotation.

From the assumptions, cable length is conserved and the sum of all changes in cable length j must equal zero.

$$0 = \delta L_j^C + \sum_{i=1}^{j} \delta L_{ij}^P \tag{3.3}$$

Substitute in (3.1) and (3.2) into (3.3)

$$\begin{aligned} 0 &= \pm\frac{r_j^C}{\eta_j} \times \delta\theta_j^M \pm \frac{r_{jj}^P}{\gamma_j} \times \delta\theta_j^J \pm \sum_{i=1}^{j-1} \left[r_{ij}^P \times \delta\theta_i^J \right] \\ &\Leftrightarrow \\ \delta\theta_j^M &= \pm\frac{\eta_j \times r_{jj}^P}{\gamma_j \times r_j^C} \times \delta\theta_j^J \pm \sum_{i=1}^{j-1} \left[\frac{\eta_j \times r_{ij}^P}{r_j^C} \times \delta\theta_i^J \right] \end{aligned} \tag{3.4}$$

Although we actually want to find the mapping from motor space to joint space, it is easier to solve the inverse mapping first. The mapping is one to one and onto, so the matrix will be invertible. Create n-vectors for the joint position (Θ^J) and motor position (Θ^M). These two vectors are related by the position decoupling matrix (D^P):

$$\Theta^M = D^P \cdot \Theta^J$$

From (3.4) D^P must be lower triangular and have the form:

$$D^P = \begin{bmatrix} \pm\frac{\eta_1 \times r_{11}^P}{\gamma_1 \times r_1^C} & 0 & \dots & 0 \\ \pm\frac{\eta_2 \times r_{12}^P}{r_2^C} & \pm\frac{\eta_2 \times r_{22}^P}{\gamma_2 \times r_2^C} & 0 & \vdots \\ \vdots & \ddots & \ddots & 0 \\ \pm\frac{\eta_n \times r_{1n}^P}{r_n^C} & \dots & \pm\frac{\eta_n \times r_{n-1n}^P}{r_n^C} & \pm\frac{\eta_n \times r_{nn}^P}{\gamma_n \times r_n^C} \end{bmatrix} \tag{3.5}$$

3.2 Torque

The cables in the mechanism create torque coupling between the motors and joints. To control the mechanism, a mapping from joint space to motor space is needed. Under the assumptions that the cables can not stretch, always have positive tension, are frictionless and do not slip, this mapping is one to one and onto.

Under these assumptions, the force in the cables will be the same throughout an entire cable run. It is possible to relate the force in the cables to the torque on the motors, intermediate pulleys and reduction pulleys through the physical parameters of the exoskeleton (i.e. pulley radius, gear ratio, etc.).

The torque on the i^{th} motor (τ_i^M) is related to the force on the cable attached to it (F_i^C) by the motor's gear ratio (η_i) and the radius of the capstan plus the cable that is around it (r_i^C)

$$\tau_i^M = \pm F_i^C \times \frac{r_i^C}{\eta_i} \quad \Leftrightarrow \quad F_i^C = \pm\frac{\eta_i}{r_i^C} \times \tau_i^M \tag{3.6}$$

The sign of the change is determined by the direction the cable is wrapped around the pulley relative to the defined positive rotation.

The torque around a pulley that is attached to the i^{th} joint with the j^{th} cable around it (τ_{ij}^P) is related to the force on the cable (F_j^C) by the radius of the pulley plus the cable wrapped around it (r_{ij}^P) for an intermediate pulley. If it is a reduction pulley ($i = j$), the pulley reduction ratio (γ_i) is also needed.

$$\tau_{ij}^P \quad = \quad \pm \begin{cases} r_{ij}^P \times F_j^C & \text{if } i \neq j \\ \frac{r_{ij}^P}{\gamma_i} \times F_j^C & \text{if } i = j \end{cases}$$

Replacing F_j^C with (3.6)

$$\tau_{ij}^P = \pm\begin{cases} \frac{\eta_j \times r_{ij}^P}{r_j^C} \times \tau_j^M & \text{if } i \neq j \\ \frac{\eta_j \times r_{ij}^P}{\gamma_i \times r_j^C} \times \tau_j^M & \text{if } i = j \end{cases} \tag{3.7}$$

Again, the sign of the change is determined by the direction the cable is wrapped around the pulley relative to the defined positive rotation.

By superposition, the torque on the i^{th} joint (τ_i^J) is the sum of the torque on each pulley attached to that joint.

$$\tau_i^J = \sum_{j=i}^{n} \tau_{ij}^P \tag{3.8}$$

Substitute (3.7) into (3.8) .

$$\tau_i^J = \pm\frac{\eta_i \times r_{ii}^P}{\gamma_i \times r_i^C} \times \tau_i^M \pm \sum_{j=i+1}^{n} \left[\frac{\eta_j \times r_{ij}^P}{r_j^C} \times \tau_j^M\right] \tag{3.9}$$

Although we actually want to find the mapping from joint space to motor space, it is easier to solve for the inverse mapping first. The mapping is one to one and onto, so the matrix will be invertible. Create n-vectors for the joint torque (T^J) and motor torque (T^M). These two vectors are related by the torque decoupling matrix (D^τ):

$$T^J = D^\tau \cdot T^M$$

From (3.9) D^τ must be upper triangular and have the form:

$$D^\tau = \begin{bmatrix} \pm\frac{\eta_1 \times r_{11}^P}{\gamma_1 \times r_1^C} & \pm\frac{\eta_2 \times r_{12}^P}{r_2^C} & \dots & \pm\frac{\eta_n \times r_{1n}^P}{r_n^C} \\ 0 & \pm\frac{\eta_2 \times r_{22}^P}{\gamma_2 \times r_2^C} & \ddots & \vdots \\ \vdots & 0 & \ddots & \pm\frac{\eta_n \times r_{n-1n}^P}{r_n^C} \\ 0 & \dots & 0 & \pm\frac{\eta_n \times r_{nn}^P}{\gamma_n \times r_n^C} \end{bmatrix} \tag{3.10}$$

3.3 Exoskeleton Decoupling

The exoskeleton has motors placed in two distinct places. Four large motors are mounted on the base, and three smaller motors are mounted on joint five. This configuration creates coupling between the first four joints as well as the last two; the fifth joint is decoupled from the others. Applying (3.10) to each of the three coupled sections (1-4, 5 and 7-8) separately and concatenating produces the 7x7 torque decoupling matrix for the exoskeleton.

Appendix A contains the physical constants for the exoskeleton used to calculate the decoupling matrices. From (3.10) the first 4x4 decoupling block equals:

$$\begin{bmatrix} \pm\frac{\eta_1 \times r^P_{11}}{\gamma_1 \times r^C_1} & \pm\frac{\eta_2 \times r^P_{12}}{r^C_2} & \pm\frac{\eta_3 \times r^P_{13}}{r^C_3} & \pm\frac{\eta_4 \times r^P_{14}}{r^C_4} \\ 0 & \pm\frac{\eta_2 \times r^P_{22}}{\gamma_2 \times r^C_2} & \pm\frac{\eta_3 \times r^P_{23}}{r^C_3} & \pm\frac{\eta_4 \times r^P_{24}}{r^C_4} \\ 0 & 0 & \pm\frac{\eta_3 \times r^P_{33}}{\gamma_4 \times r^C_4} & \pm\frac{\eta_4 \times r^P_{34}}{r^C_4} \\ 0 & 0 & 0 & \pm\frac{\eta_4 \times r^P_{44}}{\gamma_4 \times r^C_4} \end{bmatrix} = \begin{bmatrix} 12.04 & -3.26 & -3.41 & 4.10 \\ 0 & 11.75 & -3.41 & 4.10 \\ 0 & 0 & -9.44 & 11.41 \\ 0 & 0 & 0 & -13.40 \end{bmatrix} \tag{3.11}$$

The second 1x1 block equals:

$$\begin{bmatrix} \pm\frac{\eta_5 \times r^P_{55}}{\gamma_5 \times r^C_5} \end{bmatrix} = \begin{bmatrix} 30.33 \end{bmatrix} \tag{3.12}$$

and the last 2x2 block equals:

$$\begin{bmatrix} \pm\frac{\eta_6 \times r^P_{66}}{\gamma_6 \times r^C_6} & \pm\frac{\eta_7 \times r^P_{67}}{r^C_7} \\ 0 & \pm\frac{\eta_7 \times r^P_{77}}{\gamma_7 \times r^C_7} \end{bmatrix} = \begin{bmatrix} 27.07 & 26.61 \\ 0 & -27.07 \end{bmatrix} \tag{3.13}$$

The complete decoupling matrix is found by concatenating (3.11), (3.12) and (3.13)

$$D^{\tau} = \begin{bmatrix} 12.04 & -3.26 & -3.41 & 4.10 & 0 & 0 & 0 \\ 0 & 11.75 & -3.41 & 4.10 & 0 & 0 & 0 \\ 0 & 0 & -9.44 & 11.41 & 0 & 0 & 0 \\ 0 & 0 & 0 & -13.40 & 0 & 0 & 0 \\ 0 & 0 & 0 & 0 & 30.33 & 0 & 0 \\ 0 & 0 & 0 & 0 & 0 & 27.07 & 26.61 \\ 0 & 0 & 0 & 0 & 0 & 0 & -27.07 \end{bmatrix}$$

Taking the inverse of the matrix

$$(D^{\tau})^{-1} = \begin{bmatrix} .0831 & .0231 & .0383 & .0001 & 0 & 0 & 0 \\ 0 & .0851 & -.0307 & -.0001 & 0 & 0 & 0 \\ 0 & 0 & -.1059 & -.0902 & 0 & 0 & 0 \\ 0 & 0 & 0 & -.0746 & 0 & 0 & 0 \\ 0 & 0 & 0 & 0 & .0330 & 0 & 0 \\ 0 & 0 & 0 & 0 & 0 & .0369 & 0.0363 \\ 0 & 0 & 0 & 0 & 0 & 0 & -.0369 \end{bmatrix}$$

Examining (3.5) and (3.10) reveals that the position and torque decoupling matrices are related.

$$D^{\tau} = (D^{P})^{T}$$

The position decoupling matrix does not have to be calculated. Simply take the transpose of the torque decoupling matrix.

Chapter 4

ADMITTANCE CONTROL

Typically, in admittance control a force sensor is attached to the end effector of a robot, then the input from this sensor is used to produce velocity commands for the device. The redundancy in our device creates problems with this model, not only do we have to specify the velocity of the handle, velocities for the elbow angle must also be specified. Several algorithms have been developed to select the elbow angle, including creating selection criteria based on kinematic, dynamic and biomechanical data [49]. Creating heuristics based on observations of movement [83], and several iterative methods used to avoid obstacles and joint limits [33], or that use dynamic information [89]. Although these algorithms can create natural reach motions, the exoskeleton device needs to track the motion of the user in all situations. The above mentioned algorithms lack the flexibility of real time use where even small differences in exoskeletons position and the users desired position can cause discomfort. For this reason additional force sensors track the interactions of the user and the device at the upper arm and lower arm allowing forces in the null space of the hand to be monitored.

4.1 Method

There are two fundamental way that the admittance control can be implemented. The first is to use the force/torque to compute a trajectory in task space then use inverse kinematics to calculate the required joint angles. The second is to transform the force/torques signals into joint torque equivalent, then create joint trajectories directly from the torque signals.

4.1.1 Task Space Admittance Control

In task space admittance control, the change in position and orientation of the hand as well as the elbow angle are calculated in task space using the four force sensors. The change in position of the wrist, orientation of the wrist, and the swivel angle are calculated independently at each time step. Then the trajectory of the hand as well as the swivel angle are put through the inverse kinematic function from section 2.2 to find the joint trajectories. The joint trajectories are followed using PID control.

Wrist Position

The position of the wrist is influenced by the force interactions from each of the four forces sensors. It is straight forward to relate the forces at tip ($\vec{f_t}$), handle ($\vec{f_h}$) and lower arm ($\vec{f_l}$), to changes in position at the wrist. Each of these locations have three DOF of translational motion. They each span all of R^3 and the device will not constrain the translational motion at any of these locations. The motions of the device due to the interaction forces will be in the same direction of the force vector. It is not as straight forward for the upper arm, where there are only two translational degrees of freedom. With the shoulder being a spherical joint, any point on the upper arm is constrained to move on a sphere centered at the shoulder. If a force is applied on the upper arm that is tangent to this sphere, then it can move the device along this sphere. If a force is applied that is perpendicular to the sphere, the device resists the force and no motion occurs. A spherical trajectory of the upper arm creates a similar spherical trajectory at the wrist where its motion is also centered around the shoulder. However, the motion at the wrist is not always in the same direction as the force vector at the upper arm.

To relate the direction of the upper arm force sensor and the motion at the wrist, begin by defining a frame at the origin of the upper arm force sensor. Let x point to users right, y point forward and z point up when the arm is at the side. The z component of the upper arm force signal is always perpendicular to the sphere of motion that the sensor is constrained to move on. It is not possible to move the sensor along this trajectory, so the z component of the the signal is set to zero. The x component of the signal creates motion at the wrist in the same direction as the upper arm because the x vector is tangent to the sphere of motion of both the upper arm and wrist [Fig. 4.1(a)]. The y component of the signal does not create motion at the wrist in the same direction as the upper arm signal. When the elbow is bent, the projection onto the yz plane of the vector going from the shoulder to the upper arm sensor and the vector from the shoulder to the wrist are separated by the angle α, previously defined in equation (1.8). Because motion must be tangent to these vectors, a motion in the y direction at the sensor, will cause a motion at the wrist that is rotated by an angle α [Fig. 4.1(b)]. Taking these considerations into mind, the original upper force signal ($\vec{f_u}$) gets transformed as follows:

$$\vec{f_u} = \begin{bmatrix} x \\ y \\ z \end{bmatrix} \Rightarrow \begin{bmatrix} x \\ y \\ 0 \end{bmatrix} \Rightarrow \begin{bmatrix} x \\ cos(\alpha)y \\ sin(\alpha)y \end{bmatrix} \tag{4.1}$$

To work with the four sets of force signals, they must all be in a common frame. It is a simple matter to convert all the signals into the global frame.

$$\vec{f_u}' = R_1R_2R_3\vec{f_u} \tag{4.2}$$

$$\vec{f_l}' = R_1R_2R_3R_4R_5\vec{f_l} \tag{4.3}$$

$$\vec{f_h}' = R_1R_2R_3R_4R_5R_6R_7\vec{f_h} \tag{4.4}$$

$$\vec{f_t}' = R_1R_2R_3R_4R_5R_6R_7\vec{f_t} \tag{4.5}$$

With all the forces transformed we must relate force to a motion command. If the arm and exoskeleton device are moving together perfectly, then the force between the

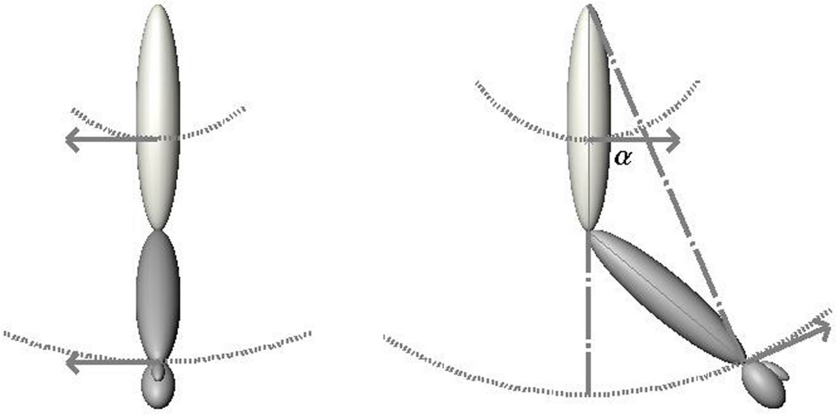

(a) (b)

Figure 4.1: Force interactions at the upper arm create motion that is tangent to a sphere that is centered at the shoulder. **a)** The x component of an upper arm force creates motion in the x direction at the upper arm and wrist. **b)** The y component of the force creates a motion in the y direction at upper arm but the motion is rotated by α at the wrist.The z component is resisted by the mechanism and does not result in motion

user and the device should be zero, provided there are no modelling errors. Therefore we will use zero as our reference force, and the error in the force ($\vec{f_e}$) will be.

$$\vec{f_e} = \vec{f_u}^{'} + \vec{f_l}^{'} + \vec{f_h}^{'} + \vec{f_t}^{'} - \vec{0} \tag{4.6}$$

In this model the forces are all weighted evenly. Next, transform the force signals into a task space position signal.

$$x = k_p \vec{f_e} + k_i \int \vec{f_e} - k_d \dot{x} \tag{4.7}$$

The last term ($-k\dot{x}$) is not directly related to the force error, because force sensors have a lot of noise, taking the derivative can be a problem. If force is approximated with Hooks law

$$F = -K(x - x_0) \tag{4.8}$$

then

$$\dot{F} = -K\dot{x} \tag{4.9}$$

and we can get an approximate derivative of the force without having to deal with a noisy force signal [77]. To deal with integrator windup, the difference between the actual and desired position saturates. This saturation limits the maximum velocity of the wrist. Additionally there is a decay term that slowly brings back the desired position to the current position. This allows the force applied to a stationary object to return to zero if there is no longer a force at the force sensor.

Wrist Orientation

Changes in the wrist orientation are calculated based on the torque applied at the wrist. The upper and lower force sensors are located proximally from the wrist, and therefore produce no torque on the wrist. Both the handle and tip force sensor are located distally from the wrist and will produce torques on the wrist. Neither the wrist or the tip sensors are located at the wrist. Therefore the torque at the wrist ($\vec{\tau_w}$) due to the handle, will be the addition of the handle torque ($\vec{\tau_h}$) with the cross product of the handle distance ($\vec{r_h}$) and the handle force ($\vec{f_h}$). Similarly, the torque at the wrist due to the tip will be the tip torque ($\vec{\tau_t}$) plus the cross product of the tip distance ($\vec{r_t}$) with the tip force ($\vec{f_t}$). By superposition, the total torque at the wrist will be the addition of the contributions of the handle and the tip. Next transform $\vec{\tau_w}$ from the sensor frame into the global frame.

$$\vec{\tau_w} = \left[\vec{\tau_h} + (\vec{r_h} \times \vec{f_h})\right] + \left[\vec{\tau_t} + (\vec{r_t} \times \vec{f_t})\right] \tag{4.10}$$

$$\vec{\tau_w}' = R_1 R_2 R_3 R_4 R_5 R_6 R_7 \vec{\tau_w} \tag{4.11}$$

The desired reference torque is zero, making the error signal

$$\vec{\tau_e} = \vec{\tau_w}' - \vec{0} \tag{4.12}$$

Taking $\vec{\tau_e}$ to be the axis angle representation for the change in orientation, a rotation matrix (R_e) can be constructed to represent the desired change.

$$\theta_e = ||\vec{\tau_e}|| \tag{4.13}$$

$$\vec{\omega_e} = \tfrac{\vec{\tau_e}}{\theta_e} \tag{4.14}$$

$$R_e = I + \hat{\omega_e}\,\sin(\theta_e) + \hat{\omega_e}^2(1 - \cos(\theta_e)) \tag{4.15}$$

Where θ_e is the desired change in angle, $\vec{\omega_e}$ is the rotation axis, I is the 3×3 identity matrix, and $\hat{\omega_e}$ is the antisymmetric matrix equivalent of the cross product. With this the desired orientation (R_d) is then:

$$R_d = R_e R_{d-1} \tag{4.16}$$

Where R_{d-1} is the desired orientation from the previous time step. At initiation R_{d-1} is set equal to the current orientation of link 7. This is equivalent to a discrete time integrator, so a saturation function limits the angular difference between the actual and desired orientation to prevent integrator windup.

Swivel Angle

Changes in the swivel angle are calculated based on the torque applied around the swivel axis. The handle and tip forces are not used for this calculation because the swivel axis defines the redundance of the manipulator. The upper and lower arm force sensors both contribute to the torque around the swivel axis. The upper and lower arm sensors are measured in different frames and have to be put into the common global frame.

$$\vec{\tau_u}' = R_1 R_2 R_3 \vec{\tau_u} \tag{4.17}$$

$$\vec{f_u}' = R_1 R_2 R_3 \vec{f_u} \tag{4.18}$$

$$\vec{\tau_l}' = R_1 R_2 R_3 R_4 R_5 \vec{\tau_l} \tag{4.19}$$

$$\vec{f_l}' = R_1 R_2 R_3 R_4 R_5 \vec{f_l} \tag{4.20}$$

The upper and lower sensors are not located on the rotation axis, so the applied torque on the axis must be calculated. The torque on the shoulder as a result of the upper sensor is equal to the torque at the upper sensor ($\vec{\tau_u}'$) added to the cross product of the vector from the shoulder to the upper sensor ($\vec{r_u}$) with the upper force ($\vec{f_u}'$).

Similarly, the torque on the shoulder as a result of the lower forces is equal to the torque at the lower arm ($\vec{\tau_l}'$) plus the cross product of the vector from the shoulder to the lower sensor ($\vec{r_l}$) with the lower force ($\vec{f_l}'$). By superposition, the total torque on the shoulder ($\vec{\tau_s}$) is the addition of the contributions from the upper and lower arm.

$$\vec{\tau_s} = \left[\vec{\tau_u}' + (\vec{r}_u \times \vec{f_u}')\right] + \left[\vec{\tau_l}' + (\vec{r_l} \times \vec{f_l}')\right] \tag{4.21}$$

Only the component of torque that acts on the swivel axis will cause a change in the swivel angle. The component of $\vec{\tau_s}$ acting on $\vec{n}$ (from Eqn. (1.1)) is fould by taking the dot product of the two.

$$\vec{\tau_n} \;=\; \vec{\tau_s} \cdot \vec{n} \tag{4.22}$$

The desired reference torque is zero so the error is equal to:

$$\vec{\tau_e} = \vec{\tau_n} - 0 \tag{4.23}$$

and the desired swivel angle is:

$$\phi \;=\; k_p\,\vec{\tau_e} + k_i \int \vec{\tau_e} - k_d\,\dot{\phi} \tag{4.24}$$

Like equation (4.7) the term ($-k_d\,\dot{\phi}$) is an approximation of the derivative of the torque without having to take the derivative of a noisy torque signal. A saturation term is added to avoid integrator wind up.

Equations (4.7), (4.16) and (4.24) define the desired position, orientation and swivel angles for a given time step. The desired joint angles are then calculated using the inverse kinematics developed in section 2.2. A PID position controller moves the exoskeleton to the desired joint angles.

4.1.2 Joint Space Admittance Control

In joint space control, the forces and torques from the four sensors are first transformed into the joint torque equivalent. Then changes in joint position are calculated. The transformation is achieved by multiplying the force/torque signal ($F = [\vec{f}, \vec{\tau}]^T$) by the Jacobian transpose (J^T).

$$\Gamma = J^T F \tag{4.25}$$

The Jacobian from the base to each of the force sensors have to be calculated. The upper sensor Jacobian (J_u) will be a 6×3 matrix. The lower sensor Jacobian (J_l) will be a 6×5 matrix. The handle sensor Jacobian (J_h) will be a 6×7 matrix, and the tip sensor Jacobian (J_t) will be a 6×7 matrix. Then the torque on the joints due to each sensor is:

$$\Gamma_u = J_u^T F_u \tag{4.26}$$

$$\Gamma_l = J_l^T F_l \tag{4.27}$$

$$\Gamma_h = J_h^T F_h \tag{4.28}$$

$$\Gamma_t = J_t^T F_t \tag{4.29}$$

The total joint torque on each joint is the summation of the individual joint torques applied as a result of the interaction at each sensor location. The upper and lower sensors, however do not contribute to joint torques of joint that are distally located on the manipulator chain. In order to add the vector quantities, append zeros to Γ_u and Γ_l untill they are both 7×1 vectors. With all the vectors the same dimension, they can be added.

$$\Gamma_j = \Gamma_u + \Gamma_l + \Gamma_h + \Gamma_t \tag{4.30}$$

Finally the desired joint position has to be calculated from the joint torques. The desired reference force for all the sensors is zero, which corresponds to a zero torque at the joints. Then the torque error (Γ_e) is equal to Γ_j and the desired joint position becomes

$$\theta_j = k_p\Gamma_e + k_i\int\Gamma_e - k_d\dot{\theta}_j \qquad (4.31)$$

A saturation function avoids integrator wind up.

4.2 Experimental Setup

This experiment compared movement of the device with task space admittance control using four sensors as described in section 4.1.1 and movement of the device with joint space admittance control using four sensors as described in section 4.1.2. Additionally the motion of manual control (back-driven with no control effort) were recorded.

The height, age and sex of each subject was taken at the beginning of each experiment. The exoskeleton's height was adjusted for each user in a seated position. The subject was secured in the device by two straps, one at the upper arm and the other at the lower arm, additionally the user held a handle. In front of the subject was a table with 3 plastic targets each with two slotted holes that matched a slotted peg on the tip of the device. The target are numbered 1 to 6 from the subjects top right to bottom left. The location of the targets were, target 1 - [.450,.431,.870], target 2 - [.450,.431,.978], target 3 - [.09,.597,.870], target 4 - [.09,.597,.978], target 5 - [-.325,.575,.870], target 6 - [-.325,.575,.978], with x being to the subjects right, y being in front of the subject and z pointing up. x and y are measured from the center of the shoulder, z is measured from the floor, all units are in meters [Fig. 4.2]. In the users left hand was an enable button which released the brakes on the device and engaged the motor. Each subject was instructed to begin with their arm at their side, with the enable button disengaged. The experimenter would then tell them a target to move to, they then press the enable button, insert the peg into the hole, return their arm to the side, and release the enable button. For each experiment there were 6 targets. Each control scheme moved to each target once in random order. Four repetitions were repeated for each subject, and each subject was asked if they needed a break between repetitions.

4.3 Results

Six subjects participated in the experiment. There was a mix of male and female subjects with a range of ages and heights, see table 4.1. All subjects were able to participate in every trial, except subject #4 was who was unable to lift the device under manual control. Data for joint space and task space control was recorded for subject #4. A total of 395 trails were recorded consisting of: 118 trials for manual control, 134 trials for joint space control and 143 trials for task space control.

Table 4.1: Subject Data

Subject	Sex	Age	Height (m)	Exoskeleton Height (m)
1	m	21	1.74	0.86
2	m	23	1.88	0.89
3	m	43	1.74	0.86
4	f	25	1.63	0.79
5	m	22	1.73	0.82
6	f	21	1.70	0.82

Statistical significants was determined using Matlab's anovan and multcompare functions. The multcompare function calculates the mean value and a confidence interval for that value. If two intervals do not overlap then the difference in their means are statically significant at the confidence level selected. If their intervals do over lap then it is not clear if the difference is due to random effects or the effect of the variable. The 95% confidence level was selected as significant for this study.

4.3.1 Forces and Torques

Figure 4.3 shows the average interaction force normalized with respect to task completion. Interactions are shown for the upper, lower, handle and tip force sensors as

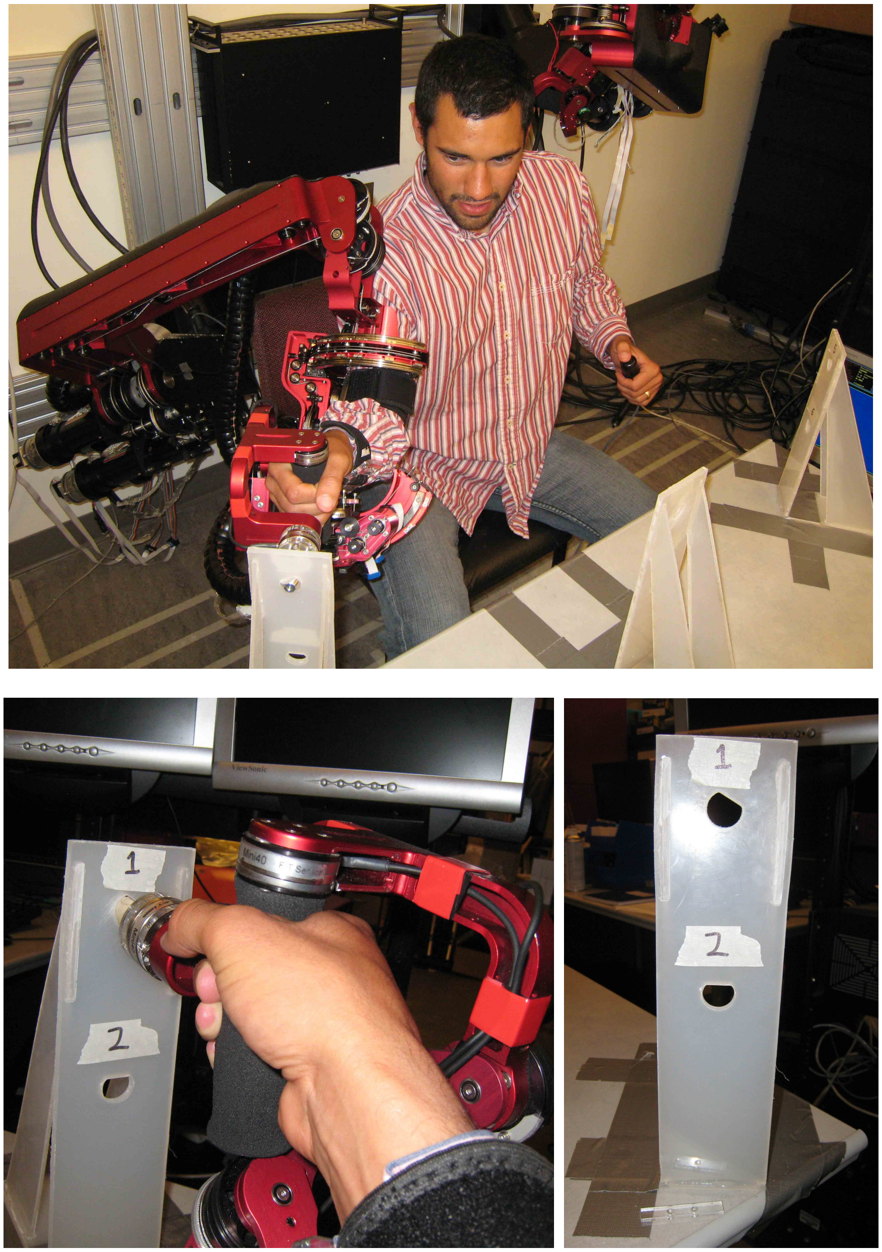

Figure 4.2: A subject inserts the tip of the exoskeleton into a target. There was a total of 6 targets. Each subject performed 4 repetitions of every controller moving to every target

well as the aggregate force of the upper, lower and handle force sensor. Similarly, Figure 4.4 shows the average torque recorded at the upper, lower, handle and tip sensors after being normalized by the task completion time and the aggregate torque from the upper, lower and handle sensor. Table 4.2 shows the average force and torque for the entire task along with the maximum value recorded and the 95% confidance interval for the true mean.

The interaction force for manual control was higher and statistically different at the .05 level from joint space and task space control for the upper, handle and tip force sensors locations and the aggregate force of the three contact points. There was no difference at the lower arm sensor for the three controllers, and there was no statistical difference between joint space and task space control. The interaction torque for manual control was higher and statistically different for joint and task space at the handle and the aggregate force readings. Manual control was not statistically different at any other sensor location. Joint and task space control showed no differences in interaction torque at any sensor location.

4.3.2 Path length

Using the recorded joint angles, the path length of the tip and elbow were calculated. Table 4.3 contains the average of the path length data for the tip and elbow. Manual and task space control showed no statistical differences in tip path length from one another but were shorter and statistically different from joint space control. No control and task space control had no statistical difference for elbow path length but longer and statistically different for joint space control.

4.3.3 Completion time

The task completion time for each controller was measured as the time the enable button was pressed until it was released. Table 4.4 summarizes the task completion time for each controller and figure 4.5(d) shows its distribution. Manual control was

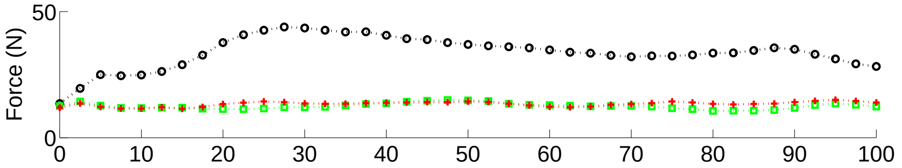

(a) Average Upper Force

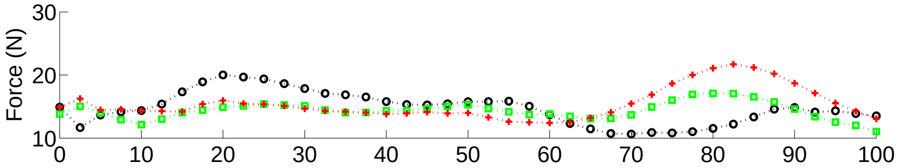

(b) Average Lower Force

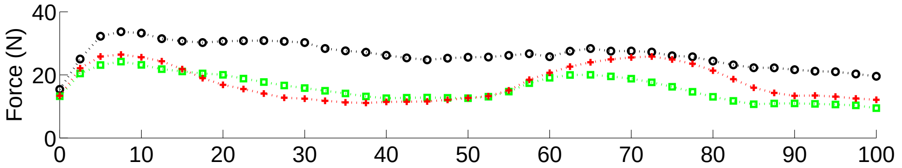

(c) Average Handle Force

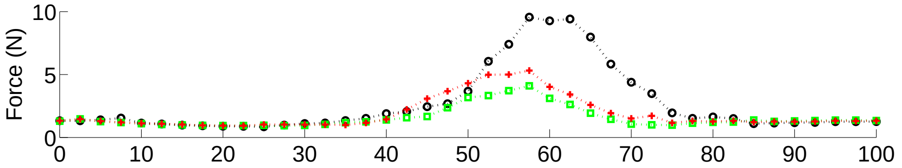

(d) Average Tip Force

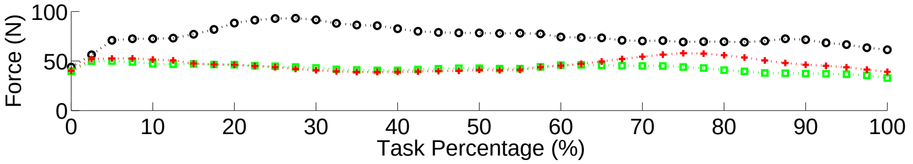

(e) Average Aggregate Force

Figure 4.3: The average interaction force normalized with with respect to task completion time. The black ○ represent manual control, the red + is joint space control and the green □ is for task space control.

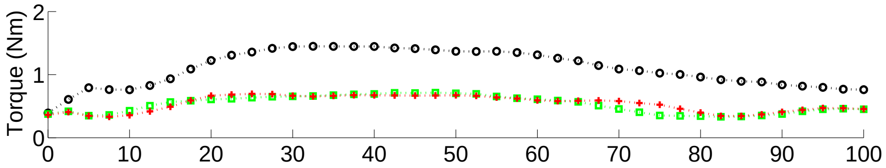

(a) Average Upper Torque

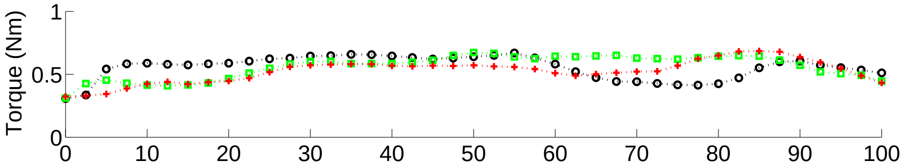

(b) Average Lower Torque

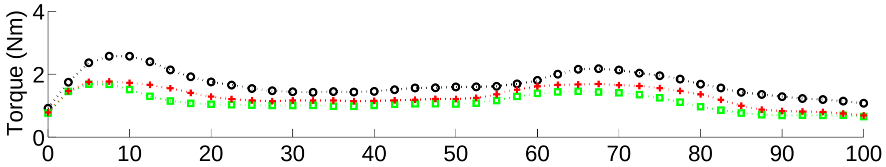

(c) Average Handle Torque

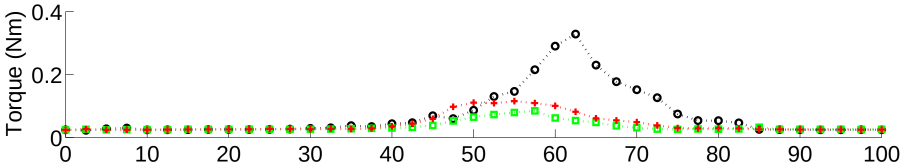

(d) Average Tip Torque

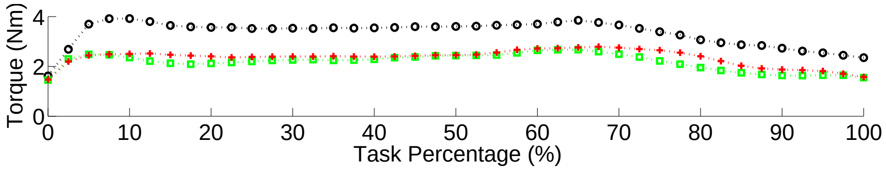

(e) Average Aggregate Torque

Figure 4.4: The average interaction torque normalized with with respect to task completion time. The black ◯ represent manual control, the red + is joint space control and the green □ is for task space control.

Table 4.2: Force and Torque Data

	Manual		**Task Space**		**Joint Space**	
	(N)	(Nm)	(N)	(Nm)	(N)	(Nm)
Upper Arm						
Mean	34	0.81	12	0.59	13	0.60
95% C.I.	1.41	0.036	1.28	0.033	1.27	0.033
Max	127	4.0	74	2.7	72	3.5
Lower Arm						
Mean	15	0.66	14	0.65	15	0.63
95% C.I.	1.17	0.024	1.07	0.022	1.05	0.022
Max	86	2.3	87	3.3	84	2.2
Handle						
Mean	27	1.35	16	1.15	18	1.22
95% C.I.	1.01	0.064	0.92	0.059	0.91	0.058
Max	91	5.2	73	4.6	84	4.8
Tip						
Mean	3	0.095	2	0.067	2	0.074
95% C.I.	0.19	0.013	0.18	0.012	0.17	0.012
Max	49	2.5	43	1.5	40	1.5
All						
Mean	73	2.72	40	2.32	44	2.38
95% C.I.	2.84	0.108	2.59	0.098	2.56	0.097
Max	218	9.8	209	8.8	182	9.6

Table 4.3: Path length

	Manual (m)	**Task Space** (m)	**JointSpace** (m)
Tip			
Mean	1.95	1.87	2.07
95% C.I.	0.087	0.082	0.078
Elbow			
Mean	0.82	0.81	0.76
95% C.I.	0.021	0.019	0.019

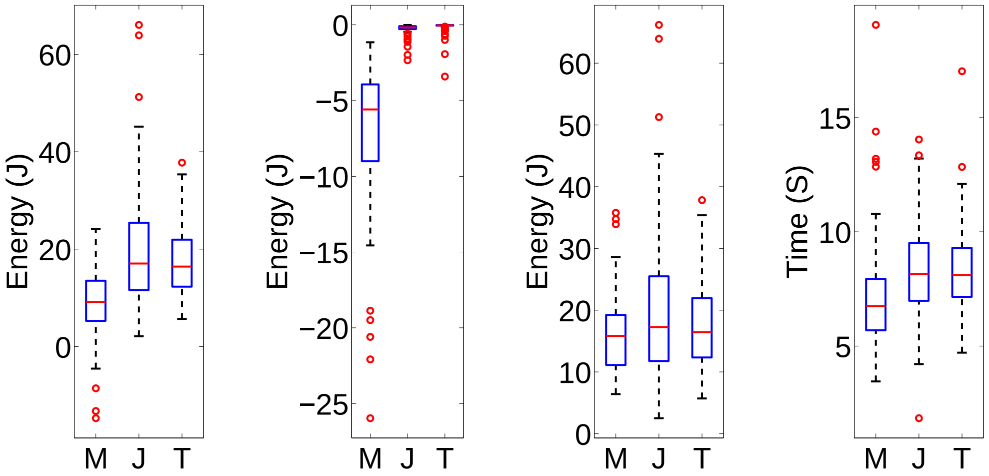

(a) (b) (c) (d)

Figure 4.5: Distribution of interaction energy and completion time. **a)** Total energy interaction **b)** negative energy interaction **c)** Positive energy interaction **d)** Completion time

Table 4.4: Task Completion Time

	Manal (s)	**Task Space** (s)	**Joint Space** (s)
Mean	7.0	8.1	8.4
95% C.I.	0.33	0.31	0.30
Max	19.1	14.1	17.05

statistically different for the other controllers. Task space control and joint space control showed no statistically significant difference between each other.

4.3.4 Interaction Power

The linear and angular power exchange at each sensor was calculated by multiplying the recorded force/torque by its respective velocity. The velocities we calculated at each sensor by differentiating the position of each sensor. Figure 4.6 shows the average power exchange for manual control, joint space control and task space control after

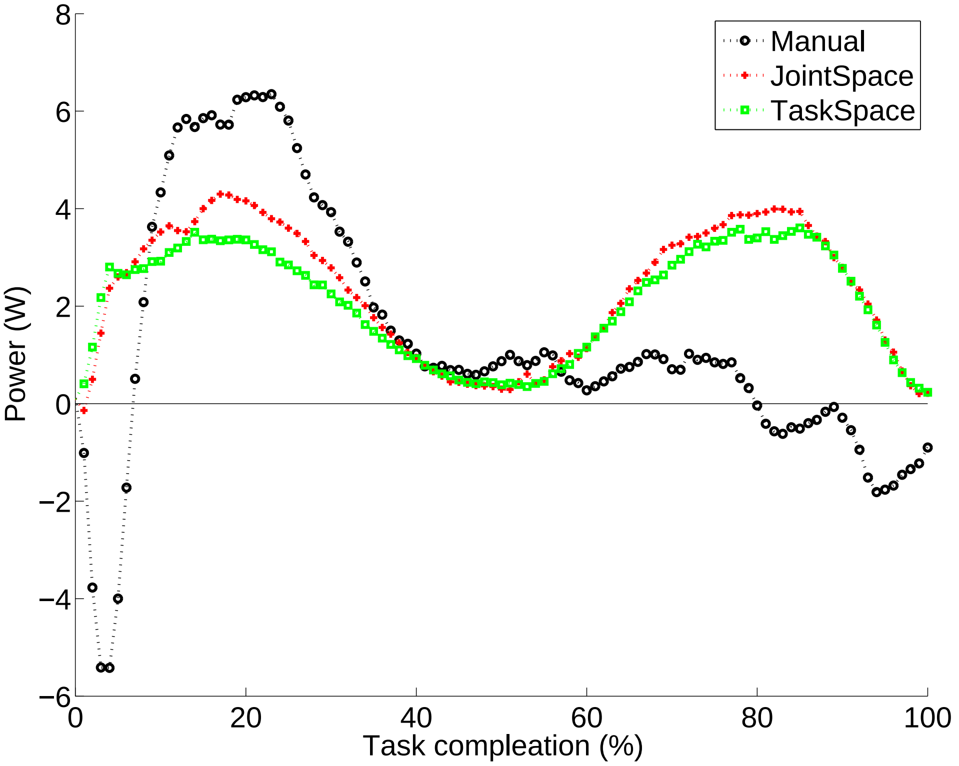

Figure 4.6: The average interaction power for no control, task space control and joint space control. For no control it can be seen that the interaction energy is much higher for the first half then the other two controllers, but close to zero or negative for the second half of the task. No control required high interaction poser to lift the device and little power to let it fall back down. In contrast the two admittance controllers required a uniform interaction power to both raise and lower the device and would be expected. both the task space control and joint space control had similar profiles with the task space being slightly smaller in magnitude.

they have been normalized with respect to time. For manual control a sharp drop in interaction power followed by steep rise in power characterizes the first half of the move (move to the target), the second half of the second half of the move (returning from the target) shows low then negative interaction power. The joint space and task space admittance controllers show a uniform rise and fall for of the interaction power when moving toward the target and returning from the target.

4.3.5 Interaction Energy

The energy exchange between the subject and exoskeleton was calculated for each trial by integrating the power. Additionally the negative and positive components of the energy were each computed separately. Figure 4.5 shows the distribution of energy for the over all energy (Fig. 4.5(a)), the negative energy component (Fig. 4.5(b)), and the positive energy component (Fig. 4.5(c)). Table 4.5 reports the mean with its 95% confidence interval along with the maximum value recorded. The differences in mean for the overall energy was statistically significant for all three groups. For the negative component, manual control was statically different from joint and task space control. Joint and task space control were not statistically different from each other. For the positive energy component, joint space control was statistically different from manual and task space control. Manual and task space control were not statistically different from one another.

4.4 Analysis

As expected the force that it took to control the exoskeleton was reduced with the use of admittance control. a total reduction of 45% from manual control to task space control and a 40% reduction from manual control to joint space control was achieved. It was clear that with the admittance controls much less force was required to move the device around. It was interesting to note that not only did the magnitude of the force change but also the distribution of forces. With manual control, the largest

Table 4.5: Interaction Energy

	Manual (J)	**Task Space** (J)	**JointSpace** (J)
Overall			
Mean	9.29	17.43	19.55
95% C.I.	1.11	1.01	1.04
Negative			
Mean	-6.92	-.098	-.025
95% C.I.	0.34	0.33	0.34
Positive			
Mean	16.21	17.52	19.81
95% C.I.	1.10	0.99	1.03

forces were at the upper arm followed by the handle and the smallest forces at the lower arm. Conversely, the admittance controllers had the highest forces in the handle, followed by the lower arm and lowest in the upper arm. To control the position of the device it would be expected that there would be higher forces at the handle and wrist, as these locations have more degrees of freedom and larger ranges of motion than the upper arm. With manual control, a large majority of the force is used to support the weight of the device at the upper arm and handle with a smaller portion of the force dedicated to control of the motion. At the wrist the force magnitude for manual control and the admittance controllers were comparable. Looking at the forces alone does not give any indication of a difference between the task space control and joint space control. Figure 4.6 shows the average power exchange between the subject and exoskeleton during reach tasks. It should be noted that this power is only the exchange of power between the two systems and does not say anything about the total power used by either system. In this figure it is easy to identify three distinct regions of motion. From 0% to about 40% of task completion the subject is raising the arm from their side up to the level of the target. From about 40% to 60%, the target is being engaged, and from about 60% to 100% the arm is being lowered back down to the side of the body. In region one we see that manual control has a sharp drop with a negative power peaking about -5.8W, followed by a steep increase to a positive power of around 6.5W and finally has a decline to around 1.0W. The sharp decrease is due to to the device falling slightly after the breaks were disengaged. The arm is then accelerated upwards to the level of the target increasing the power, finally the acceleration is decreased as the target is approached. Joint and task space control have a similar, but small in magnitude, rise and fall on the power curve without the initial drop as the controllers prevented the exoskeleton from falling when the breaks were released. In Region 2, the subjects are engaging the targets. for all three control types the power was low, between 0.5 and 1.0 watts. In this region the motion was much slower as the peg is inserted into the hole. Additionally the motion was in the transverse plane so gravitational forces were not in the direction of motion, making the power much lower for this region. The third region is the most interesting. For manual control, power is low and positive for about half the region and low and negative for the other half. As the subject lowers the arm, gravity pulls it in the same direction as the motion creating a very low power. The plots would indicate that initially the subject was moving slightly faster then gravity was pulling the arm down, then at about 80% of task completion, the subject began to slow the arm and gravity pulled the arm faster then they wanted to go. The two admittance controllers produce a power profile that is very similar to region one, where there is an increase to the power followed by a reduction to 0W. It would be easy to interpret this as meaning the admittance controllers made it harder to lower the arm, This would be an incorrect interpretation of the data. The power plot is power exchanged between the device and subject, not the power exerted by the subject. For an admittance controller the power exchange should always be positive, as the device should only move in the direction that you are pushing it. In fact having a similar power profile for region one and three shows uniform performance for both raising and lowering the arm.

The total energy for manual control is lowest for all the controllers. Because the admittance controllers have almost no negative power, we would expect them to have a higher energy then the manual control. It is more insightful to look at the negative and positive components of the energy and compare them separately. As expected the admittance controllers have almost no negative components and doesn't give us a lot of information to compare them. The positive energy component shows a statistically significant difference between the joint space and task space control. Task space control had about an 11.5% lower energy exchange then joint space control.

Interestingly, the completion time when control is added increases. Task space control saw a 16% increase in completion time, and joint space control saw a 20% increase. For the admittance controllers, there was a trade off in tuning the gains between fast open space movement and slower precise movement of inserting the peg. For open space movement large gains are desired so that a small force will create high velocities, to preserve stability, gains had to be limited, and when coupled with saturation limits to avoid integrator wind up, the maximum velocity was limited. On the other side when the tip was close to the target, smaller gains are desirable to allow greater control of the tip's position. With a linear gain, it is not possible to mutually satisfy both requirements and a trade off has to be made, resulting in a degradation in the ability to preform the task resulting in increased task completion time. There was no statistical difference between the task completion time for the joint space and task space control.

Tip and elbow path length was an area where the task space and joint space controllers differed. Task space control used a 10% shorter path length at the tip then joint space control. But joint space control had a 6.6% shorter path length at the elbow. It is difficult to interperate these results, as a shorter path can indicate a more direct efficient path. With longer path at the tip then the elbow one could argue that the task space control had a more efficient movement. However it is not the most direct efficient path that is desired with the exoskeleton, but the most natural movement for the user. The best way determine which controller produces the most natural path will be to record subject completing the same task without wearing the exoskeleton, then compare the motion. Without the restriction of kinematic constraints nor velocity limits from the controllers completion time for the task should be much less; however, it has been shown that neither joint angle selection or amplitude of the selected angle change much with differences in speed [90].

With an 11.5% reduction in interaction energy the task space controler is the more desirable control to have implemented. However task space control is a more complex algorithm, with the inverse kinematic equation needing to be solved, the desired position and orientation the wrist, and position of the elbow have to be explicitly calculated, and more gains tuned. However, it is easier to control the redundancy independently from the hand position/orientation if you are interested in studying the effects of differing swivel angels on movement. Limiting task space velocities uniformly in the work space is much easier to do with task space control as joint velocities do not map linearly to task space.

4.5 Discussion

It was found that both the task space and joint space controllers reduced the force required to move the exoskeleton. However they also increased the completion time for the given task. It would be desirable to improve the controller such that task completion time is at least as fast as when no control effort is applied. In the current experiments, the weights for all four sensors were set equal. It is worth exploring the effects of differing the weights of each sensor to see if improved results are achieved. The main limitation to increasing the speed is to increase the gains, however increasing the gains results in instability of the controllers. Other work [73] has shown that placing the HMI at the neural level can increase the achievable gains in the system by as much as double while still maintaining stable operation.

Other areas to further explore would be the necessity of four 6-axis force/torque sensors as well as the effect of loads on performance. Although it was discovered that a sensor is required at each location the body is in contact with the exoskeleton it is unclear whether the sensors have to all be 6 axis force torque sensors. The upper arm and lower arm have less then 6 DOF so it is expected that 6-axis force/torque sensors would not be needed. The 6 axis sensors are expensive and replacing one or two of then with cheaper sensors with fewer degrees of measurement would be desirable. Additionally exploring the effects of load on performance is another area of interest. For the current experiments, there was no load present at the tip of the device. We know that the gravitational load comprises the majority of the required force for low velocity reach activities so varying the load at the end effector should have a significant effect on the required torque for the device.

Chapter 5

SWIVEL PREDICTION

Since an important feature of an assistive robot is to provide synchronized movement with the human, its control mechanism should accommodate knowledge of natural human movement. Due to the lack of knowledge about the human motion planning mechanism, it is important to find a control mechanism that provides synchronized movement with the human. In spite of the redundancy of the human arm, natural hand movement reveals a unique pattern commonly seen in all humans[48][23]. Implying there is a hidden mechanism in natural hand movements. In this section, a new algorithm for selecting the swivel angle of the exoskeleton, such that the motion in free space matches the user's during reaching, tasks is presented. A motion capture study is then used to verify that the algorithm predicts natural human arm configuration, and finally the algorithm is applied to the exoskeleton device and is shown to reduce the interaction energy between the user and the device during reach tasks.

5.1 Background

Since grabbing and reaching tasks make up the majority of arm movements during daily life, we focus on a control mechanism that supports a natural human-robot arm interface for these types of motions. For decades, there has been a lot of research on redundant robot manipulators. Kinematically redundant robot manipulators enable various joint configurations for the given end effector position and orientation and allow for obstacle avoidance[61][12][51], singularity avoidance[7][72], joint limit control[50], torque optimization[8][34], dexterity optimization[43], and much more.

Liu et al.[50] proposed an improved motion planning scheme which provides proper joint configuration at key path points in the velocity level. However, unlike the conventional robotic manipulator, a robot such as an exoskeleton robot[67][62], which requires human-robot interaction, has to provide natural arm movement at the human robot interface so the operator feels as if the robot is a natural extension of their body. The control algorithms introduced so far provide proper joint configuration to the robotic manipulator when it interacts with the work space, but does not take into account the user's desired arm configuration. For this reason, other research proposes posture-based motion control strategies[20][21] based on the Donders' law, originally proposed for eye movements. Most of the work in this line of research focuses on the desired hand posture at a kinematic level given that the kinematic constraint is a target location.

Another line of research focuses on the kinematic strategy of the human arm based on the dynamic constraint such as amount of work and energy[35][1]. In this context, Soechting and his colleagues[79] proposed that the final arm postures were selected to minimize the amount of work required to move the hand from a starting location to the target position. The minimum-torque-change model is presented in [82][49].

More recently in[1], it is shown that arm posture, based on a particular target, is affected by both kinematics and dynamics and their relative contribution might be variable depending on the task complexity. Tao et al.[35] presented an inverse kinematic solution which defines the elbow rotation axis for natural arm movement by minimizing the total work done by joint torques. However as pointed out in [1], any single criteria cannot explain the human arm kinematic mechanism. Thus it is recommended that both kinematic and dynamic constraints should be constructively unified for better explanation of the hand movement.

All the criteria discovered so far are important in an engineering point of view and partially explain the human hand inverse kinematic mechanism. However due to the fundamental differences between robots and humans, it is difficult to fully model the human arm movement using the previously mentioned criteria. In addition to this, most of the inverse kinematic solutions require an iterative algorithm or well known optimization techniques, which are computationally demanding for real time robot control and prone to instability from the nature of ill-posed inverse problem. The proposed algorithm focuses on the functional difference between robot and human manipulators by closely observing human behavior. As a result, it is shown that natural hand postures for reaching activities is made to bring the hand efficiently to the mouth; based on this constraint a stable and precise realtime control algorithm is formulated. This algorithm provides an inverse solution for the arm posture for the entire movement instead of just at a goal or target location.

5.2 Method

For every movement, the human arm immediately forms a unique and repeatable swivel angle. To find the hidden mechanism inherently used by the human body, the functional differences between human and robot arms was observed. This lead to a crucial constraint for the inverse kinematic problem: robots are designed for specific tasks such as moving or reaching object without considering self powering and maintenance. Instead they are directly powered by an external energy source such as a battery or power cable and managed then by an engineer. On the other hand, the human arm is designed not only to manipulate objects but also to touch and feed the person. In other words, the human has to maintain their own body for survival and feeding and sensing play a critical role. Based on this observation the following hypothesis is formed:

Hypothesis 5.2.0.1. ***The redundancy of the human arm is defined to efficiently retract the hand to the mouth.***

Although the human does not always bring an object to their mouth, the human arm is unconsciously prepared to bring the hand there. One can easily observe this in a simple experiment. First, reach any target in free space naturally. Next, freeze the arm and rotate only the elbow joint. You can observe that your hand retracts to the area around mouth in most cases. This constraint is significantly different from other well known constraints based on target location or goal location of the hand. To translate hypothesis 5.2.0.1 into a mathematical representation, the swivel angle is chosen such that the projection of the longest axis of the manipulability ellipsoid of the hand onto the line going from the hand to the mouth is maximized.

5.2.1 Manipulability Ellipsoid

When we consider the different combination of joint velocities satisfying

$$\Sigma_{i=1}^{n} \dot{\theta}_i^{\,2} = 1 \tag{5.1}$$

the velocity at the hand resulting from the joint inputs will be described by an ellipse because of the directionally dependent scaling of the jacobian. The ellipse graphically depicts the directions in which the hand can move most easily[52]. The major axis of the manipulability ellipsoid for the arm can be described as follows:

Lemma 5.2.1. *Define plane S to be composed of the three points P_s, P_e, and P_w representing the shoulder, elbow and wrist joints in the arm's current configuration. The longest axis of the manipulability ellipsoid is then coincident with plane S and the magnitude (σ_1) of the longest axis of the manipulability ellipsoid is defined as*

$$\begin{aligned}
\sigma_1 &= \sqrt{\frac{((L_{ws}^2 + L_{we}^2) + (L_{ws}^2 + L_{we}^2)\, c_1)}{2}} \\
c_1 &= \sqrt{1 - c_2} \\
c_2 &= \frac{4L_{we}^2 L_{ws}^2 \sin(\varphi)^2}{(L_{ws}^2 + L_{we}^2)^2} \\
L_{ws} &= \|P_w - P_s\| \\
L_{we} &= \|P_w - P_e\|
\end{aligned}$$

Proof. Let us define a new frame with its origin at P_s, the z axis orthogonal to the plane S and the x axis pointing along the vector $(P_w - P_s)$. Then the relationship between the end effector velocity $\dot{\mathbf{P}} = [\dot{P_{wx}}\ \dot{P_{wy}}\ \dot{P_{wz}}]^T$ and the joint velocity $\dot{\theta}_{1234} = [\dot{\theta}_1\ \dot{\theta}_2\ \dot{\theta}_3\ \dot{\theta}_4]$ is defined as follows

$$\begin{aligned}
\dot{\mathbf{P}} &= \mathbf{J}\dot{\theta}_{1234} && (5.2)\\
&= [\mathbf{J}_1\ \mathbf{J}_2\ \mathbf{J}_3\ \mathbf{J}_4]\dot{\theta}_{1234} && (5.3)\\
&= \mathbf{J}_1\dot{\theta}_1 + \mathbf{J}2\dot{\theta}_2 + \mathbf{J}_3\dot{\theta}_3 + \mathbf{J}_4\dot{\theta}_4 && (5.4)\\
\mathbf{J}_i &= \begin{cases} \omega_i^{'} \times (P_w - P_s), i = 1,2,3 \\ \omega_i^{'} \times (P_w - P_e), i = 4 \end{cases} && (5.5)
\end{aligned}$$

where $\omega_i^{'}$ indicates the rotation axis of the ith joint in the new frame. By introducing a new variable φ to represent the elbow angle in $\mathbf{J}_4$ and using the fact that $\omega_1^{'} = \vec{x}$, $\omega_2^{'} = \vec{y}$ and $\omega_3^{'} = \vec{z}$, we have

$$\begin{aligned}
\mathbf{J}_1 &= \omega_1^{'} \times (P_w - P_s) = \vec{x} \times (P_w - P_s) = 0 && (5.6)\\
\mathbf{J}_2 &= \|P_w - P_s\|[0\ 0\ -1]^T && (5.7)\\
\mathbf{J}_3 &= \|P_w - P_s\|[0\ 1\ 0]^T && (5.8)\\
\mathbf{J}_4 &= \|P_w - P_e\|[-\sin(\varphi)\ \ \cos(\varphi)\ 0]^T && (5.9)
\end{aligned}$$

Then by plugging Eq.5.6, Eq.5.7, Eq.5.8 and Eq.5.9 into Eq.5.4, we have

$$\begin{aligned}
\dot{\mathbf{P}} &= \mathbf{J}_2\dot{\theta}_2 + \mathbf{J}_3\dot{\theta}_3 + \mathbf{J}_4\dot{\theta}_4 && (5.10)\\
&= [\mathbf{J}_2\ \mathbf{J}_3\ \mathbf{J}_4]\dot{\theta}_{234} && (5.11)\\
&= \begin{pmatrix} 0 & 0 & -L_{we}\sin(\varphi) \\ 0 & L_{ws} & L_{we}\cos(\varphi) \\ -L_{ws} & 0 & 0 \end{pmatrix} \dot{\theta}_{234} && (5.12)\\
&= \mathbf{J}_{234}\dot{\theta}_{234} && (5.13)
\end{aligned}$$

where $L_{ws} = \|P_w - P_s\|$ and $L_{we} = \|P_w - P_e\|$. According to the singular value decomposition, $\mathbf{J}_{234}$ can be represented as

$$\mathbf{J}_{234} = \mathbf{UDV}^T \tag{5.14}$$

where $\mathbf{U} = [u_1 \ u_2 \ u_3]$, $\mathbf{V} = [v_1 \ v_2 \ v_3]$, and $\mathbf{D} = diag[\sigma_1 \ \sigma_2 \ \sigma_3]$. The u_i in the left singular vector $\mathbf{U}$ indicates one of the three axis constructing the manipulability ellipsoid and the singular value σ_i in $\mathbf{D}$ indicates the magnitude of the u_i. Note that u_i and σ_i are the eigenvectors and square root of the non-zero eigenvalues of $\mathbf{J}_{234} \cdot \mathbf{J}_{234}^*$. Then we solve $\det\left(\mathbf{J}_{234} \cdot \mathbf{J}_{234}^* - \lambda \mathbf{I}\right) = 0$ to obtain u_i and $\sigma_i \left(= \sqrt{\lambda_i}\right)$. According to the rule of Sarrus:

$$\begin{aligned}
\lambda_{1,2} &= \frac{(L_{ws}^2 + L_{we}^2) \pm (L_{ws}^2 + L_{we}^2)\, c_1}{2}\ , \quad (\lambda_1 > \lambda_2) \\
c_1 &= \sqrt{1 - c_2} \\
{}_2 &= \frac{4 L_{we}^2 L_{ws}^2 \sin(\varphi)^2}{\left(L_{ws}^2 + L_{we}^2\right)^2} \\
\lambda_3 &= L_{ws}^2
\end{aligned}$$

It can be shown that $0 \leq c_2 \leq 1$ and $0 \leq c_1 \leq 1$ such that $\lambda_{1,2}$ are not complex numbers. To figure out the relationship among λ_1, λ_2 and λ_3, we consider two cases when $L_{ws} \geq L_{we}$ and $L_{ws} < L_{we}$ individually.

case1:$L_{ws} \geq L_{we}$

$$\begin{aligned}
\lambda_1 - \lambda_3 &= \frac{\left(L_{ws}^2 + L_{we}^2\right) + \left(L_{ws}^2 + L_{we}^2\right) c_1}{2} - L_{ws}^2 \\
&\geq \frac{\left(L_{we}^2 - L_{ws}^2\right) + \left(L_{ws}^2 + L_{we}^2\right) c_{min1}}{2} \\
&= \frac{\left(L_{we}^2 - L_{ws}^2\right) + \left(L_{ws}^2 + L_{we}^2\right) \sqrt{1 - c_{max2}}}{2} \\
&= \frac{\left(L_{we}^2 - L_{ws}^2\right) + \left(L_{ws}^2 + L_{we}^2\right) \sqrt{1 - \frac{4L_{we}^2 L_{ws}^2}{\left(L_{ws}^2 + L_{we}^2\right)^2}}}{2} \\
&= \frac{\left(L_{we}^2 - L_{ws}^2\right) + \sqrt{\left(L_{ws}^2 - L_{we}^2\right)^2}}{2} = 0 \qquad (5.15)
\end{aligned}$$

where c_{min1} and c_{max2} mean the minimum and maximum value of c_1 and c_2 respectively. The c_{max2} applied to Eq.5.15 is defined as

$$c_{max2} = \max \frac{4L_{we}^2 L_{ws}^2 \sin(\varphi)^2}{\left(L_{ws}^2 + L_{we}^2\right)^2} = \frac{4L_{we}^2 L_{ws}^2}{\left(L_{ws}^2 + L_{we}^2\right)^2}$$

case2:$L_{ws} < L_{we}$

$$\begin{aligned}
\lambda_1 - \lambda_3 &= \frac{\left(L_{ws}^2 + L_{we}^2\right) + \left(L_{ws}^2 + L_{we}^2\right) c_1}{2} - L_{ws}^2 \\
&= \frac{\left(1 + c_1\right)\left(L_{ws}^2 + L_{we}^2\right)}{2} - L_{ws}^2 \\
&\geq \frac{\left(1 + c_{min1}\right)\left(L_{ws}^2 + L_{we}^2\right)}{2} - L_{ws}^2 \\
&= \frac{\left(L_{ws}^2 + L_{we}^2\right)}{2} - L_{ws}^2 \\
&= \frac{\left(L_{we}^2 - L_{ws}^2\right)}{2} \geq 0 \qquad (5.16)
\end{aligned}$$

where the inequality in Eq.5.16 comes from the fact that $c_{min1} = \min[c_1] = 0$. The last line of inequality is valid since $L_{ws} < L_{we}$. Therefore we can conclude that $\lambda_1 \geq \lambda_3$ in all ranges of L_{ws}. It implies that the magnitude of the longest axis in the manipulability ellipsoid is

$$\sigma_1 = \sqrt{\lambda_1} = \sqrt{\frac{(L_{ws}^2 + L_{we}^2) + (L_{ws}^2 + L_{we}^2)\, c_1}{2}} \tag{5.17}$$

Based on the fact that the direction of the major axis of the manipulability ellipsoid corresponds to the eigenvector of the following Eq.5.18, the eigenvector ν_1 is obtained by applying the corresponding eigenvalue λ_1 to λ in Eq.5.18.

$$(\mathbf{J}_{234} \cdot \mathbf{J}_{234}^*)\, \mathbf{X} = \lambda \mathbf{X}, \quad \mathbf{X} = [x\ y\ z]^T \tag{5.18}$$

Then the direction of the eigenvector $\mathbf{X}$ in Eq.5.18 is defined as

$$\begin{aligned} y &= \frac{\lambda_1 + L_{we}^2 \sin(\varphi)\cos(\varphi)}{-L_{we}^2 \sin(\varphi)^2} x && (5.19) \\ &= \left(-\frac{\lambda_1}{L_{we}^2 \sin(\varphi)^2} - \frac{1}{\tan(\varphi)} \right) x && (5.20) \\ z &= 0 && (5.21) \end{aligned}$$

Considering the joint limit of the exoskeleton robot[75], we can assume that $0 < \varphi \leq \pi/2$. Note that when $\varphi = 0$, the arm is in a singular position. Then based on the fact that $\lambda_1 > 0$, the slope in Eq.5.19 becomes negative. $\square$

5.2.2 Swivel angle selection

We would like to find the swivel angle that maximizes the projection of the long axis of the manipulability ellipsoid onto the line that goes from the hand to the mouth. To do this, first define a point P_m that represents the location of the mouth. The vector $\vec{f}$ can then be defined as $P_m - P_w$. The projection of the manipulability ellipsoid is then maximized when the vector $\vec{f}$ is coincident with the plane S and the swivel angle is found as follows:

$$\vec{f} = P_w - P_m \tag{5.22}$$

$$\vec{f}' = \vec{f} - \left(\vec{f} \cdot \vec{n}\right) \vec{n} \tag{5.23}$$

$$\phi = \arctan 2 \left(\vec{n} \cdot \left(\vec{f}' \times \vec{u}\right), \vec{f}' \cdot \vec{u}\right) \tag{5.24}$$

Proof. The magnitude of the projection of the long axis of the manipuability ellipsoid ($\vec{\nu}_1(\phi)$) onto $\vec{f}$ is equal to:

$$\vec{\nu}_1(\phi) \cdot \vec{f}$$

From Lemma 5.2.1 we know that $\vec{\nu}_1$ is coincident with plane S. In a coordinate frame, with the z axis normal to plane S and the x axis equal to $\vec{n}$, the vector $\vec{\nu}_1$ is constant and its value is given in equation 5.19 - 5.21. The vector $\vec{f}$ can be put into that coordinate frame with the following coordinate transformation:

$$\begin{bmatrix} \vec{n}^T \\ (\vec{u}\cos(\phi) + \vec{v}\sin(\phi))^T \\ (\vec{u}\sin(\phi) + \vec{v}\cos(\phi))^T \end{bmatrix} \vec{f} \tag{5.25}$$

Then

$$\vec{\nu}_1 \cdot \vec{f} = \left[\vec{n} \cdot \vec{f}\right] \nu_x \tag{5.26}$$

$$+ \left[(\vec{u}\cos(\phi) + \vec{v}\sin(\phi)) \cdot \vec{f}\right] \nu_y \tag{5.27}$$

$$+ \left[(\vec{u}\sin(\phi) + \vec{v}\cos(\phi)) \cdot \vec{f}\right] 0 \tag{5.28}$$

The first component of the projection (5.26) is a constant, the second component (5.27) is a function of ϕ, and the last component (5.28) is equal to zero. To maximize the projection, ϕ should be chosen such that (5.27) has that largest possible magnitude with the same sign as (5.26). Because the coordinate change in equation (5.25) cannot change the magnitude of the original vector $\vec{f}$ and the first component of the projection (5.26) is constant, the magnitude of the second component (5.27) is maximized when the magnitude of $[(\vec{u}\sin(\phi) + \vec{v}\cos(\phi)) \cdot \vec{f}]$ in minimized. This value is the z component of the vector $\vec{f}$ in the specified coordinate frame and is equal to zero when $\vec{f}$ is coincident with the plane S, maximizing the magnitude of (5.27). The vector $\vec{f}$ is coincident with plane S for two values of ϕ that are π radians apart. The sign of (5.27) will be positive for one and negative for the other. The value of ϕ that makes (5.27) have the same sign of (5.26) and $\vec{f}$ coincident with S maximizes the projection.

$\square$

5.3 Verification

It is necessary to verify the above hypothesis before implementing it as a control algorithm for the exoskeleton device. To do this, a motion capture experiment where subjects performed predefined reach tasks in open space was performed. the actual swivel angles that the subjects selected during thoes task were then calculated. After an optimization of the point P_m was performed for each subject, the estimated swivel angle was calculated using equation 5.24. Finally, the actual vs. estimate swivels angel were then compared.

5.3.1 System and Protocol

The experimental setup is shown in Fig.5.1. The kinematic data of the human arm was collected using the Phasespace motion capture system (Phasespace, Inc.), which was equipped with eight cameras providing a millimeter accuracy at a distance of three meters. A 240Hz sampling rate was chosen to give excellent data density around potential occlusions that may occur. Active red LED markers were attached to a subject at key anatomical locations which includes the shoulder, elbow, wrist, and chest [Fig.5.1(b)]. Each subject was instructed to perform a reaching task described

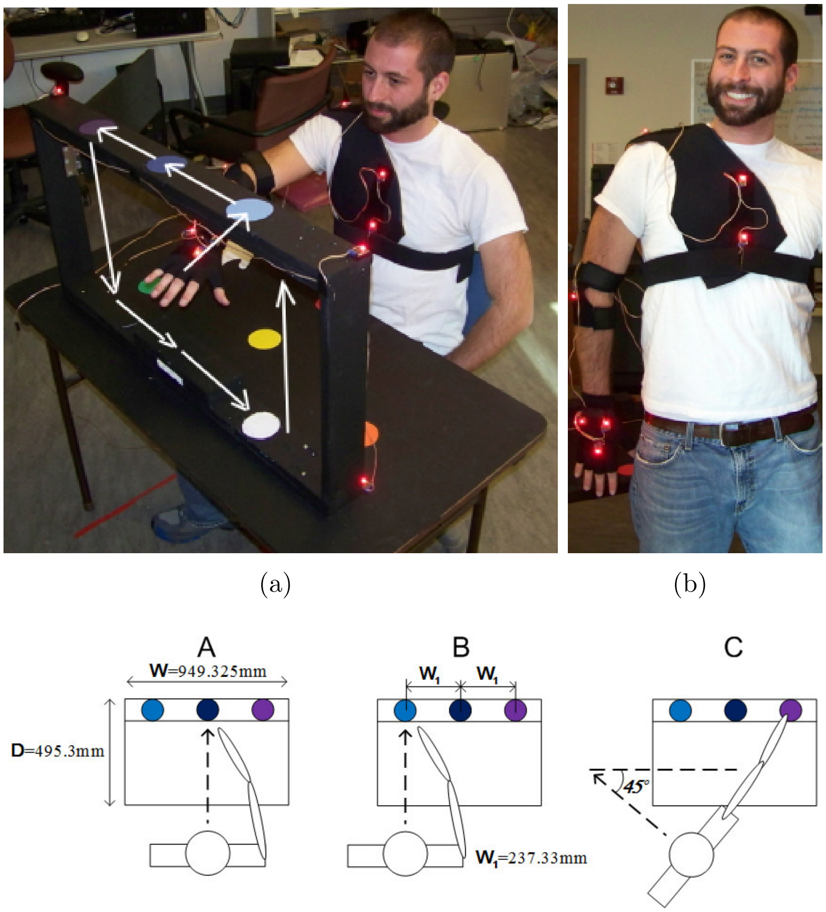

(a) (b)

(c)

Figure 5.1: **a)** Hand trajectory for data collection **b)** Positions of LED markers: Shoulder(Arcomioclavicular joint), Elbow(Lateral edge of the Ulna), Wrist(Medial & Lateral edge of the distal end of the radius & ulna), Palm(between 2 & 3 metacarples) and Torso(Upper & lower sternum) **c)** Top view of three different tasks. Height of table-top to top-of-shelf = 501.65mm, Height of table-top from ground = 736.6mm.

in Fig.5.1(c). In detail, subjects placed their hand at the center of the task space and reached targets sequentially following the arrows. There were five target locations marked with different colors. Three colored circles were on an upper side and two on the lower side of the rectangular frame. Pointing to each of the five targets in turn was regarded as finishing one circuit. Each subject accomplished five circuits for each of three different experimental conditions by moving their hand with a smooth path at a self directed pace as illustrated in Fig.5.1(a). The three experimental conditions were associated with the alignment of the torso in task space and designed to cover most of the right hand work space. In condition (A) and (B), the torso was facing the center and the left blue circle of the task space respectively. The final condition (C) is when the torso was turned forty five degree counterclockwise off the Sagittal alignment and the abducted hand points to the right purple circle. Five right handed and healthy subjects(three male and two female subjects with an average height of 175.76cm) aged from 20 to 38 participated in the experiment.

5.3.2 *Optimum P_m Estimation*

Due to the differences between subjects, it is important to optimally locate P_m for each subject. Torsional motion is not included in our model of the arm, and subjects were instructed to only move the arm and keep the torso stationary during data collection. For these reasons it is assumed that that the Sagittal plane of the body is in a fixed orientation during data collection with only minor translational motion. To measure the translational motion, a marker P_{ch} was placed on the chest. If we attach a reference frame F_{ch} on P_{ch}, P_m is translated in F_{ch} by a fixed amount on the Sagittal plane. By doing this, the upper body remains rigid and consequently P_m can be represented as a function of time t,

$$P_m(t) = P_{ch}(t) + P_o \tag{5.29}$$

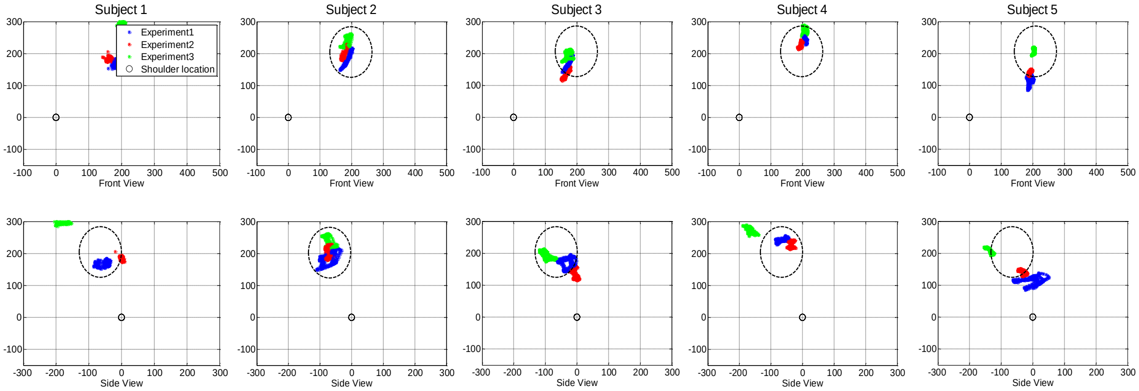

Figure 5.2: Upper row and lower row indicate the front and side view of P_m with respect to the shoulder(reference frame) in millimeter scale. Dotted circles are approximated head shape for reference. P_m is individually estimated for each experiment

where P_o is the fixed amount of translation from P_{ch} with respect to F_{ch}. Note that $P_{ch}(t)$ becomes a function of time t because the upper body with respect to the global reference frame F_G slightly varies in each experiment. Then according to Eq.5.24, the optimum offset P_o is chosen to minimize the difference between $\phi(t)_{est}$, the estimated swivel angle based on Eq.5.24, the calculated swivel angle from the measured joint positions and $\phi(t)_{act}$.

$$P_o\left(x_{center}, y_{opt}, z_{opt}\right) = \arg\min_{y,z\in U_s} \frac{1}{T}\int_{t_x}^{t_x+T} |\phi(t)_{act} - \phi(t)_{est}|dt \qquad (5.30)$$

where U_s and x_{center} in Eq.5.30 mean the (y, z) coordinate pairs on the Sagittal plane and the x coordinate from $P_{ch}(t)$. Also note that T in Eq.5.30 corresponds to 1/5 of the total recording for individual reaching tasks. For the rest of the data sets, the estimated P_o is applied to $P_m(t)$, Fig.5.2 shows the optimum $P_m(t)$ estimated for three different experiments with respect to the global frame F_G. In Fig.5.2, we find out that P_m is clustered around the facial region. The estimated P_m will be used in the following section to estimate the swivel angle.

5.3.3 Performance of Swivel Angle Estimation

In order to assess the estimation performance, the swivel angles are estimated using the wrist position data. The estimates are then compared with calculated swivel angles which are computed from the motion capture data. Note that the LED markers for the motion capture system are attached to the surface of the human body closest to the actual joint location and the collected data is used as the joint location data. This may cause an extra amount of estimation error.

Fig.5.3 presents the comparison result for all five subjects and three types of experiments. The results show that the estimated swivel angle is very close to the calculated one. To quantitatively evaluate the estimation performance, the standard deviation of the absolute estimation errors are provided with absolute error mean-averaged over all the recorded data from each subject in Table.5.1. In all cases, the standard deviation and mean value of absolute estimation error is less than five degrees. Considering the imperfect joint location and measurement error of the motion capture system, estimation error in Table.5.1 can be regarded as precise estimation results. The result can be improved by including dynamic constraint or considering P_m as an area instead of a point. However unlike the experiments 2 and 3, estimation results of experiment 1 in Fig.5.3 are slightly uncorrelated with the calculated swivel angles. This is because the left side targets are at the left edge of the right arm work space, which causes unnecessary torsional movement.

5.4 Application

The motion capture study showed a good correlation between the estimated swivel angle and the recorded one. The results provide good confidence that the algorithms can work on the exoskeleton system as part of a control structure. In this section, the swivel angel estimation method is integrated into the admittance control structure and an experiment is performed to compare the performance of the controller with

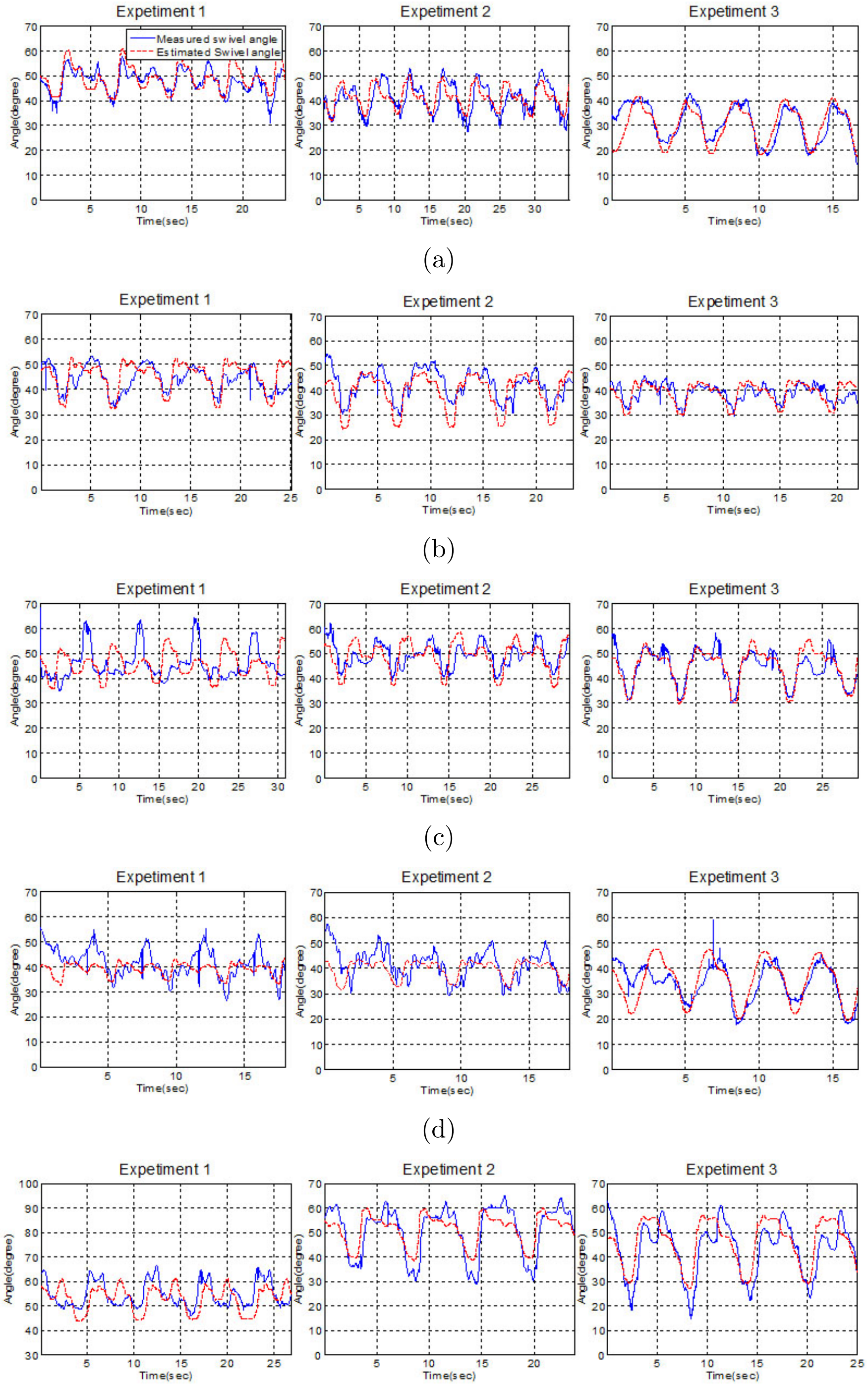

(a)

(b)

(c)

(d)

(e)

Figure 5.3: Comparison between estimated swivel angle (Red dotted line) and measured swivel angle (Blue line) for five different subjects.

Table 5.1: Estimation Error

Subject	$P_o(mm)$ (y_{opt}, z_{opt})	Trial	Standard Deviation of Error Exp 1	 Exp 2	 Exp 3	Mean error
1	(-160, 280)	#1	2.344°	2.720°	3.769°	3.024°
		#2	3.071°	3.473°	2.768°	
2	(-140, 320)	#1	2.337°	2.579°	1.365°	3.516°
		#2	2.351°	3.062°	1.951°	
3	(-70, 290)	#1	3.395°	2.756°	2.340°	4.103°
		#2	4.705°	2.840°	2.474°	
4	(-140, 330)	#1	2.817°	2.564°	3.010°	3.525°
		#2	3.088°	2.218°	1.914°	
5	(-60, 220)	#1	2.740°	3.225°	3.501°	4.739°
		#2	2.829°	2.843°	3.663°	
Total				2.824°		3.781°

and without the estimation algorithm integrated into the control. Before that can happen, the joint limits of the system have to be related to the swivel angle to avoid driving the system to an unreachable location.

5.4.1 Joint Limits

When we solve the inverse kinematic equation, we must select a desired wrist position and orientation as well as a desired swivel angle. The wrist position and orientation will be dictated by the desired task and the swivel angle is selected to create a natural arm posture for that task. Wearable robotic system are subject to joint limitations and it is desirable to relate the swivel angle to the joint limits. This can be accomplished by calculating the values of ϕ where the joints are at their limits to determine boundaries for the intervals of valid swivel angles. Due to the symmetry of the model, joints five, six, and seven are found in a similar manner as joints one, two, and three. Therefore only a treatment of the first three joints is presented. Using a four step process, the interval of ϕ that, for a particular wrist position and orientation, results in valid joint configurations can easily be calculated [56].

Step 1: Calculate β

Depending on the desired location of P_w there are three different types of solution sets. To determine which set the problem is in, calculate β, the angle between the the vectors $\vec{n}$ and $\vec{\omega}_1$:

$$\beta = acos(\vec{\omega}_1 \cdot \vec{n}) \tag{5.31}$$

The three cases, shown in fig. 5.4, correspond to when $\beta > \alpha$, $\beta = \alpha$, and $\beta < \alpha$. The first case ($\beta > \alpha$) is the most common and occurs when the first rotation axis ($\vec{\omega}_1$) is outside the elbow circle. The next case ($\beta = \alpha$) is the least common and occurs when $\vec{\omega}_1$ pierces the perimeter of the elbow circle. In this configuration, there is a value of ϕ that puts the device into a singular position. The last case ($\beta < \alpha$) occurs when $\vec{\omega}_1$ is inside the elbow circle.

Step 2: Calculate Joint Minimum and Maximum

For a particular P_w the range of each joint as ϕ rotates in the interval $[0, 2\pi]$ will be equal to 2π or less then or equal to π. The exact minimum and maximum can be computed by establishing a reference angle within the joints range of motion and calculating the deviation from that reference.

Reference Angle A convenient reference angle for θ_1 and θ_2 is the angle formed when the elbow is located at $P_{e_r} = (U\vec{n})$. This corresponds to when the elbow is on the line that is colinear with the one going from P_s to P_w. The references (θ_{1_r},θ_{2_r}), can be found by solving the following equation:

$$T_1 T_2 P_{e_0} = P_{e_r} \tag{5.32}$$

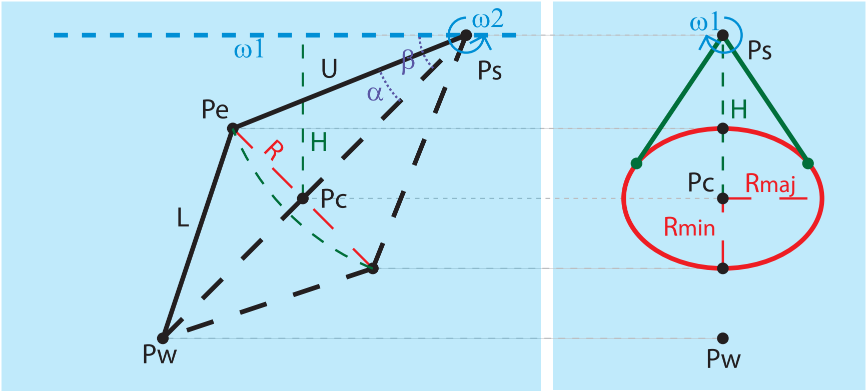

(a) $\beta > \alpha$

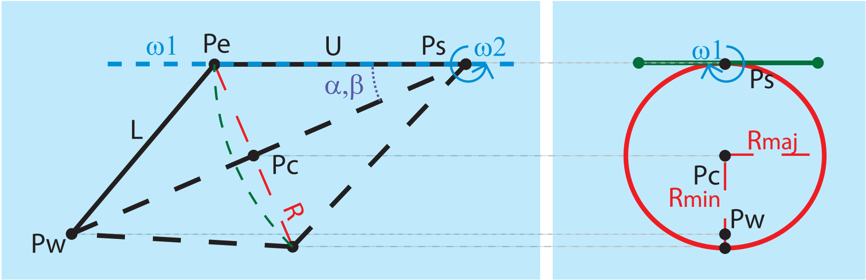

(b) $\beta = \alpha$

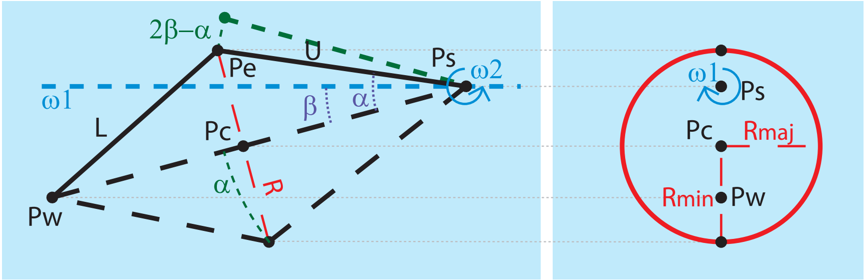

(c) $\beta < \alpha$

Figure 5.4: Planes A and B are normal to the vectors ω_2 and ω_1, respectively, and both pass through the point P_s. a) When $\beta > \alpha$ the range of θ_1 is the angle of the lines that pass through P_s and are tangent to the elliptical projection of the elbow circle. The range of θ_2 is equal to 2α. b) When $\beta = \alpha$ the point P_s is on the projection of the elbow circle and the angle of the tangent lines is π, note that the device will be singular for some value of ϕ in this configuration. The range of θ_2 is 2α. c) When $\beta < \alpha$ the point P_s is inside the projection of the elbow circle and the lines passing through this point will never be tangent to the ellipse. The range of θ_1 is 2π. The range of θ_2 will be $\alpha + 2\beta - \alpha = 2\beta$.

This equation is in the form of equation (D.1) of the appendix and can be immediately solved. This has multiple solutions, chose the negative sign in (D.2) to be consistent with the earlier selections. The reference angle θ_{3_r} will be $\frac{\pi}{2}$ when $P_{w_x} < 0$ and $-\frac{\pi}{2}$ when $P_{w_x} \geq 0$.

Joint Range The range of each joint depends on the value of β. The value of the range can be determined through geometry (fig. 5.4). $\delta\theta_1$ is the angle of the line that passes through P_s and is tangent to the elliptical projection of the elbow circle onto the plane normal to ω_1. $\delta\theta_2$ is the angle between the line P_{e_r}, and $\delta\theta_3$ (not pictured) is the angle between the projection of an ellipse on to the plane normal to ω_3 in a similar manner to $\delta\theta_1$. When $\beta > \alpha$

$$\delta\theta_1 = \pm atan\left(\sqrt{\frac{R_{1_{maj}}^2}{H_1^2 - R_{1_{min}}^2}}\right) \tag{5.33}$$

$$\delta\theta_2 = \pm\alpha \qquad \delta\theta_3 = \pm\pi \tag{5.34}$$

Where $H_1 = ||P_c - (P_c \cdot \vec{\omega}_1)\vec{\omega}_1||$ which is the magnitude of the projection of P_c, $R_{1_{maj}} = R$, and $R_{1_{min}} = Rcos(\beta)$ are the major and minor axes of the ellipse (fig. 5.4(a)). For $\delta\theta_3$, P_s is inside the projection of the ellipse and no line is tangent. When $\beta = \alpha$ (fig. 5.4(b))

$$\delta\theta_1 = \pm\frac{\pi}{2} \qquad \delta\theta_2 = \pm\alpha \qquad \delta\theta_3 = \pm\frac{\pi}{2} \tag{5.35}$$

In this case the point of reference for both ellipses are on the ellipse and the tangent line is $\frac{\pi}{2}$. When $\beta < \alpha$ (fig. 5.4(c))

$$\delta\theta_1 = \pm\pi \qquad \delta\theta_2 = \pm\alpha, \mp(2\beta - \alpha) \tag{5.36}$$

$$\delta\theta_3 = atan\left(\sqrt{\frac{R_{3_{min}}^2}{H_3^2 - R_{3_{maj}}^2}}\right) \tag{5.37}$$

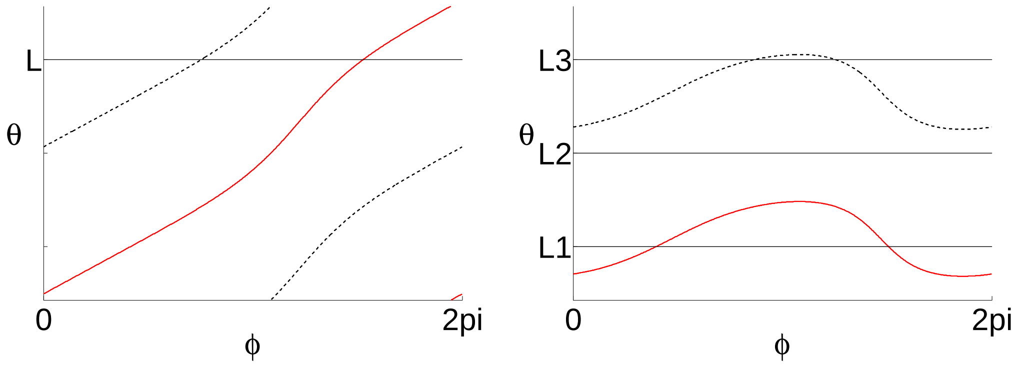

(a) (b)

Figure 5.5: Intersection of joint limit L with θ, the dashed black and solid red lines represent the multiple possible solution for the inverse problem. **a)** If the joint range is equal to 2π both the valid and invalid solution set for θ will intersect the joint limit L exactly once each. In this case you must chose the valid solution. **b)** If the joint range is less then 2π there are three possible intersection cases. 1) The joint limit $L1$ intersects the valid solution for θ in two places (possibly a double root). This makes 2 real and valid solutions. 2)The joint limit $L2$ dose not intersect either solution. This makes two imaginary solutions. 3)The joint limit $L3$ intersects the invalid solution for θ in two places. This makes two real but invalid solutions.

Where $H_3 = Wsin(\alpha) + \left[\frac{Wsin(\beta)}{2*cos(\alpha+\beta)} - \frac{Wsin(\beta)}{2*cos(\alpha-\beta)}\right]$. $R_{3_{maj}} = \left[\frac{Wsin(\beta)}{2*cos(\alpha-\beta)} + \frac{Wsin(\beta)}{2*cos(\alpha+\beta)}\right]$ and $R_{3_{min}} = R_{3_{maj}}\sqrt{1 - \left(\frac{sin(\alpha)}{cos(\beta)}\right)^2}$. $\delta\theta_2$ will be the top sign if $P_{w_x} > 0$ and the bottom sign otherwise.

Step 3: Joint Limit Intersection

Determining the value(s) of ϕ that result in the joint being equal to the joint limits (L_i) will establish the boundaries for the interval of ϕ that will result in valid joint configurations. There will be four solutions for each joint (two for the maximum and two for the minimum limit) but not all solutions will be valid.

Valid Solution There are four possible cases. The first case is when the range of θ is 2π. In this case there will always be one real valid solution, and one real invalid solution for each limit. The invalid solution represents the intersection with θ from the unselected IK solutions from eqn. (2.4) and (2.5). This case is represented in fig. 5.5(a). The other three cases are when the range of θ is less then or equal to π. Then, there may be 2 real (possibly double root) valid solutions, 2 real invalid solutions, or 2 imaginary invalid solutions. The two real invalid solutions are from the intersections of θ with the unselected IK solutions and the imaginary solution represent when neither the selected or unselected IK solution intersect with L_i. Figure 5.5(b) shows the last three cases. If the joint limit is with in the range of the joint:

$$(\theta_{i_r} - \delta\theta_i) \quad \geq L_i \geq \quad (\theta_{i_r} + \delta\theta_i) \tag{5.38}$$

then the solutions are valid. Once it is determined how many of the solutions are valid the values need to be calculated.

Calculate Intersection Values To calculate ϕ such that θ_i is equal to L_i, set θ_i equal to L_i and solve eqn. (2.4). This equation is not redundant with one joint angle selected. For the first three joints, we will begin by decomposing (2.4) by postmultiplying by P_{w_0}. Since P_{w_0} is an eigen vector of the last three joints with an associated eigen value of 1, (2.4) becomes:

$$T_1 T_2 T_3 T_4 P_{w_0} \quad = \quad P_w \tag{5.39}$$

This equation can further be decomposed to the form of (D.1) once θ_i is set to L_i, which will allow for the immediate solution of $\theta_{1_{Li}}$ and $\theta_{2_{Li}}$ which are the angels of joints one and two at joint limit i. Then ϕ_{Li} can be solved using eqn. (2.5) and (1.10).

L_1 - Given the joint limit L_1, the matrix T_1 is constant. By premultiplying (5.39) by T_1^{-1} we get:

$$T_2 T_3 (T_4 P_{w_0}) \quad = \quad (T_1^{-1} P_w) \tag{5.40}$$

which is in the form of (D.1) where $P_0 = (T_4 P_w)$, $P_d = (T_1^{-1} P_w)$, the rotation intersection is P_s, and the rotation axes are $\vec{\omega}_2$ and $\vec{\omega}_3$. If $\beta \geq \alpha$ then both solutions to (5.40) will be valid if eqn (5.38) is satisfied for $i = 1$. If $\beta < \alpha$, then the positive sign in (D.2) represents the valid solution.

L_2 - Given the joint limit L_2, the matrix T_2 is constant. By performing a change of coordinates on T_2, eqn. (5.39) can put in the form of (D.1)

$$\begin{aligned} T_1 T_{23} (T_2 T_4 P_{w_0}) \quad &= \quad (P_w) && (5.41) \\ T_{23} \quad &= \quad T_2 T_3 T_2^{-1} && (5.42) \end{aligned}$$

Where $P_0 = (T_2 T_4 P_w)$, $P_d = P_w$, the intersection location is P_s, and the rotation axis are $\vec{\omega}_1$ and $R_2 \vec{\omega}_3$. If eqn. (5.38) is satisfied for $i = 2$, then both solutions to (5.41) will be valid.

L_3 - Given L_3, the matrix T_3 is constant and eqn, (5.39) is already in the form of (D.1).

$$T_1 T_2 (T_3 T_4 P_{w_0}) \quad = \quad (P_w) \tag{5.43}$$

Where $P_0 = (T_3 T_4 P_w)$, $P_d = (P_w)$, the rotation intersection is P_s, and the rotation axes are $\vec{\omega}_1$ and $\vec{\omega}_2$. If $\beta \leq \alpha$ then both solutions to (5.40) will be valid if eqn (5.38) is satisfied for $i = 3$. If $\beta > \alpha$, then the negative sign in (D.2) represents the valid solution.

After the intersections are found that define intervals of ϕ, we must determine which intervals are invalid and which of the valid intervals we would like to work in.

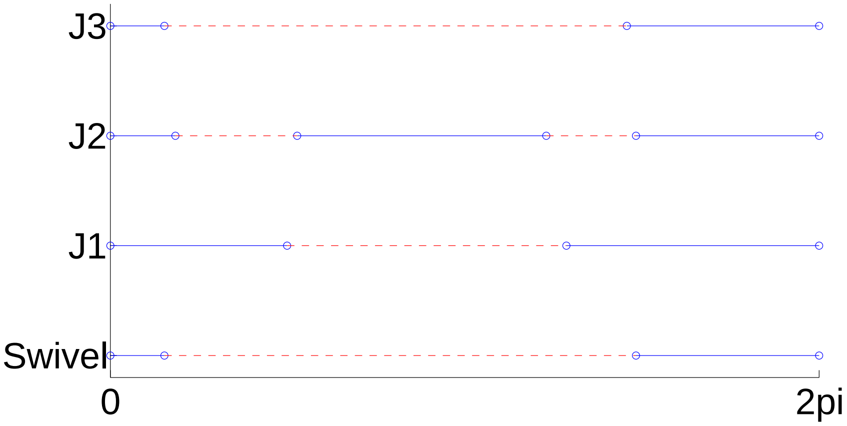

Figure 5.6: Value of ϕ that produce valid joint limits (solid blue) and invalid joint limits (dashed red). The valid interval of the swivel angle is the intersection of the valid intervals of ϕ for each joint.

Step 4: Intervals

For each joint there is up to four valid solutions for ϕ_{Li}. These solutions mark the boundary between the intervals of ϕ that result in valid joint configurations and those that result in joint configurations that are outside joint limits. Because ϕ wraps around at 2π the number of intervals will be equal to the number of valid solutions for ϕ_{Li}. The intervals will alternate between valid and invalid, so testing one value of ϕ is enough to determine which of the intervals are valid.

Taking the intersection of every valid set for each of the six joints results in a single valid set of intervals of ϕ where all joint limits are mutually satisfied (fig. 5.6). Because the functions are continuous, it is not possible to jump from one interval to another unless you are in a singular position. After selecting an initial position the robot is restricted to live in a particular interval within the set.

5.4.2 Admittance control with swivel estimation

The task space admittance controller from section 4.1.1 was modified to include the swivel estimation as part of the controller. To do this, equation 4.24 was changed from:

$$\phi \;=\; k_p\,\vec{\tau_e} + k_i \int \vec{\tau_e} - k_d\,\dot{\phi} \tag{5.44}$$

to

$$\phi \;=\; \phi_{eq} + k_p\,\vec{\tau_e} \tag{5.45}$$

This sets the desired swivel angle to the estimated value from equation 5.24, but allows deviation from this estimate if the torque on the swivel axis is not zero with a stiffness of k_p. If the estimation does a reasonable job of predicting the desired swivel angle of the user, the swivel axis should rotate with the user without them having to apply a torque on that axis. The proposed modification to the admittance control will be compared with the purely reactive, non modified admittance control algorithm from section 4.1.1.

5.4.3 Experimental Setup

The exoskeleton's height was adjusted for all subjects in a seated position. The subject was secured in the device with the two straps, one at the upper arm and the other at the lower arm. In front of the subject was a table with 3 target plates. The targets were numbered 1 to 3 from the subjects right to left. The location of the targets were defined in Fig.5.8. Note that z points up and is measured from the floor. Each subject was instructed to touch the targets in the following order.

$$RP \rightarrow T1 \rightarrow RP \rightarrow T2 \rightarrow RP \rightarrow T3 \rightarrow RP(20times) \tag{5.46}$$

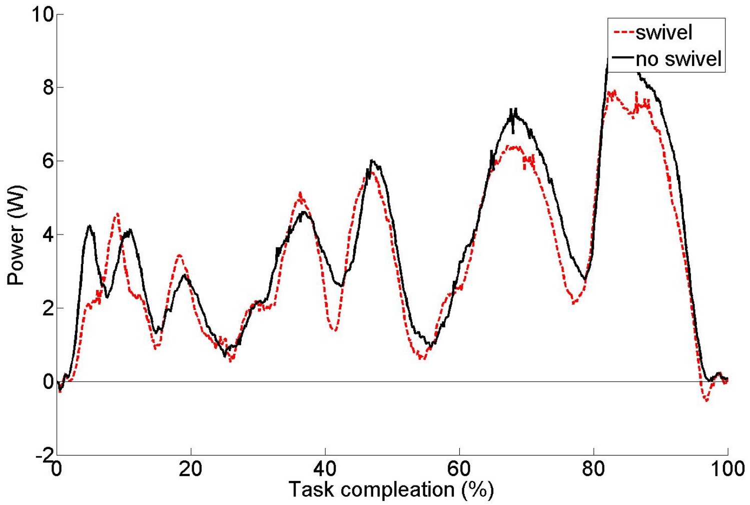

Figure 5.7: The interaction power of the exoskeleton and the user.

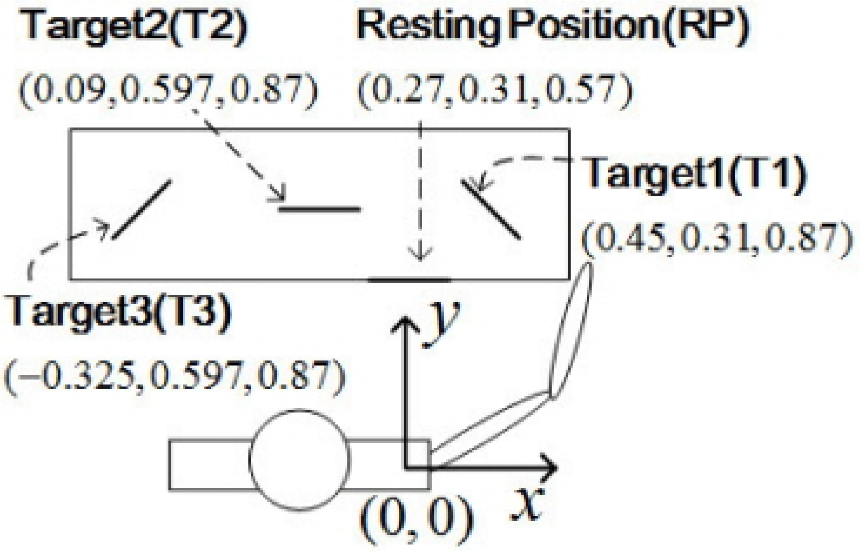

Figure 5.8: Target location for the admittance control algorithm test with respect to the Exo position. All measurement are in meters

5.4.4 Result

Four male subjects participated in this experiment. The average power profile for all subjects is represented in figure 5.7. The power peaks correspond to pushing the exoskeleton towards or pulling it back from the targets and the valleys occur when the subjects approached the target and their velocity reduced. The approach and retraction from each target is clearly distinguishable in the plot and it can be seen that the further away the target location, the greater the interaction power. This is reasonable to expects as the further the target position is, the more time the arm has to accelerate. In the plot, it can also be seen that while the power profile for control with and without swivel support are similar, the peaks and valleys are a little lower when swivel support is on.

The interaction energy averaged over all subjects showed a statistically significant difference (at the .05 level) when comparing the energy of swivel supported admittance control to non-swivel supported admittance control. The task interaction energy was 42.07 J with swivel support and 46.79 J without swivel support. This represents an 11.22% increase in the positive energy interaction when swivel support is not used. It is important to note that the interaction energy is the energy exchange between the robot and user and contains no information about the total energy of either system to complete the task. There were no statistaclly significant differences in the completion time when swivel support was added.

5.5 Discussion

The swivel estimation algorithm presented in this chapter is based on the hypothesis that the arm is optimizing its configuration to bring food back to the mouth. By choosing the redundancy of the arm such that the projection of the manipulability ellipsoid is maximized onto the line going from the hand to the mouth, a mathematical representation was formed to predict the swivel angle given the current hand position.

This algorithm is closed form, simple to implement, and fast to calculate which makes it ideal for real time control. Using motion capture, the prediction algorithm was tested for free space reaching tasks and shows less then five degrees of error from the predicted to the actual swivel angel selection. Next, the algorithm was applied to the exoskeleton controller by modifying the admittance control from section 4.1.1. When compared to non-swivel supported control, the admittance control without swivel prediction required 11.22% more interaction energy then the admittance with swivel support. These results produce a high level of confidence that the algorithm works to predice the arm configuration for reaching in free space and provides a way to increase the usability of the exoskeleton device for heathy subjects by reducing the interaction energy required to move the device. An even better potential use of this algorithm will be for use with a disabled population, where the exoskeleton is used for training. Recreating natural motion is important for this population and with this algorithm, the trajectory of the hand can be specified based on the task to be completed, without having to then also figure out what the configuration of the rest of the arm should be, it would automaticly be supported by the device that was running the swivel prediction algorthm.

Chapter 6

EMG CONTROL

EMG motion prediction and an admittance controller are used to determine the desired joint positions of the exoskeleton. Decoupled exoskeleton position data, force reading from the HMI, and myosignals from the user are the inputs to the motion controllers. The desired joint positions are then fed to a PID joint controller that, with the addition of friction and gravity compensation, calculates the desired joint torques. The joint torques are then fed to the torque decoupler to determine torque to the actuators [fig. 6.1]. The EMG motion prediction can calculate the desired motion of the user by measuring and analyzing the myosignals from a subset of the user's muscle. This controller, however, is feed-forward and doesn't correct for errors in the prediction. The admittance controller, which reacts to forces applied by the user on the HMI, is used to close the loop. Using the four force sensors, the exoskeleton robot tries to regulate the force to zero by moving the device in the direction of the force. This control design is explored in [58].

6.1 Methods

EMG motion prediction and an admittance controller are used to determine the desired joint positions of the exoskeleton. Decoupled exoskeleton position data, force reading from the HMI, and myosignals from the user are the inputs to the motion controllers. The desired joint positions are then fed to a PID joint controller that, with the addition of friction and gravity compensation, calculates the desired joint torques. The joint torques are then fed to the torque decoupler to determine torque to the actuators [fig. 6.1]. The EMG motion prediction can calculate the desired motion

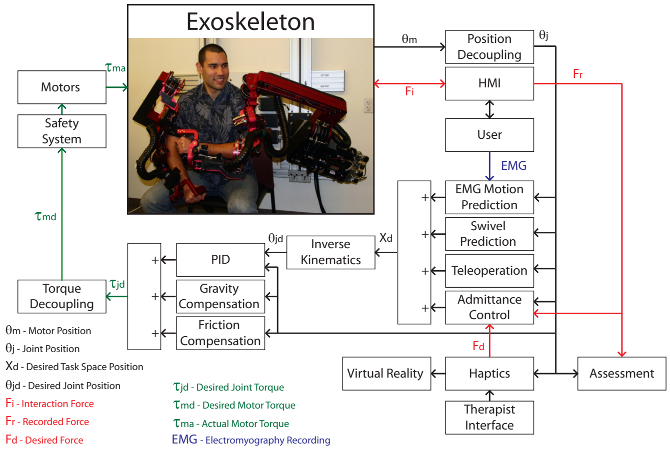

Figure 6.1: The position of the exoskeleton is determined by combination of the EMG motion prediction and admittance control. The EMG predicts motion based off of EMG from the user and the admittance control closed the loop using the force sensors at the HMI.

of the user by measuring and analyzing the myosignals from a subset of the user's muscle. This controller, however, is feed-forward and doesn't correct for errors in the prediction. The admittance controller, which reacts to forces applied by the user on the HMI, is used to close the loop. Using the four force sensors, the exoskeleton robot tries to regulate the force to zero by moving the device in the direction of the force. This control design is explored in [58].

Electromyography (EMG) is a technique for recording the electrical activity in the muscles when they are neurologically activated. There is an inherent delay from when a nerve first activates a muscle and when the muscle begins to contract. This delay is called the electro-mechanical delay (EMD). When EMG signals are used as one of the inputs to a motion control system, motion of the joints can be predicted before movement occurs. The EMG signal by itself does not give the necessary information to predict the motion of the joints. This signal only relates to the force generated by the muscle for isometric contraction. For dynamic motion, the muscle length and velocity are also necessary to estimate the resulting muscle force. Additionally, the moment arm that the muscle acts on changes as a function of the arm configuration. For all these reasons a muscle model is needed to predict the torque on a joint as a function of joint angles, velocities and the myosignals. This model consists of four modules:

1. **Neural activation module** - Takes raw EMG signals and processes them into muscle activations.
2. **Kinematic module** - Takes joint positions and anatomical data to calculate muscle lengths and moment arms.
3. **Hill base muscle model** - Takes muscle activations and lengths to predicts muscle forces.
4. **Dynamic module** - Takes muscle moment arms and forces to predict joint motion.

6.1.1 Neural activation module

Inputs: raw EMG signal
Outputs: muscle activation (a)

The neural activation module takes a raw EMG recording and processes it to produce the muscle activation (a). The EMG is recoded by placing electrode pairs on the skin and reading the differential voltage between them produced by the chemical process involved when a nerve activates a muscle contraction. Due to the nature of the signal it must be processed to infer meaning full data from it. The processed signal is called the muscle activation which is a value between 0 and 1, where 0 indicates no contraction and a 1 represents the highest voluntary contraction that muscle can produce. The following sections describe the particular hardware I will use to record the signals, the method for placing the electrodes to insure a good reading, the nature of the signal and why it is necessary to process, and finally the signal processing method.

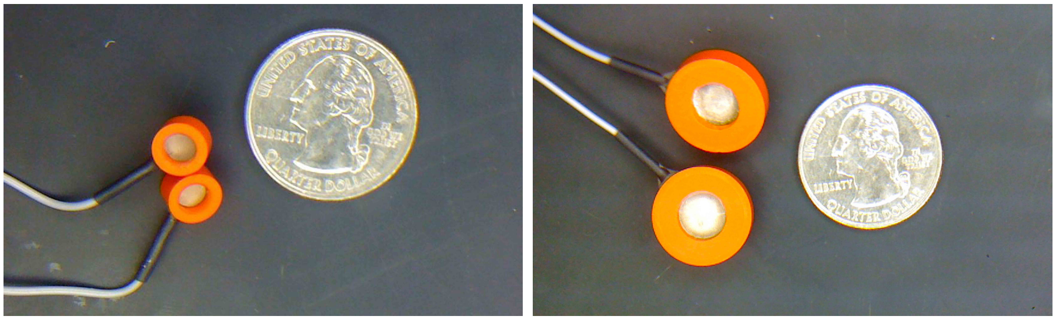

(a) E220N-LS (b) E224A-LS

Figure 6.2: Different sized electrodes from In Vivo Metric are used depending on the muscle being recorded

Hardware

For these experiments we will be using differential Ag-AgCl electrodes from In Vivo Metric (http://www.invivometric.com). We have two sizes, the E220N-LS has a 4mm sensor with a 7mm housing that is 5.5mm high [Fig. 6.2(a)] and the E224A-LS has an 8mm sensor with a 16mm housing and is 6mm high [Fig. 6.2(b)]. The smaller E220N-LS are for smaller muscles such as those of the forearm and the larger E224A-LS are for larger muscles such as the muscles of the upper arm.

The Electrodes attach to a custom 32 channel differential amplifier that consisted of 8 - 4 channel Teledyne A0401 modules that have a 1K gain, common mode rejection ratio of 100db, a first order high pass filter of 0.5 Hz and a 6th order anti aliasing low pass filter with cut off of 500Hz. Time constant of these filters are negligible compared to the constants of the filters used in the software that are on the order of 80 ms. A 14 bit analog to digital (A/D) card (model: PD2-MF-64-400/14H from UEI) reads values to the computer at 400 kS/s.

Table 6.1: Recommendations for electrode-skin preparation [44]

Impedance Range (kΩ)	Recommendation
1 - 5	Very Good
5 - 10	Good and recommended when feasible
10 - 30	Acceptable for easy conditions
30 - 50	Less good, attention is needed
$>$ 50	Should be avoided

Placing the electrodes

When placing electrodes to record EMG signals it is very important that the skin and electrodes are prepared properly before attachment and that the connection is tested after attachment. If the impedance of the skin is too high the signal will be weak or undetectable. To reduce the impedance of the skin at the electrode site, the hair and dead skin should be removed. Then the area should be cleaned with alcohol and allowed to dry before the electrode is placed on the skin. After the skin is ready, the electrodes need to be prepared. Each electrode is attached to the skin with a double-sided adhesive disk, and a conducting gel is used between the sensor and the skin. It is important that there aren't any bubbles in the gel as they will increase the impedance to the sensor. After placing the electrode pairs it is important to test the impedance between the pairs. The impedance between the electrode pair should be less then 10kΩ when the skin is prepared properly [44].

Action Potential

An ionic equilibrium between the inner and outer spaces of the muscle cell forms a resting potential at the muscle membrane. (Approximately -80 to -90 mV when not contracted). This difference in potential, maintained by an ionic pump, results in a negative potential compared to the surface. When a nerve activates a muscle fiber an influx of Na+ ions flows in causing depolarization. This is immediately restored by a backward exchange of ions within the ion pump. If a certain threshold is reach an action potential will occur causing a quick change from -80 to +30 milivolts. Starting from the motor end of the nerve the action potential propagates in both directions inside the muscle fiber. This excitation leads to a release of calcium ions in the intra cellular space creating a chemical process that eventually causes the muscle to contract [44]. The time from the action potential to the contraction is the neural muscular delay. This delay although dependent on many factors is roughly between 30-100ms [6, 63].

The action potential covers a ares of about $1-3mm^2$ and travels down the muscle fiber at about 2-6m/s. The potential difference between two electrodes placed on a muscle changes as the action potential propagates down the muscle fiber and depends on the distance between the electrodes. Because there are many muscle fibers all contracting to produce tension in a muscle, the signal that we see at the electrode is the superposed signal of all the units that are under the electrode site. Additionally the skin and contractile tissue have a low pass filter effect on the signal, resulting in a signal at the electrode site that is not exactly representative of the original signal [44]. Figure 6.3 shows a typical recording of an raw EMG signal.

Signal Processing

Because the EMG signal is an aggregate reading of all the muscle fibers under the electrode site, no two signals will be exactly alike. Therefore, only the qualitative shape of the signal is meaningful to us. The signal is filtered to extract out the meaningful portion of the signal. The EMG signal is sent through a cascade of filters as follows: 1) 20Hz High pass filter 2) 60Hz notch filter 3) full wave recertification 4) 5Hz low pass filter 5) Normalization to maximal voluntary contraction 6) nonlinear gain $a(t) = \frac{A^{u(t)}-1}{A-1}$. Figure 6.4 shows a signal as it goes through the filter process.

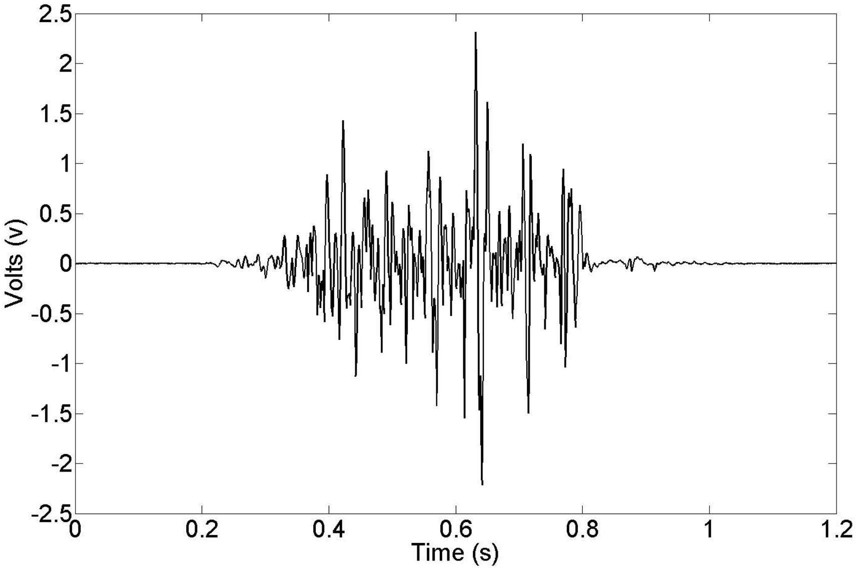

Figure 6.3: A typical non processes EMG recording. This signal was taken from the left bicep

6.1.2 Kinematic module

Inputs:	joint angles (θ)
Outputs:	muscle length (L)
	moment arm (b)

The kinematic module takes the arm's joint angles as an input and returns the muscle length as well as the moment arm for each joint that the muscle acts on. By specifying a series of stationary points that the muscle passes through as well as physical obstacles that are fixed relative to the bone, the line of action of the muscle is computed. The length of the line of action is equal to the muscle length. The moment arm is computed by looking at the direction the line of action attaches to the bone relative to the joint rotation axis. In the following sections the muscle length and moment arm calculations are explored in more detail.

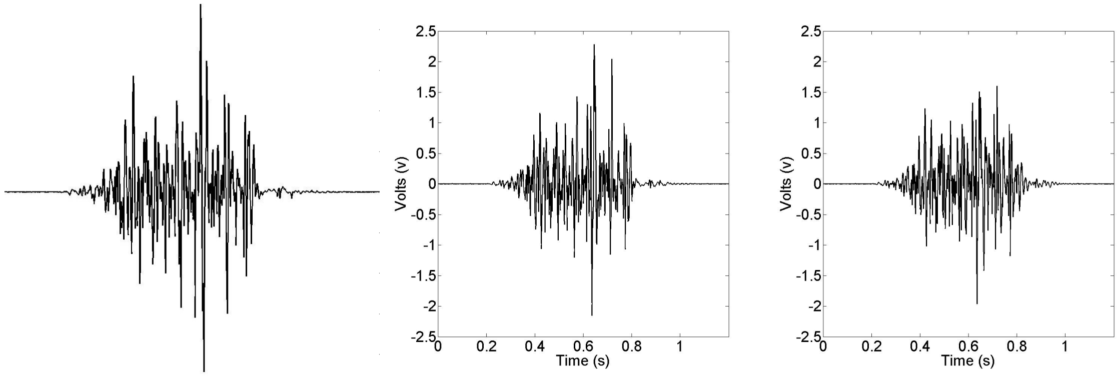

(a) Unprocessed (b) 20Hz highpass filter (c) 60Hz notch filter

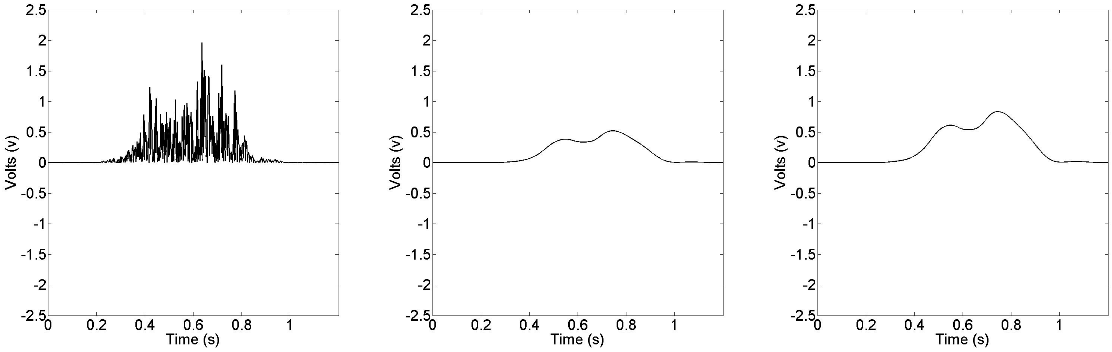

(d) Full wave rectification (e) 5Hz low pass filter (f) Normalization

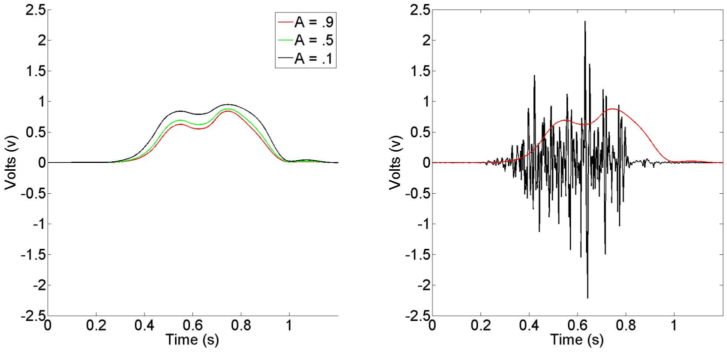

(g) Nonlinear gain (h) Original vs Processed

Figure 6.4: The recorded EMG signal goes through several filters to get a final processed signal. The unprocessed signal in (a) passes through the filters shown in **(b) - (g)**. In **(g)** three different values for the parameter A are chosen in order to show how that parameter affects the final value. In **(h)** the original signal and final processed signal with A = .5 is compared

Muscle length

In a series of papers by Garner and Pandy [17, 18, 19] a method is developed to determine the muscle length given the configuration of the arm. Their development begins by creating a kinematic model of the upper limb [17] based off of data from the visible human project (VHP). The VHP data set consists of high resolution medical images of the human body. They next develop a method for computing a muscle's length by defining the origin and insertion point of the muscle, several intermediate points called via points and one or more obstacles which represented other muscles or bones that the muscle could come in to contact with [18]. They define four obstacle types 1) a sphere, 2) a cylinder 3) a double cylinder and 4) a sphere caped cylinder. Their algorithm computes the distance between the defined points and adds the lengths to get a final length of the muscle. In the final paper of the series [19], the actual values for the origin and insertions points, the intermediate via points, and obstacle type and location are reported for several muscles of the upper limb.

Moment arm

After computing the muscle path, the moment arm can be readily computed:

$$b_i = (r_i \times F) \cdot k_i \tag{6.1}$$

where b_i is the moment arm for the i^{th} joint rotation, k_i is the direction of the of the joint rotation axis, F is the unitary vector along the force direction and r_i is the distance vector from the rotation axis to the insertion point.

6.1.3 Hill based muscle model

Inputs:	muscle length (L)
	muscle activation (a)
Outputs:	muscle force (F)

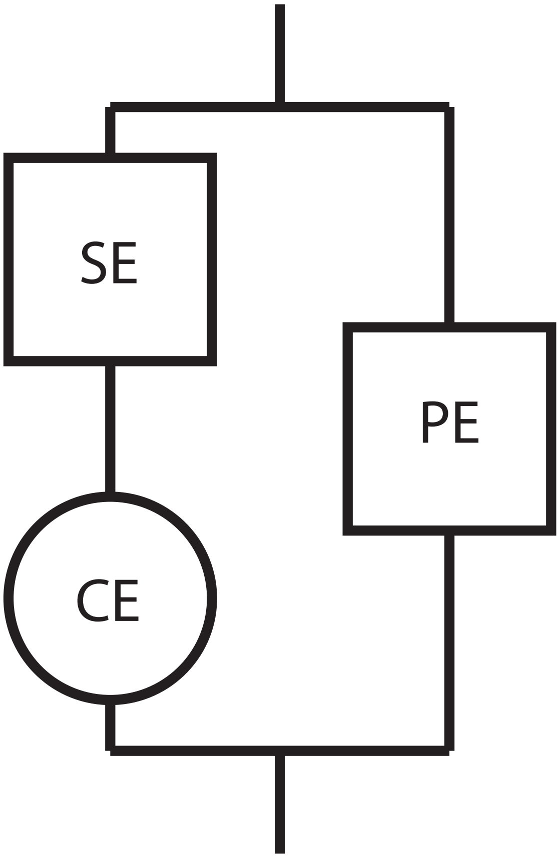

Figure 6.5: The Hill muscle model is a lumped parameter model. It consists of two branches. The first branch has an active contractile element and a passive serial element. The second branch has a passive parallel element.

The Hill based muscle model takes muscle length and activation as inputs and returns the muscle force. It is a systems engineering lumped parameter model used to predict muscle states first proposed by A.V Hill in 1938 [27] the model has been refined over the years by many others [84, 69, 85]. Because the model is based on experimental curve fitting and represents biological systems, a parameter optimization has to be preformed for each muscle force being predicted.

Model

The Hill based model consists of two parallel branches: one branch has an active contractile element (CE) and a passive serial element (SE), and the second branch has a passive parallel element (PE) [Fig. 6.5]. From the structure of the model we can relate the lengths and forces on each element in the following ways:

$$\begin{aligned} L_{PE} &= L_{CE} + L_{SE} && (6.2) \\ F_{SE} &= F_{CE} && (6.3) \\ F_{tot} &= F_{CE} + F_{PE} = F_{SE} + F_{PE} && (6.4) \end{aligned}$$

Where L is the length and F is the force on the elements.

The passive parallel and serial elements represent connective tissue, tendons, skin, blood vessels and other tissue that do not actively create tension. They generate force based on displacement and have the same equation with differing internal parameters.

$$F_{PE,SE} = \left[\frac{F_{max}}{e^{S} - 1}\right]\left[e^{(S\Delta L/\Delta L_{max})} - 1\right] \tag{6.5}$$

where $F_{PE,CE}$ is the passive force generated by either the PE or SE element. ΔL is the change in length compared to the slack length of the element. S is a shape parameter and determines the stiffness of the element. F_{max} is the maximum force exerted when the element is at its maximum length of ΔL_{max}

The force generated by the CE element is a function of the neural activation a, the normalized force-length function f_l, the normalized force-velocity function fv, and the constant value $F_{CE_{max}}$ which is the maximum force the element can produce. The following are the experimentally determined functions that describe the force created by the CE element:

$$\begin{aligned} F_{CE} &= a \cdot f_l \cdot f_v \cdot F_{CE_{max}} && (6.6) \\ f_l &= \exp\left[-.5\left(\frac{\frac{\Delta L_{CE}}{L_{CE_0}} - \phi_m}{\phi_v}\right)^2\right] && (6.7) \\ f_v &= \frac{0.1433}{0.1074 + \exp[-1.3\sinh(2.8\frac{V_{CE}}{V_{CE_0}} + 1.64)]} && (6.8) \\ V_{CE_0} &= 0.5(a+1)V_{CE_{max}} && (6.9) \end{aligned}$$

f_l is modeled as a Gaussian function where ΔL_{ce} is the length change of the CE element and L_{CE_0} is the optimal fiber length. ϕ_m and ϕ_v affect the mean and variance of the distribution. In the force-velocity equation, V_{CE} is the velocity of the CE element and V_{CE_0} is the maximum velocity of the the element when $F_{CE} = 0$. It is possible to express V_{CE_0} as a function of the neural activation and $V_{CE_{max}}$.

Using the neural activation from section 6.1.1 and the muscle length found in section 6.1.2 the muscle force can be computed. The force generated by the PE element can be immediately found given the muscle length using equation (6.5). To find the force of the CE or SE element, the length of the element must first be solved. By turning equation (6.6) into a nonlinear finite difference equation, it becomes a function of L_{CE} only.

$$F_{CE}(\Delta L_{CE}[n]) = \frac{0.1433 * a * f_l(\Delta L_{CE}[n]) * F_{CE_{max}}}{0.1074 + \exp\left[-1.3\sinh\left(2.8\frac{\Delta L_{CE}[n] - \Delta L_{CE}[n-1]}{\Delta t * V_{CE_0}} + 1.64\right)\right]} \quad (6.10)$$

Furthermore, F_{SE} can also be expressed as a function of L_{CE} replacing L_{SE} with $L_{PE} - L_{CE}$. Next set F_{SE} equal to F_{CE} and solving for L_{CE}. This can be accomplished with root finding algorithm such as the bisection algorithm. Because we know the total length of the muscle we can guarantee a desired precision in a known finite number of iterations. The total force generated by the muscle is then $F_{CE} + F_{PE}$.

6.1.4 Dynamic module

Inputs:	moment arms (b)
	muscle force (F)
Outputs:	joint torque (τ)
	joint position (θ)

The dynamic module uses the moment arm and muscle force to predict the joint torque and position. The torque predicted by the model on each joint will be equal to

$$\tau_i = \sum_j F_j * b_{ij} \tag{6.11}$$

Where τ_i is the torque on the i^{th} joint rotation, F_j is force generated by the j^{th} muscle, and b_{ij} is the moment arm for the j^{th} muscle acting on the i^{th} joint. The desired joint position will the be calculated using a PID admittance controller:

$$\theta_i = k_p \tau_i + k_i \int \tau_i + k_d \dot{\theta} \tag{6.12}$$

6.2 Experiment

4 subjects performed a reaching task with the exoskeleton to evaluate the performance of the motion prediction of the EMG controller. The following section describes the muscles selected for the motion prediction, the parameter optimization, the experimental procedure, and performance metrics.

6.2.1 muscle selection

For this set of experiments, EMG motion prediction of the shoulder and elbow were targeted. To reduce complexity, wrist motion was controlled with admittance control only. The large muscle groups responsible for shoulder and elbow motions that could also be easily recorded using surface electrodes were chosen for the EMG inputs of

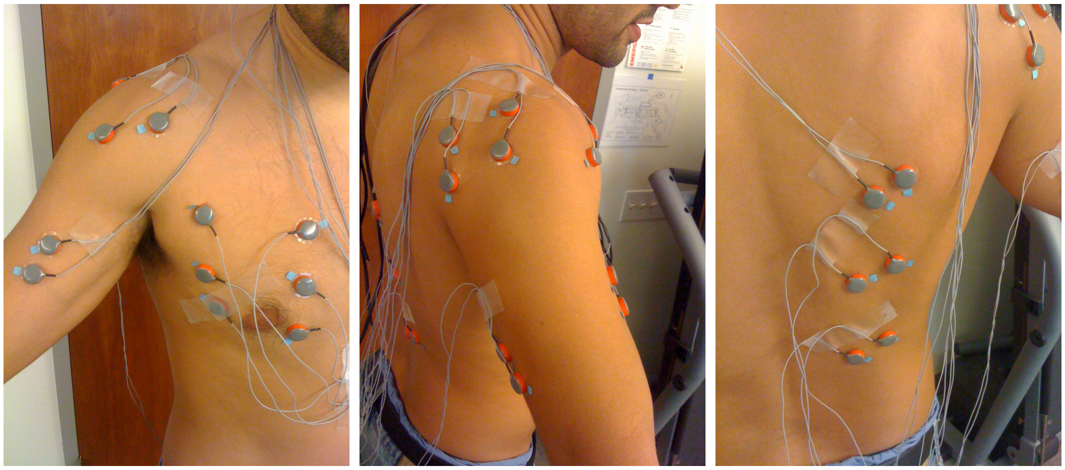
(a) (b) (c)

Figure 6.6: A front **(a)** side **(b)** and rear **(c)** view of a Subject with a set of 11 electrodes attached.

the controller. Initially, eleven muscle groups were selected. These included the 1) Biceps, 2) Triceps, 3) Pectoralis Ribs, 4) Pectoralis Sternal, 5) Pectoralis Clavicular, 6) Deltoid Clavicular, 7) Deltoid Acrimial, 8) Deltoid Scapular, 9) Latissimus Dorsi Thoracic, 10) Latissimus Dorsi Lumbar, and the 11) Latissimus Dorsi Illiac. Figure 6.6 shows the attached electrodes. After some preliminary testing, it was found that the signals recorded from the Pectoralis Ribs, Latissimus Dorsi Thoracic, Latissimus Dorsi Lumbar, and the Latissimus Dorsi Illiac had a very low signal to noise ratio despite the fact that they were large easy to record muscle groups. After some investigation it was determined that for the motions in the experiment, these muscle groups caused motion of the arm in the same direction as gravity, and therefore had low activation. For this reason they were ultimately not included in the final control design for shoulder and elbow motion prediction.

In the previous publications [17] [19] frame assignments for the skeleton, muscle origin and insertion location were given. The exoskeleton device has a different frame assignment and link lengths then the model presented in those works. For this reason, the model had to be modified slightly to work with the exoskeleton device. First the origin and insertion points were converted to the exoskeleton frame. Next the locations were modified due to slightly different link length of the garner model and the exoskeleton. To accommodate the differences, the location of the insertions were moved so that on the exoskeleton they were the same distance to the nearest joint as in the garner model.

6.2.2 Parameter Training

Due to physological differences between subjects, the parameter set in the muscle model that was presented in section 6.1.3 must be tuned for each individual. Due to the large parameter space and the high degree of non-linearity in the model, a genetic algorithm is well suited for the parameter training. The muscle model presented in section 6.1.3 has 14 parameters per muscle. The parameters in the model have physical meaning at the expense of a model that is mathematically redundant. By combining parameters, the model can be reduced to have only nine parameters. Because we are fitting the parameters with experimental data using the genetic algorithm, distinction between the redundant parameter is not possible. Additionally, reduction of the parameter space increases the likelihood of convergence. Parameters are combined in equations (6.7) and (6.5) for f_l and $F_{SE,PE}$ in the following way:

$$f_l = C_1 \exp\left[-0.5\left(\frac{L_{CE} - C_3}{C_2}\right)^2\right] \tag{6.13}$$

$$F_{SE,PE} = A_1\left[\exp(A_2(L_{SE,PE} - A_3) - 1)\right] \tag{6.14}$$

The rest of the parameters remain unchanged.

Using a 10 step process the parameter were tuned for each individual preforming the experiment.

1. Record training data with the exoskeleton device. The subject was asked to

move the device around and touch some targets. The admittance joint control was active during this time. Three recordings were taken for each subject. EMG signals, joint positions, and applied joint torques (calculated using the force sensors), were recorded for the training set.

2. Run a simulation, using Matlab's Simulink, of the muscle model, which took an initial set of parameters, the joint positions, and EMG data recorded from the training set as inputs to calculate the estimated joint torque from the muscle model.

3. A cost function was calculated to determine how well the estimation fit the data in the following way:

$$\sum_{j=1}^{4} W_j * (\tau_{estimate_j} - \tau_{measured_j})^2$$

   Where j is the joint, W_j is a weighing factor for joint j and $(\tau_{estimate_j} - \tau_{measured_j})$ is the difference between the actual and measured joint torque.

4. Update each parameter using the following equation:

$$P_{update} = P_{current} + (rand - .5) * Span$$

   Where P_{update} is the updated parameter set, $P_{current}$ is the current parameter set, $(rand - .5)$ is a random number between -.5 and .5, and $Span$ is a scaling factor to make the update an appropriate size for each parameter.

5. Apply a saturation to the P_{update} set to ensure that parameters that must be positive will be set to a small non zero positive number if the update from the previous step results in a negative value.

6. Ensure that the updated parameter set is valid. The force produced by the contractile element is equal to the series element and their combined length must be equal to the parallel element. Figure 6.7(a) shows a typical force-length curve for the contractile and series elements in the model. The intersection of the two curves determines the force produced by the contractile element. A parameter set is valid if the solution is continuous for an action potential of the muscle in the set [0,1] and the muscle's length is between its minimum and maximum. The solution set is continuous if there is only one intersection point of the two curves. Figure 6.7(b) show an example of an invalid parameter set because F_{SE} has multiple intersection points with F_{CE}.

   We want to ensure that there is always only one intersection point for a given muscle length, By solving for the length in term of the force of equation (6.13) and (6.14) and comparing the slopes of the two curves, we can determine if the parameter set is valid.

$$L_{CE} = \pm\sqrt{2C_2^2 \ln\left(\frac{C_1}{F_{CE}}\right)} + C_3 \tag{6.15}$$

$$\frac{\delta L_{CE}}{\delta F_{CE}} = \frac{-C_2}{\sqrt{2\ln\left(\frac{C_1}{F_{CE}}\right)}F_{CE}} \tag{6.16}$$

$$\frac{\delta^2 L_{CE}}{\delta F_{CE}^2} = \frac{C_2(2\ln(\frac{C_1}{F_{CE}}) - 1)}{\sqrt{8}\ln^{\frac{3}{2}}\left(\frac{C_1}{F_{CE}}\right)F_{CE}^2} \tag{6.17}$$

$$L_{SE} = \frac{-\ln(\frac{F_{SE}}{A_1} + 1)}{A_2} + A_3 \tag{6.18}$$

$$\frac{\delta L_{SE}}{\delta F_{SE}} = \frac{-1}{A_1 A_2 + A_2 F_{SE}} \tag{6.19}$$

$$\frac{\delta^2 L_{SE}}{\delta F_{SE}^2} = \frac{1}{A_2(A_1 + F_{SE})^2} \tag{6.20}$$

   If $L'_{CE} = L'_{SE}$ for some value of F (i.e. L'_{CE} and L'_{SE} intersect), then there exist a value of A_3 that gives multiple solutions on the force length curve and the parameter set is invalid. Because there is no closed form solution to $L'_{CE} - L'_{SE} = 0$ an iterative method was used to check the parameter set.

By looking at some special values and examining the properties of equations (6.15) - (6.20), the problem can be broken down into three cases. The values are, $L'_{SE}(0)$ when the slope of the length curve of the series element when the series element has no force (i.e. its slack length), $L'_{SE}(C1)$ the slope of the length curve for the series element when the force of the contractile is maximum, and $C_1 e^{-.5}$ the maximum slope of the length curve for the contractile element. The equation properties are L'_{SE} is strictly increasing and L''_{SE} is strictly decreasing for all values of F. L'_{CE} is strictly increasing and L''_{CE} is strictly decreasing in the range of F from $[0, C_1 e^{-.5})$. Then L'_{CE} is strictly decreasing and L''_{CE} is strictly decreasing in the range of F from $(C_1 e^{-.5}, C_1]$. From these properties it can be concluded that if

- $L'_{SE}(0) > C_1 e^{-.5}$ Then L'_{SE} will always be greater then L'_{CE} and the two curves will not intersect meaning the parameter set is valid.
- $L'_{SE}(C1) < C_1 e^{-.5}$ then L'_{SE} and L'_{CE} will intersect, which implies that there is some value of A_3 that creates an invalid parameter set.
- Otherwise, an iterative method is used to determine if the two curve intersect.

If $L'_{SE}(F_{n-1}) < C_1 e^{-.5}$ there exists a value F_n such that $L'_{CE}(F_n) = L'_{SE}(F_{n-1})$. Where n begins at 1 and $F_0 = 0$

$$F_n = \sqrt{\frac{-C_2^2}{L'^2_{SE}(F_{n-1}) W\left(\frac{-C_2^2}{L'^2_{SE}(F_{n-1}) C_1^2}\right)}}$$

Where $W(*)$ is the LambertW function. From the properties of equations (6.15)

- (6.20), it is guaranteed that F_n occurs before L'_{SE} and L'_{CE} intersect. Next update the value of F_n to F_{n+1} by finding the intersection of L'_{SE} and the line that is tangent to the curve L'_{CE} at the point F_n. This is done by solving the quadratic formula with $A = mA_1$, $B = A_1A_2m + bA_2$, and $C = bA_1A_2 + 1$, where $m = L''_{CE}(F_n)$ and $b = -mF_{n-1} + L'_{CE}(F_n)$ are the slope and intercept of the tangent line. If $L'_{SE}(F_{n+1}) > C_1e^{-.5}$ no intersection will occur and the parameter set is valid, if $L'_{SE}(F_{n+1}) = C_1e^{-.5}$ the intersection occurs here and the parameter set is invalid, Otherwise continue to update F_n until one of the two cases are satisfied. If the parameter set is invalid return to step 4, if it is valid go to the next step.

7. Run the same simulation as in step 2 with the updated parameter set.

8. Calculate the cost function for the new simulation and compare it to the previous cost function. If the cost with the new parameter set is less then the previous cost, update the parameter set, otherwise discard the new parameter set and keep the previous parameter set and cost.

9. Repeat steps 4 - 8 for 2000 iterations.

10. Using one of the sets of data that was not used for parameter tuning, run the simulation with the newly updated parameter. Verify that there is a good fit on the data that was not used to update the parameters. If the fit is not good, use a different set of data to train the parameters and compare the new set with data that was not trained on.

6.2.3 Procedure

The anatomical data were recored for each subject performing the experiment. This included height, age, gender, and dominant handedness. In order to allow electrodes

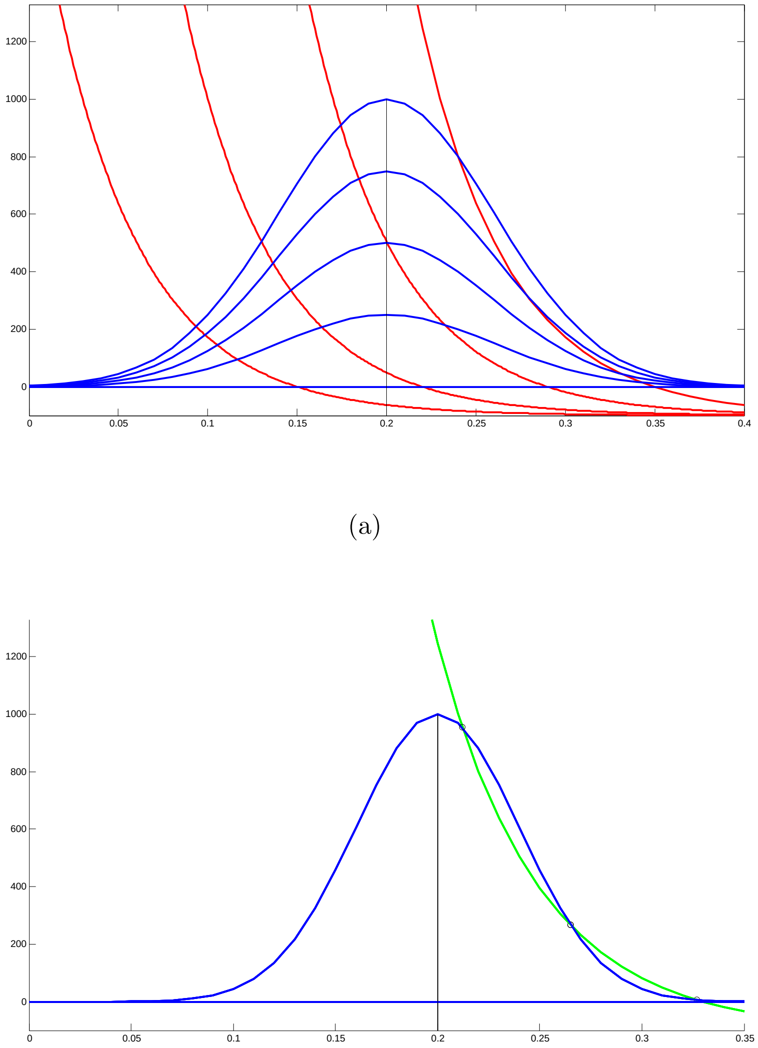

(a)

(b)

Figure 6.7: **a)** The possible force of the contractile element (blue line) is modeled as a family of Gaussian curves, where the particular curve is determined by the activation level and velocity of the muscle. The possible force of the series element (red line) is the family of exponential curves, where the particular curve is determined by the length of the parallel element. The force generated by the two elements for a particular instant of time is the value where the two curves intersect. **b)** For some parameter sets, the F_{ce} and F_{se} curves intersect in multiple locations. This results in a non continuous force prediction for the muscle and is an invalid parameter set.

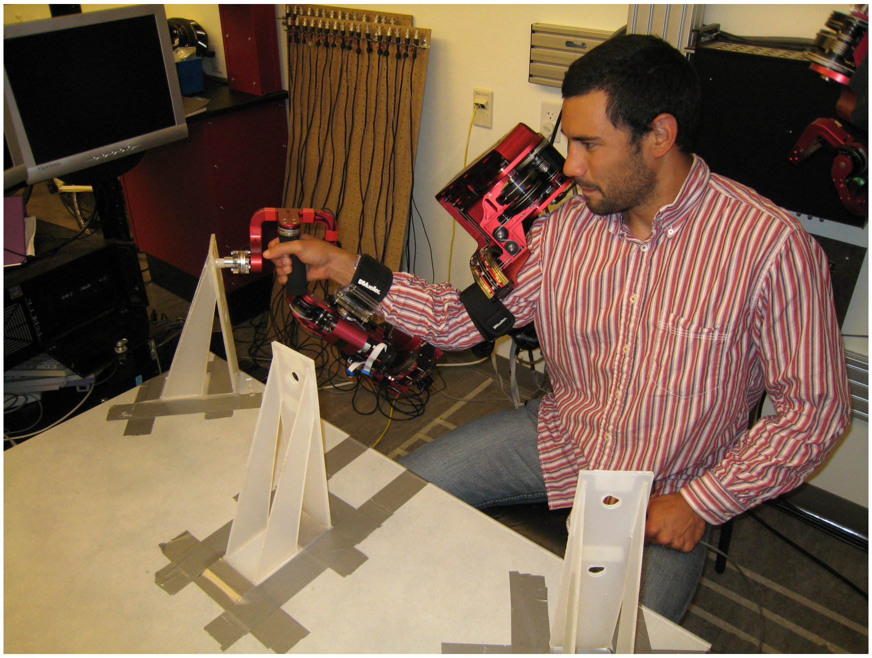

Figure 6.8: The subject would move from a start location to one of three randomly selected targets for each trial of the experiment.

access to the muscles, the subjects wore a sleeveless shirt. For each of the muscles being recorded the skin was conditions using an exfoliating pad then cleaned with alcohol. The alcohol was allowed to dry and the electrode pair was then attached to the muscle following the procedure descried in section 6.1.1. To ensure a good signal reading, the impedance between the electrode pair was measured. If the impedance was greater then $10k\Omega$ the electrode pair was removed, and the conditioning and placement of the electrode was repeated until a value less then $10k\Omega$ was achieved.

After all the electrode pairs were placed, the subject was seated and their right arm was secured in the right exoskeleton device. Their left arm rested in the left side device which helped to keep their torso aligned properly, but this arm was not used for these experiments and was not strapped into place. In front of the the subject was a table that had three targets and a start position attached to it, the start (S) position was under the table and to the users right, target 1 (T1) was to the subjects right, target 2 (T2) was directly in front of the subject and target 3 (T3) was located to the subjects left [fig. 6.8]. The target location with the X,Y measured from the center of shoulder rotation, and Z measured from the ground were, S [.223,.423,.612], T1 [.450,.431,.924], T2 [.09,.597,.924] and T3 [-.325,-.575,.924]. With X being to the subjects right, Y being in front of the subject and Z pointing up, all units are in meters. Before starting data recording, each subject was given as much time as they liked to move around in the exoskeleton. A foot pedal released the mechanical brakes and activated the motors. Admittance control only was run during the acclimation period. After the subject indicated that they felt comfortable moving around in the device, an initial data set was recorded for the purpose of data parameter fitting. The initial set consisted of the subject starting with the tip of the end effector touching the start position and the pedal in the disengaged position. Next the subject engaged the device by pressing and holing the foot pedal, and moved the tip of the exoskeleton to touch:

$$\text{S} \rightarrow \text{T1} \rightarrow \text{S} \rightarrow \text{T2} \rightarrow \text{S} \rightarrow \text{T3} \rightarrow \text{S}$$

After the above sequence was completed the subject then released the foot pedal. This sequence was repeated three times. The subject was unhooked from the device, but the electrode pair were left on while the data was used for parameter fitting.

After the parameters for the muscle model were fit for the subject, the subject was brought back to conduct the experiment. The impedance of each electrode pairs was again recorded to ensure that the impedance was still below 10 $k\Omega$. There were three reach movements:

$$S \rightarrow T1 \rightarrow S$$

$$S \rightarrow T2 \rightarrow S$$

$$S \rightarrow T3 \rightarrow S$$

and two controller configuration: admittance control only, admittance control plus EMG prediction, for a total of 6 different trial conditions. For each trial condition, the subject began at start, pressed and held the pedal, touch the designated target, returned home and released the pedal. One repetition consisted of a set of each of the six trials in a random order. Each subject was supposed to complete 25 repetitions. After the subject had completed all the repletions, the experiment was completed and they were unhooked from the device.

6.2.4 Metrics

The exoskeleton device collects EMG data, forces and torque interactions between the user and device, joint position data and the state of the enable pedal. For performance evaluation, the forces and torques applied to the device, the task completion time, the path length of the hand, interaction power and interaction energy are calculated. Forces and torques were read directly from the force sensors. Task completion time was defined as the time between when the enable pedal is pressed until it is released. path length was calculated by the integral of the absolute value of the velocity vector. The interaction power was calculated by taking the dot product of the linear velocity at each force sensor with the force reading at the respective sensor and adding that to the dot product of the angular velocity at each sensor with the torque of each respective sensor. The angular and linear velocity at each sensor was calculated by first finding the position of each sensor using the joint angle data and the forward kinematic map, then differentiating the position with respect to time. Positive power indicates that that the user is pulling the device in a direction, and negative power regions indicate that the user is being pulled by the device. Note that this calculation is the power exchanged between the system and the user and is not an indication of how much power the system or the user is using individually. Also note that the power exchange is non conservative and negative power regions do not create energy storage. The interaction energy is found by integrating the power, however, because the negative power is not stored as energy, the negative and positive energy should not cancel each other out. For this reason, the positive and negative portions of the energy are calculated separately. The metrics from the EMG and joint control were compared using Matlab's multcompare function. Statistical significance was set at the .05 level.

6.3 Results

Four male subjects between the ages of 21 and 32 performed the experiment. Subject 1 preformed 20 repetitions of the experiment, Subject 2 preformed 25 repetitions, subject 3 preformed 25 repetitions, and Subject 4 preformed 11 repetitions. After removing data that didn't record correctly there was usable data from 520 trials. The impedance of the electrode pairs for every test was less then the prescribed $10k\Omega$.

6.3.1 Force / Torque

Figures 6.10(a) and 6.10(b) shows the average force and torque that was applied to the exoskeleton device during a trial normalized with respect to task completion. Similar values for the force and torque were recorded with and without EMG assistance turned on.

6.3.2 Interaction Energy

The first two rows of Figure 6.9 show the recorded interaction energy for each trial of the experiment. Tables 6.2 and 6.3 show the average negative and positive interaction energy for each subject along with the 95% confidence interval for the true population mean, and whether the difference between joint control and EMG control is statistically significant. Subjects 1 and 2 showed a statistically significant difference in the negative energy interaction. Subjects 1 and 3 showed a statistically significant difference in the positive energy interaction. No other groups showed significant changes with respect to the energy exchange between the user and the device.

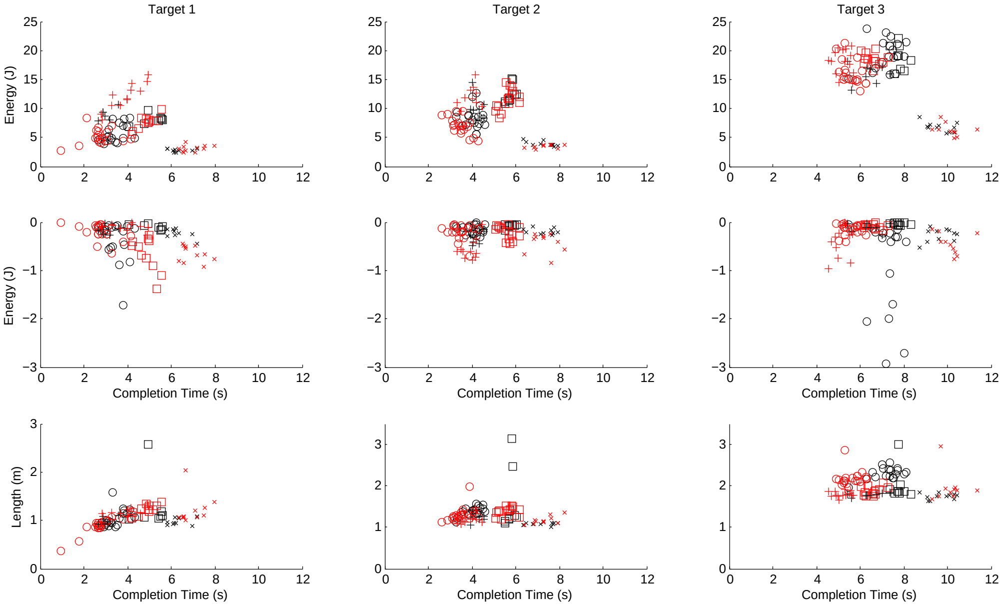

Figure 6.9: Positive and negative interaction energy and path length for each trial in the experiment. The three columns are for each target. The three rows are the positive portion of the interaction energy, the negative portion of the interaction energy and the path length of the hand. Subject 1 is represented with the o symbol, Subject 2 with the □, Subject 3 with the +, and Subject 4 with the x. The black marks are when control with EMG assist was used, and the red marks are for control without EMG assistance

Table 6.2: Average Negative Energy (J) Per Trial with 95% confidence interval

	Joint Space Control	EMG Control	Statistically Significant
Subject 1	-.4364 ± .0674	-.1776 ± .0674	Yes
Subject 2	-.0699 ± .0402	-.3212 ± .0322	Yes
Subject 3	-.1981 ± .1890	-.3376 ± .1384	No
Subject 4	-.2108 ± .1533	-.4833 ± .1533	No
Subject average	-.2774 ± .0605	-.3008 ± .0546	No

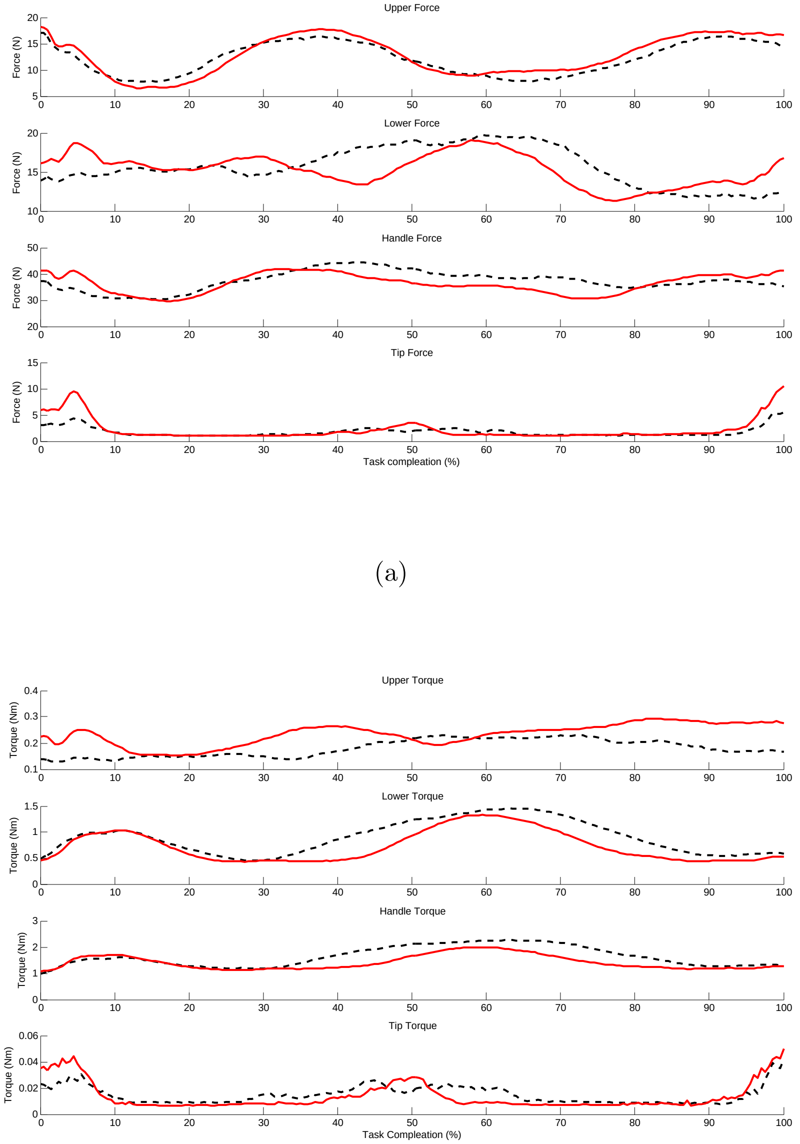

(a)

(b)

Figure 6.10: Average force **(a)** and torque **(b)** recorded at the upper arm, lower arm, handle and tip force sensors. The red line is when the EMG assist is on and the black line is when EMG assist is off.

Table 6.3: Average Positive Energy (J) Per Trial with 95% confidence interval

	Joint Space Control	EMG Control	Statistically Significant
Subject 1	10.8800 ± .3498	8.7714 ± .3498	Yes
Subject 2	13.0963 ± .2953	12.5374 ± .2367	No
Subject 3	11.8507 ± .5210	13.9307 ± .3814	Yes
Subject 4	4.2220 ± .3337	3.9977 ± .3337	No
Subject average	9.8197 ± .3468	9.8623 ± .3134	No

Table 6.4: Average Path Length Per Trial with 95% confidence interval

	Joint Space Control	EMG Control	Statistically Significant
Subject 1	1.573 ± 0.029	1.459 ± 0.029	no
Subject 2	1.625 ± 0.044	1.490 ± 0.035	no
Subject 3	1.350 ± 0.049	1.395 ± 0.036	no
Subject 4	1.270 ± 0.040	1.447 ± 0.040	yes
Subject average	1.454 ± 0.021	1.448 ± 0.018	no

6.3.3 Path Length

The last row of figure 6.9 shows the recorded path length of the hand for each trial of the experiment. Table 6.4 shows the average path length of each subject along with the 95% confidience interval for the true population mean, and whether the difference between joint control and EMG control is statistically significant. Subject 4 showed a statistically significat differnce, no other group shows a difference.

6.3.4 Completion Time

The plots in figure 6.9 are plotted verses completion time. Table 6.5 shows the average task completion time for each subject and the average of all subjects, along with the 95% confidence interval and statistical significance between joint space control and EMG control. Subjects 1, 2 and the average of all the subjets showed a statistically significant difference in the completion time.

Table 6.5: Average Completion Time (sec) Per Trial with 95% confidence interval

	Joint Space Control	EMG Control	Statistically Significant
Subject 1	4.7823 ± .1128	3.6529 ± .1128	Yes
Subject 2	6.2318 ± .0902	5.6811 ± .0723	Yes
Subject 3	4.5549 ± .1130	4.3342 ± .0827	No
Subject 4	7.1454 ± .4721	7.6043 ± .4721	No
Subject average	5.7477 ± .1432	5.2321 ± .1281	Yes

6.3.5 Interaction Power

Figure 6.11 shows the interaction power averaged over all trials after it had been normalized with respect to task completion. The interaction energy for both joint control and EMG control have similar qualitative shapes with the EMG control having a consistently higher interaction power.

6.4 Discussion

The interaction power plot [Fig. 6.11] shows that EMG control has a higher power requirement than joint space control to complete the same task. This is not surprising after noting that the interaction energy required for task completion was the same for both controllers but the completion time for EMG control was faster. Additionally the path length for the two controls showed no significant differences, the trajectories were not changed with the use of the EMG control. Figures 6.10(a) and 6.10(b) show that the forces and torques that were applied to the device for the arm motions were similar in magnitude for both controllers. In the ideal case it is desirable that that both the completion time and the interaction energy to preform the task would decrease with use of the EMG controller. However a faster completion time with the same force applied to the device means that the effective gain of the system increased when the EMG control was turned on.

Due to high variability between subjects it is also worth looking at individual

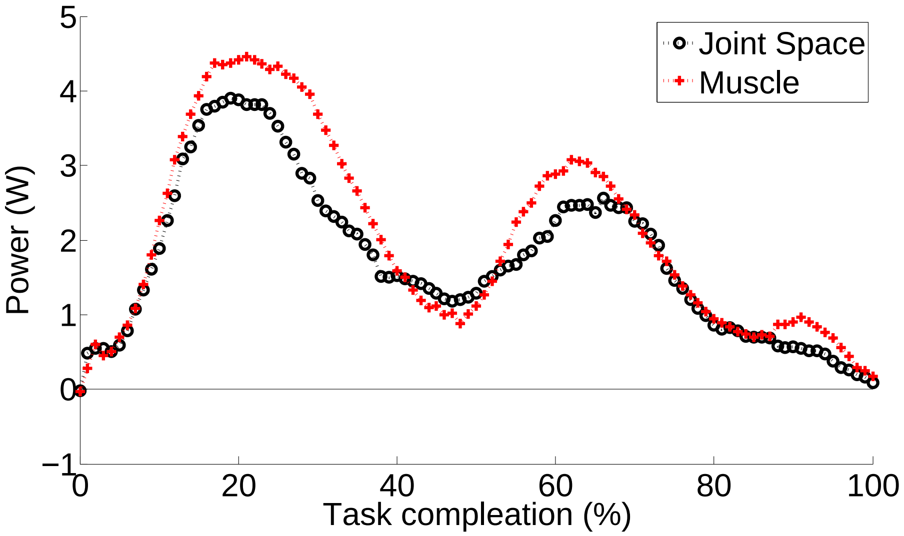

Figure 6.11: Interaction power averaged with respect to task completion. The qualitative shape of the two curves are similar but the EMG controller consistently had a higher interaction power.

performance of the tasks. Subject one showed the ideal case where both the interaction energy and the completion time of the task were reduced with use of the EMG control. Subject two showed a decrease in completion time but the same level of interaction energy with the EMG control, indicating some improvement over joint space control but not the ideal case as with subject one. Subject three showed no improvement in completion time and an increase in the interaction energy with EMG control. EMG control for subject three was worse then simple joint space control. Subject four saw no significant differences in either task completion time of force interaction. Of the four subjects two saw improvements; one had a decrease in performance and one saw no difference between the controllers. Each subject had an individual parameter fit performed for their experiments because a genetic algorithm was used there is no guarantee that a minimum was found for the subject data and it is likely that it was not. The large parameter space makes it hard to conclude how far from optimum performance the controller was working for an individual, but the improvements in individual performance shows that it is possible to predict motion using the prescribed method.

6.5 Conclusions

The EMG control method that was used for this study showed some promise in its ability to predict motion. Due to the large parameter space, and the uncertainty of the genetic algorithm or other method available to fit large nonlinear parameter sets, it is difficult to always fit the parameter set of an individual such that motion prediction is accurate. Additionally, although not measured as a metric, the set up time to place all the electrodes is long. For these reasons this method is probably not suitable for use in a disabled population, who would have difficulty tolerating long sessions to place electrodes, and lack the strength to overcome incorrect motion of the device if the parameter fit was initially done poorly. Future work should be focused on reducing setup time, improving methods for individual parameter fitting, and extending the method to include muscles of the forearm.

Chapter 7

CONCLUSIONS

Integrating capabilities of humans and robotic-machines into a unified system offers numerous opportunities for developing a new generation of assistive technology. Potential applications could benefit members of both healthy and disabled populations. At the heart of this human-machine integration lies two fundamental scientific and technological issues: (i) the exoskeleton (orthotic device) mechanism itself and its biomechanical integration with the human body, and (ii) the human machine interface (HMI). These two key issues will determine the quality of the integration between the human and the exoskeleton in terms of how natural it will be for the operator to control the exoskeleton device as a biological extension of his/her body. This body of work focused on the HMI at the controls level and explored three modes of operation, admittance control, swivel angle prediction, and EMG control.

Admittance Control: The admittance controller takes user inputs in the form of force readings at the physical interface between the user and the device as well as the environment. From the force inputs, a position command is created, the command can be used for arm tracking where the force is driven to zero when the device follows the user, or the force can be driven to non-zero to simulate integrations with a virtual environment. Due to the redundancy and multiple contact points with the user, a single force sensor is insufficient to determine the intended arm configuration of the user. There are four sensor locations, one at the upper arm, one at the lower arm, one in the handle and one at the end effector tip. Each of the 4 sensors has 6 degrees of freedom (3 force and 3 torque reading) for a total of 24 signals. The exoskeleton has 7 degrees of freedom, so a mapping from the 24 dimensional sensor space onto the 7 dimensional robot joint space had to be achieved. Two methods were explored, a task space model, where the forces were combined in task space then used the inverse kinematic map to solve the joint space configuration, and the joint space model where the forces were resolved first into joint torques then combined to solve for the joint space configuration.

Comparing the interaction power, energy and the task completion time, showed that the task space model performed better than the joint space model. Both controllers reduced the interaction forces required for the device to track the motion of the user. However, the completion time was reduce compared to manually back driving the device. The reduced controller bandwidth compared to the simple back-driven mode is caused by limitations on the gains of the system. This is most likely due to subject-device misalignment, signal noise and system compliance.

Swivel Angle Prediction: Swivel angle prediction is an algorithm to predict the configuration of the redundant space of the exoskeleton based on the position of the end effector. From observation of human behavior it is noted that one of the most important roles of the human arm is to bring food to the mouth. The hypothesis that the redundant space is configured to always optimally be able to bring whatever is in the hand to the mouth was proposed. This configuration corresponds to the plane defined by the three points located at the shoulder, elbow and wrist joints being coplanar with the plane that is defined by the three point located at the mouth, shoulder joint and wrist joint. The system was tested with the swivel angle prediction used with the admittance control, compared to admittance control alone. A significant reduction in the interaction energy was achieved when the prediction was turned on. The algorithm is simple to implement and is effective. This algorithm can be used in motion tracking to decrease the interaction energy required to run the device, or in motion planning where the end effector trajectory can be planned to achieve a particular goal and the redundant space will follow a natural path. This is very advantages for rehabilitation, where the patient needs to relearn natural motions.

EMG Control EMG control takes the myosignals read with surface electromyography to predict the muscle's contraction and ultimately the motion of the arm. There is an inherent delay from when the nerve activates the muscle and when the muscle actually begins to contract. During this time delay we can read the signal and make predictions on how much force the muscle will generate. When using this algorithm the gains in the system can be increased. This controller uses a Hill based lumped parameter systems engineering approach to model the behavior of the muscle. This system has nine independent parameter per muscle that need to be tuned for each person that uses the device. The model is nonlinear and has a large parameter space so a genetic algorithm is used to tune the parameters for each person. The algorithm does not guarantee convergence to the the global minimum and there is no way to know how far you are from the minimum. The results from testing the control scheme showed that for two subjects the system worked very well, one it made control worse and for the last subject the control showed no difference with or without it turned on. The results showed that the gain in the system can be increased with this method, however due to the nature of the parameter fitting algorithm there is no guarantee that the model will fit a particular person. Additionally long setup times for the current electrode placement method would be undesirable in a disable population.

Future Work: The methods tested here have shown great promise in development of a device that can be used for rehabilitation. The main limitation of the methods is a reduction in the bandwidth of the arm motion when using the system. This implies that the device is applying kinematic and dynamic constraints on the user's arm when they are trying to move. Characterizing how much the device is constraining the motion will be an important step in understanding how to improve the preformance.

This can be achieved by using a motion capture system and preform tasks with and without the exoskeleton system then compare the trajectories.

It is likely that misalignment between the user and the device plays an important role in creating these constraints on the arm. With the force sensors on the device it is easy to measure forces in the null space of the device as the user is moving. By purposefully adjusting the height and width of the exoskeleton so that it does not align with the user then measure the magnitude of the force in the null space, a sensitivity to misalignment can be inferred. One must be careful when performing a test like this so that large forces on the user due to induced misalignment forces are not created.

The force sensors on the device give us a lot of information about the interaction of the user and the device, however there are many DoF on the sensors that are redundant, or are in the null space of the device. It would be interesting to map out what signals are required for control of the device and what signals are unneeded. The force sensors represent a significant cost in the system and reducing the number of degrees of freedom that the force sensors read could potential save cost.

The current system has the ability to do bilateral teleoperation which to the best of my knowledge is unique for rehabilitation robots. The device is currently in clinical trials to test this mode of operation for stroke rehabilitation. There is great potential in this and other systems like it, but there is also much work left before their full potential can be realized.

BIBLIOGRAPHY

[1] Marjan A.Admiraal, Martijn J.M.A.M. Kusters, and Stan C.A.M. Gielen. Modeling kinematics and dynamics of human arm movements. *Motor Control*, 8(3):312–338, 2004.

[2] Norman I. Badler and Deepak Tolani. Real-time inverse kinematics of the human arm. *Presence*, 5(4):393–401, 1996.

[3] P. Baerlocher and R. Boulic. Task-priority formulation for the kinematic control of highly redundant articulated structures. In *Proceedings of the 1998 IEEE/RJS Intl. Conference on Intelligent Robots and Systems*, pages 323–329, 1998.

[4] Samuel R. Buss. Introduction to inverse kinematics with jacobian transpose, pseudoinverse and damped least squares methods. 2004.

[5] Samuel R. Buss and Jin-Su Kim. Selectively damped least squares for inverse kinematics. *journal of graphics, gpu, and game tools*, 10(3):37–49, 2005.

[6] P. R. Cavanagh and P. V. Komi. Electromechanical delay in human skeletal muscle under concentric and eccentric conditions. *Applied Physiology*, 42:159–163, 1979.

[7] S. Chiaverini. Singularity-robust task-priority redundancy resolution for realtime kinematic control of robot manipulators. *IEEE Trans Robotics Automat 13*, pages 398–410, 1997.

[8] W. J. Chung and Y. Youm. Null torque-based dynamic control for kinematically redundant manipulators. *Journal of Robotic Systems*, 10(6):811–833, 1993.

[9] Winstein CJ, Wing AM, and Whitall J. Motor control and learning principles for rehabilitation for rehabilitation of upper limb movements after brain injury. *In: Boller F, Grafman J, Robertson IH, editors. Handbook of neuropsychology. The Netherlands: North Holland*, 9:77–137, 2003.

[10] General Electric Company. Exoskeleton prototype project, final report on phase I. Technical Report S-67-1011, Schenectady, New York, 1966.

[11] General Electric Company. Hardiman I prototype project, special interim study. Technical Report S-68-1060, Schenectady, New York, 1968.

[12] E.S. Conkur and R. Buckingham. Manoeuvering highly redundant manipulators. *Robotica 15*, pages 435–447, 1997.

[13] P. Culmer, A. Jackson, M.C. Levesley, J. Savage, R.Richardson, J.A. Cozens, and B.B Bhakta. An admittance control scheme for a robotic upper-limb stroke rehabilitation system. In *Precedings of the 2005 Engineering in Medicine and Biology 27th Annual Conference*, pages 5081–5084.

[14] PR Culmer, AE Jackson, S Makower, R Richardson, JA Cozens, MC Levesley, and BB Bhakta. A control strategy for upper limb robotic rehabilitation with a dual robot system. *IEEE/ASME transactions on mechantronics*, 15:575–585, 2010.

[15] PR Culmer, AE Jackson, SG Makower, JA Cozens, MC Levesley, M Mon-Williams, and BB Bhakta. A novel robotic system for quantifying arm kinematics and kinetics: description and evaluation in therapist-assisted passive arm movements post-stroke. *Journal of Neuroscience Methods*, 197:259–269, 2011.

[16] J. P. Donoghue. Connecting cortex to machines: Recent advances in brain interfaces. *Nature Neuroscience (suppl.)*, 5:1086–1088, 2002.

[17] Brian A. Garner and Marcus G. Pandy. A kinematic model of the upper limb based on the visible human project (VHP) image dataset. *Computer Methods in Biomechanics and Biomedical Engineering*, 2:107–124, 1999.

[18] Brian A. Garner and Marcus G. Pandy. The obstacle-set method for representing muscle paths in musculoskeletal models. *Computer Methods in Biomechanics and Biomedical Engineering*, 3:1–30, 2000.

[19] Brian A. Garner and Marcus G. Pandy. Musculoskeletal model of the upper limb based on the visible human male dataset. *Computer Methods in Biomechanics and Biomedical Engineering*, 4:93–126, 2001.

[20] C.C.A.M. Gielen, E. J. Vrijenhoek, T. Flash, and S.F.W. Neggers. Arm position constraints during pointing and reaching in 3-d space. *Journal of Neurophysiology*, 78(2):660–673, 1997.

[21] C.C.A.M. Gielen, E. J. Vrijenhoek, T. Flash, and S.F.W. Neggers. Review of models for the generation of multi-joint movements in 3-d. *Advances in experimental medicine and biology, Progress in Motor Control*, 629:523–550, 2009.

[22] R. A. R. C. Gopura and Kazuo Kiguchi. Mechanical design of active upper-limb exoskeleton robots: State-of-the-art and design difficulties. In *Proceedings of the IEEE 11th International Conference on Rehabilitation Robotics*, pages 178–187, Kyoto International Conference Center, Japan, June 2009.

[23] Helene Grea, Michel Desmurget, and Claude Prablanc. Postural invariance in three-dimensional reaching and grasping movements. *Exp Brain Res*, 134:155–162, 2000.

[24] Erico Guizzo and Harry Goldstein. The rise of the body bots. *IEEE Spectrum*, 42(10):42–48, October 2005.

[25] Jiping He, E.J.Koeneman, R.S.Schultz, D.E.Herring, John Wanberg, H.Huang, T.Sugar, R.Herman, and J.B.Koeneman. Rupert: a device for robotic upper extremity repetitive therapy. In *Proceedings of the 2005 IEEE Engineering in Medicine and Biology 27th Annual Conference, September 1-4, 2005*, Shanghai, China, Sept 1 - 4 2005.

[26] Jiping He, E.J.Koeneman, R.S.Schultz, H.Huang, John Wanberg, D.E.Herring, T.Sugar, R.Herman, and J.B.Koeneman. Design of a robotic upper extremity repetitive therapy device. In *Proceedings of the 2005 IEEE 9th International Conference on Rehabilitation Robotics*, Chicago, IL, USA, June 28 - July 1 2005.

[27] A. V. Hill. The heat of shortening and the dynamics of muscle. *The royal society of london. Series B, Biological Science*, 126(843):136–195, 1938.

[28] Ioannis Iossifidis and Axel Steinhage. Controlling a redundant robot arm by means of a haptic sensor. In *Proceedings of ROBOTIK 2002, Leistungsstand - Anwendungen - Visionen*, pages 269–274, 2002.

[29] AE Jackson, AE PR Culmer, MC Levesley, JA Cozens, SG Makower, and BB Bhakta. Effector force requirements to enable robotic systems to provide assisted exercise in people with upper limb impairment after stroke. In *IEEE Int Conf Rehabil Robot*, pages 1–6, 2011.

[30] AE Jackson, RJ Holt, PR Culmer, SG Makower, MC Levesley, RC Richardson, JA Cozens, MM Williams, and BB Bhakta. Dual robot system for upper after stroke: the design limb rehabilitation process. *Proceedings of the Institution of Mechanical Engineers Part C: Journal of Mechanical Engineering Science*, 221:845–857, 2007.

[31] Cauraugh JH and Summers JJ. Motor rehabilitation and brain plasticity after hemiparetic stroke. *Prog Neurobiol*, 73:61–72, 2004.

[32] Cauraugh JH and Summers JJ. Neural plasticity and bilateral movements:a rehabilitation approach for chronic stroke. *Prog Neurobiol*, 75(5):309–320, 2005.

[33] Marcelo Kallmann. Analytical inverse kinematics with body posture control. *Computer Animation and Virtual Worlds*, 2007.

[34] Hee-Jun Kang and Robert A. Freeman. Null space damping method for local joint torque optimization of redundant manipulators. *Journal of Robotic Systems*, 10(2):249–270, 1993.

[35] Tao Kang, Jiping He, and Stephen I. Helms Tillery. Determining natural arm configuration along a reaching trajectory. *Exp Brain Res*, 167(3):352–361, 2005.

[36] H. Kazerooni. The human amplifier technology at the university of california, berkeley. *Robotics and Autonomous Systems*, 19:179–187, 1996.

[37] H. Kazerooni and Ming-Guo Her. The dynamics and control of a haptic interface device. *IEEE Transactions on Robotics and Automation*, 10(4), 1994.

[38] H. Kazerooni and Tanya J. Snyder. Case strudy on haptic devices: Human-induced instability in powered hand controllers. *Journal of Guidance, Control, and Dynamics*, 18(1):108–113, 1995.

[39] H. Kazerooni and R. Steger. The berkeley lower extremity exoskeleton. *Transactions of the ASME Journal of Dynamic Systems, Measurements, and Control*, 128:14–25, 2006.

[40] H. Kazerooni, Ryan Steger, and Lihuna Huang. Hybrid control of the berkeley lower extremity exoskeleton (bleex). *The International Journal of Robotics Research*, (5-6):561–573, 2006.

[41] Hyunchul Kim, Zhi Li, Dejan Milutinovic, and Jacob Rosen. Resolving the redundancy of a seven dof wearable robotic system based on kinematic and dynamic constraint. In *The Proceedings of 2012 IEEE International Conference on Robotics and Automation*, Saint Paul, Minnesota, USA, May 2012.

[42] Hyunchul Kim, Levi Makaio Miller, and Jacob Rosen. Redundancy resolution of a human arm for controlling a seven dof wearable robotic system. In *Proceedings of the IEEE EMBC*, Boston, USA, August 30 September 3 2011.

[43] Charles A. Klein and Bruce E. Blaho. Dexterity measures for the design and control of kinematically redundant manipulators. *The International Journal of Robotics Research*, 6(2):72–83, 1987.

[44] Peter Konrad. *The ABC of EMG: A practical Introduction to Kinesiological Electromyography.* Noraxon INC. USA, April 2005. Version 1.0.

[45] James U. Korein. *A Geometric Investigation of Reach.* The MIT Press, 1985.

[46] Hermano I Krebs, Mark Ferraro, Stephen P Buerger, Miranda J Newbery1, Antonio Makiyama, Michael Sandmann, Daniel Lynch, Bruce T Volpe, and Neville Hogan. Rehabilitation robotics: pilot trial of a spatial extension for mit-manus. *Journal of NeuroEngineering and Rehabilitation*, Oct 2004.

[47] Hermano I Krebs, Neville Hogan, Mindy L. Aisen, and Bruce T. Volpe. Robot-aided neurorehabilitation. *Rehabilitation Engineering, IEEE Transactions on [see also IEEE Trans. on Neural Systems and Rehabilitation*, pages 75–87, 1998.

[48] Francesco Lacquaniti and John F. Soechting. Coordination of arm and wrist motion during a reaching task. *J Neurosci*, 1:399–408, 1982.

[49] Philip Lee, Susanna Wei, Jianmin Zhao, and Norman I. Badler. Strength guided motion. *Computer Graphics*, 24(4):253–262, 1990.

[50] Tzu-Chen Liang and Jing-Sin Liu. An improved trajectory planner for redundant manipulators in constrained workspace. *Journal of Robotic Systems*, 16(6):339–351, 1999.

[51] A.A. Maciejewski and C.A. Klein. Obstacle avoidance for kinematically redundant manipulators in dynamically varying environment. *Int J Robotics Res 4*, pages 109–117, 1985.

[52] Anthony A. Maciejewski. Dealing wit the ill-conditioned equations of motion for articulated figures. *IEEE Computer Graphics and Applications*, pages 63–71, 1990.

[53] S.R Majumdar. *Pneumatic System: Principles and Maintenance.* New Delhi: Tata McGraw-Hill, 1995.

[54] B. J. Makinson. Research and development prototype for machine augmentation of human strength and endurance, hardiman I project. Technical Report S-71-1056, GE Company, Schenectady, New York, 1971.

[55] Walter Maurel. *3D Modeling of the Human Upper Limb Including the Biomechanics of Joints, Muscles amd Soft Tissues.* PhD thesis, Ecole Polytechnique Federale de Lausanne, 1998. These No 1906.

[56] Levi Miller, Hyunchul Kim, and Jacob Rosen. Redundancy and joint limit of a seven degree of freedom upper limb exoskeleton. In *in Proc. of IEEE EMBC 2011*, Boston, Augest 2011.

[57] Levi Makaio Miller. Gravity compensation for a 7 degree of freedom powered upper limb exoskeleton. Master's thesis, University Of Washington, Seattle, Washington, 2006.

[58] Levi Makaio Miller and Jacob Rosen. Comparison of multi-sensor admittance control in joint space and task space for a seven degree of freedom upper limb exoskeleton. In *Proceedings of The 3ed IEEE RAS & EMBS International Conference on Biomedical Robotics and Biomechatronics*, pages 70–75, Tokyo, Japan, September 2010.

[59] R. S. Mosher. Force reflecting electrohydraulic servo manipulator. *Electro-Tech*, 138, 1960.

[60] Richard M. Murray, Zexiang Li, and S. Shankar Sastry. *A Mathematical Introduction to Robotic Manipulation.* CRC Press, 1994.

[61] Y. Nakamura, H. Hanafusa, T. Yoshikawa, and Taskpriority. Task priority based redundancy control of robot manipulators. *Int J Robotics Res 6*, pages 3–15, 1987.

[62] Tobias Nef, Marco Guidali, Verena Klamroth-Marganska, and Robert Riender. Design of a 7 degree-of-freedom upper-limb powered exoskeleton. In *World Congress on Medical Physics and Biomedical Engineering IFMBE*, volume 25/9, Munich, Germany, Sept 2009.

[63] Robert W. Norman and Paavo V. Komi. Electromechanical delay in skeletal muscle under normal movement condition. *Acta Physiol Scand*, 106:241–248, 1979.

[64] Joel C. Perry. *Design and Development of a 7 Degree-of-Freedom Powered Exoskeleton for the Upper Limb.* PhD thesis, University of Washington, Seattle, Wa, 2006.

[65] Joel C. Perry, Janet M. Powell, and Jacob Rosen. Isotropy of an upper limb exoskeleton and the kinematics and dynamics of the human arm. *Applied Bionics and Biomechanics*, 6(2):175–191, June 2009.

[66] Joel C. Perry and Jacob Rosen. Design of a 7 degree-of-freedom upper-limb powered exoskeleton. In *Proceedings of The first IEEE / RAS-EMBS International Conference on Biomedical Robotics and Biomechatronics*, pages 805–810, Pisa, Italy, February 2006.

[67] Joel C. Perry, Jacob Rosen, and Stephen Burns. Upper-limb powered exoskeleton design. *IEEE/ASME Transactions on Mechatronics*, 12(4):408–417, 2007.

[68] David J. Reinkensmeyer, Eric Wolbrecht, and James Bobrow. A computational model of human-robot load sharing during robot-assisted arm movement training after stroke. In *Proceedings of the 29th Annual International Conference of the IEEE EMBS*, Lyon, France, August 2007.

[69] J. M. Ritchie and D. R. Wilkie. The dynamics of muscular contraction. *The Journal of Physiology*, 143(1):104–113, 1958.

[70] Nudo RJ. Role of cortical plasticity in motor recovery after stroke. *Journal of Neurologic Physical Therapy*, 22:61–67, 1998.

[71] Nudo RJ. Recovery after damage to motor cortical areas. *Journal of Neurologic Physical Therapy*, 9:740–747, 1999.

[72] R.G. Roberts and A.A. Maciejewski. Singularities, stable surface, and the repeatable behavior of kinematically redundant manipulators. *Int J Robotics Res 13*, pages 70–81, 1994.

[73] Jacob Rosen, Moshe Brand, Moshe B. Fuchs, and Mircea Arcan. A myosignal-based powered exoskeleton system. *IEEE Transactions on System, Man, and Cybernetics - Part A: Systems and Humans*, 31(3):210–222, 2001.

[74] Jacob Rosen, Moshe B Fuchs, and Mircea Arcan. Performance of hill-type and neural network muscle models - toward a myosignal-based exoskeleton. *Computer and Biomedical Research*, 32:415–439, 1999.

[75] Jacob Rosen and Joel C. Perry. Upper limb powered exoskeleton. *International Journal of Humanoid Robotics*, 4(3):529–548, 2007.

[76] Jacob Rosen, Joel C. Perry, Nathan Manning, Stephen Burns, and Blake Hannaford. The human arm kinematics and dynamics during daily activities - towards a 7 dof upper limb powered exoskeleton. In *Proceedings of the IEEE International Conference on Advanced Robotics*, pages 532–539, 2005.

[77] Homayoun Seraji. Adaptive admittance control: An approach to explicit force control in compliant motion. In *Proceedings of the IEEE International Conference on Robotics and Automation*, pages 2705–2712, 1994.

[78] Tanya J. Snyder and H. Kazerooni. A novel material handling system. In *Proceedings of the 1996 IEEE International Conference on Robotics and Automation*, pages 1147–1152, 1996.

[79] J.F. Soechting, C.A. Buneo, U. Herrmann, and M. Flanders. Moving effortlessly in three dimensions: Does donders' law apply to arm movement? *Journal of Neuroscience*, 15:6271–6280, 1995.

[80] Deepak Tolani, Ambarish Goswami, and Norman I. Badler. Ral-time inverse kinematics techniques for anthropomorphic limbs. *Graphical Models*, 62:353–388, 2000.

[81] N.G. Tsagarakis and Darwin G. Caldwell. Development and control of a 'soft-actuated' exoskeleton for use in physiotherapy and training. *Autonomous Robots*, 15:21–33, 2003.

[82] Y. Uno, M. Kawato, and R. Suzuki. Formation and control of optimal trajectory in human multi joint arm movement. *Bioligical Cybernetics*, 61(2):89–101, 1989.

[83] Xuguang Wang. A behavior-based inverse kinematics algorithm to predict arm prehension posture for computer-aided ergonomic evaluation. *Journal of Biomechanics*, 32:453–460, 1999.

[84] D. R. Wilkie. The mechanical properties of muscle. *British Medical Bulletin*, 12(3):177–182, 1956.

[85] Jack Winters. Hill-based muscle models: a systems engineering perspective. In *Multiple Muscle Systems: Biomechanics and Movement Organization*, pages 69–93. 1990.

[86] Eric T. Wolbrecht, Vicky Chan, Vu Le, Steven C. Cramer, David J. Reinkensmeyer, and James E. Bobrow. Real-time computer modeling of weakness following stroke optimizes robotic assistance for movement therapy. In *Proceedings of*

the 3rd International IEEE EMBS Conference on Neural Engineering, Hawaii, USA, May 2007.

[87] Gao Yan. Decomposible closed form inverse kinematics for reconfigurable robots using product-of-exponentials formula. Master's thesis, Nanyang Technological University, 2000.

[88] C-J Yang, J-F Zhang, Y Chen, Y-M Dong, and Y Zhang. A review of exoskeleton-type systems and their key technologies. *Proceedings of the Institution of Mechanical Engineers; Part C; Journal of Mechanical Engineering Science*, 222(8):1599–1612, March 2008.

[89] Feng Yang and Xiugan Yuan. An inverse kinematical algorithm for human arm movement with comfort level taken into account. In *Proceedings of 2003 IEEE Conference on Control Applications*, volume 2, 2003.

[90] Xudong Zhang and Don B. Chaffin. The effects of speed variation on joint kinematics during multisegment reaching movements. *human movement science*, 18:741–757, 1999.

[91] Adam Zoss, H. Kazerooni, and Andrew Chu. On the mechanical design of the berkeley lower extremity exoskeleton (bleex). In *IEEE/RSJ International Conference on Intelligent Robots and Systems*, Alberta, Canada, July 2005.

[92] Adam B Zoss, H. Kazerooni, and Andrew Chu. Biomechanical design of the berkeley lower extremity exoskeleton (bleex). *IEEE/ASME Transactions on Machatronics*, 11(2), 2006.

Appendix A

EXOSKELETON PROPERTIES

Table A.1: Initial Joint intersection locations (m)

$$P_s = [\ 0,\ 0,\ 0\ ]$$
$$P_{e_0} = [\ 0,\ 0,\ -0.3036\ ]$$
$$P_{w_0} = [\ 0,\ 0,\ -0.5806\ ]$$

Table A.2: Joint rotation axes for the right and left exoskeleton arms

Right Arm	**Left Arm**
$\vec{\omega}_{R1} = [\ 0.7071, -0.5213, -0.4777\ ]$	$\vec{\omega}_{L1} = [\ 0.7071,\ 0.5213,\ 0.4777\ ]$
$\vec{\omega}_{R2} = [\ 0.5934,\ 0.8089,\ 0\ ]$	$\vec{\omega}_{L2} = [\ 0.5934, -0.8089,\ 0\ ]$
$\vec{\omega}_{R3} = [\ 0,\ 0,\ 1\ ]$	$\vec{\omega}_{L3} = [\ 0,\ 0,\ -1\ ]$
$\vec{\omega}_{R4} = [\ 1,\ 0,\ 0\ ]$	$\vec{\omega}_{L4} = [\ 1,\ 0,\ 0\ ]$
$\vec{\omega}_{R5} = [\ 0,\ 0,\ 1\ ]$	$\vec{\omega}_{L5} = [\ 0,\ 0,\ -1\ ]$
$\vec{\omega}_{R6} = [\ 0,\ 1,\ 0\ ]$	$\vec{\omega}_{L6} = [\ 0,\ -1,\ 0\ ]$
$\vec{\omega}_{R7} = [\ 1,\ 0,\ 0\ ]$	$\vec{\omega}_{L7} = [\ 1,\ 0,\ 0\ ]$

Table A.3: Exoskeleton properties w.r.t the global frame, from Solidworks

Joint	1	2	3	4	5	6	7
Mass (Kg)	3.44	1.64	.69	1.25	1.81	.18	.52
Center Of Mass x (m)	.3114	.0487	.0936	.0123	-.0221	.0368	.0251
Center Of Mass y (m)	-.0647	.0385	-.0103	-.0381	-.0526	-.0415	.0555
Center Of Mass z (m)	-.1001	-.1083	-.1853	-.3604	-.4528	-.589	-.6662
Motor Gear Ratio	1	1	1	1	3.7	5.8	5.8
Capstan Radius (mm)	10.8	10.8	10.8	8.5	7.4176	4.7185	4.7185
Cable Radius (mm)	1	1	.705	1	.375	.375	.375
Pulley Radius cable 1 (mm)	35.5						
Pulley Radius cable 2 (mm)	37.481	35.5					
Pulley Radius cable 3 (mm)	38.494	38.494	107.893				
Pulley Radius cable 4 (mm)	37.989	37.989	107.388	28.575			
Pulley Radius cable 5 (mm)					63.5		
Pulley Radius cable 6 (mm)						23.4	
Pulley Radius cable 7 (mm)						23.4	23.4
Routing Direction cable 1	+1						
Routing Direction cable 2	-1	+1					
Routing Direction cable 3	-1	-1	-1				
Routing Direction cable 4	+1	+1	+1	-1			
Routing Direction cable 5					+1		
Routing Direction cable 6						+1	
Routing Direction cable 7						+1	-1
Pulley Reduction (mm/mm)	$\frac{21.844}{85}$	$\frac{21.844}{83}$	1	$\frac{21.844}{94}$	1	1	1

Appendix B

ANGLE OF AN ELLIPSE'S TANGENT LINE

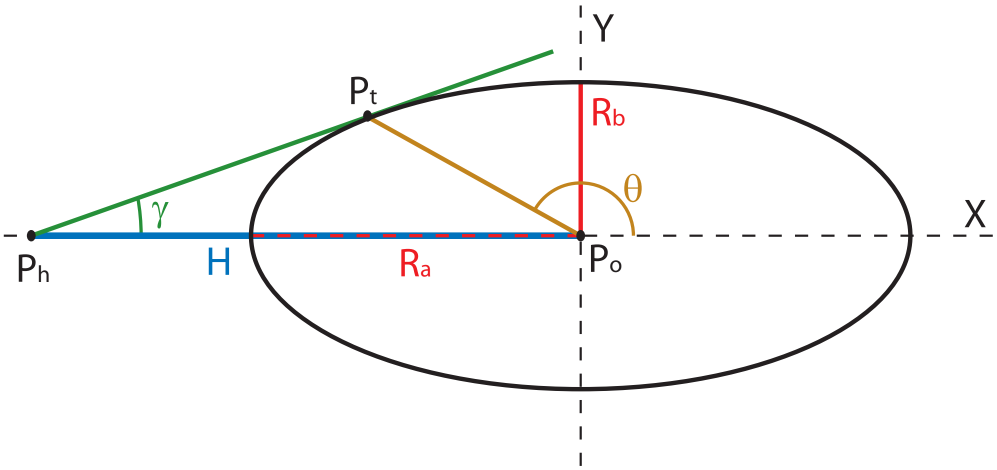

Figure B.1: An ellipse centered at point Po with major and minor axis equal to R_a and R_b. The line that passes through P_h and P_t is tangent to the ellipse. The angle γ is a function of the length of R_a, R_b and H

Given an ellipse centered at P_o, and the point P_h, which is aligned with one of the principle axis of the ellipse, the angle γ between the vectors $(P_h - P_o)$ and $(P_h - P_t)$, where P_t is the point on the ellipse that makes the line from P_h to P_t tangent, is:

$$\gamma = \pm \arctan\left(\sqrt{\frac{R_b^2}{H^2 - R_a^2}}\right) \tag{B.1}$$

Where $H = ||P_h - P_o||$, is the distance between P_h and the center of the ellipse, R_a is the length of the (major or minor) axis of the ellipse that is colinear with the line from P_h to P_o, and R_b is the length of the other axis.

Proof. Begin be assigning a coordinate frame to the system with the origin at P_o, the x axis equal to the vector $(P_o - P_h)$ and the y axis following the right hand rule. Then any point on the ellipse can be parameterized as a function of θ, the angle of rotation measured from the x axis (Fig. B.1).

$$\begin{aligned} E_x &= R_a \cos(\theta) \qquad \text{(B.2)} \\ E_y &= R_b \sin(\theta) \qquad \text{(B.3)} \end{aligned}$$

Next, solve for the angle of θ that parameterizes the point P_t. This is done by first calculating the slope of the tangent line for any point on the ellipse.

$$\frac{\dot{E}_y}{\dot{E}_x} = \frac{R_b \cos(\theta)}{-R_a \sin(\theta)} \qquad \text{(B.4)}$$

Then calculate the slope of the line going from the P_h (which is equal to $[-H, 0]$ in the defined coordinate frame) to any point on the ellipse.

$$\frac{\Delta y}{\Delta x} = \frac{E_y - P_{h_y}}{E_x - P_{h_x}} = \frac{R_b \sin(\theta) - 0}{R_a \cos(\theta) + H} \qquad \text{(B.5)}$$

Finally set (B.4) and (B.5) equal to one another

$$\frac{R_b \cos(\theta)}{-R_a \sin(\theta)} = \frac{R_b \sin(\theta)}{R_a \cos(\theta) + H} \qquad \text{(B.6)}$$

and solve for θ

$$\begin{aligned} R_a \cos^2(\theta) + H \cos(\theta) &= -R_a \sin^2(\theta) \qquad \text{(B.7)} \\ H \cos(\theta) &= -R_a \left[\sin^2(\theta) + \cos^2(\theta)\right] \qquad \text{(B.8)} \\ \theta &= \pm \arccos\left(\frac{-R_a}{H}\right) \qquad \text{(B.9)} \end{aligned}$$

The angle γ is equal to the arctan of the slope of the line calculated in (B.4)

$$\gamma = \arctan\left(\frac{R_b\cos(\theta)}{-R_a\sin(\theta)}\right) \tag{B.10}$$

Substitute θ with (B.9)

$$\begin{aligned}
\gamma &= \arctan\left(\frac{R_b\cos\left[\pm\arccos\left(\frac{-R_a}{H}\right)\right]}{-R_a\sin\left[\pm\arccos\left(\frac{-R_a}{H}\right)\right]}\right) && \text{(B.11)}\\
&= \arctan\left(\frac{\frac{-R_bR_a}{H}}{\pm R_a\sqrt{1-\left(\frac{R_a}{H}\right)^2}}\right) && \text{(B.12)}\\
&= \pm\arctan\left(\frac{R_b}{H\sqrt{1-\left(\frac{R_a}{H}\right)^2}}\right) && \text{(B.13)}\\
&= \pm\arctan\left(\sqrt{\frac{R_b^2}{H^2-R_a^2}}\right) && \text{(B.14)}
\end{aligned}$$

Equation (B.14) is equal to (B.1) as desired. $\square$

Appendix C

INVERSE KINEMATICS: SUBPROBLEM ONE

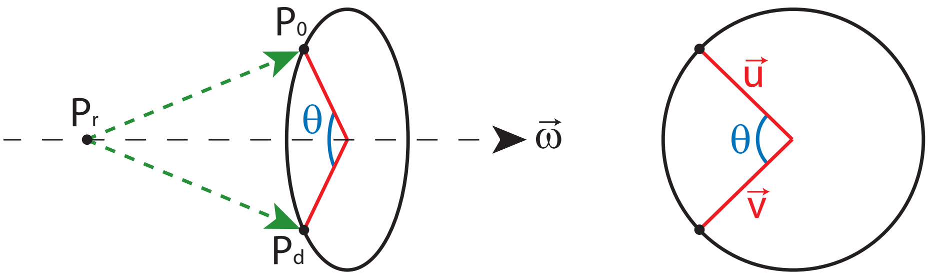

Figure C.1: The initial point P_0 rotated around the axis $\vec{\omega}$ by an angle of θ to end at P_d the desired finial point. The vectors $\vec{u}$ and $\vec{v}$ are the projection of $(P_0 - P_r)$ and $(P_d - P_r)$ onto a plane normal to $\vec{\omega}$.

Given the transformation matrix $T(\theta)$ Find θ such that:

$$T(\theta)P_0 = P_d \tag{C.1}$$

This corresponds to rotating an initial point P_0 about a given axis until it is coincident with P_d the desired final position (Fig. C.1). The solution to this problem is:

$$\theta = \arctan 2\left[\vec{\omega}^T(\vec{u} \times \vec{v}), \vec{u}^T\vec{v}\right] \tag{C.2}$$

Where $\vec{\omega}$ is the vector pointing in the direction of the rotation axis, P_r is any point that the axis passes through, and $\vec{u}$ and $\vec{v}$ are the projections of $(P_0 - P_r)$ and $(P_d - P_r)$

onto the plane normal to $\vec{\omega}$ and are equal to:

$$\vec{u} = (P_0 - P_r) - \vec{\omega}\vec{\omega}^T(P_0 - P_r) \tag{C.3}$$

$$\vec{v} = (P_d - P_r) - \vec{\omega}\vec{\omega}^T(P_d - P_r) \tag{C.4}$$

This problem will have solution when:

$$\vec{\omega}^T(P_0 - P_r) = \vec{\omega}^T(P_d - P_r) \qquad \text{and} \qquad ||\vec{u}|| = ||\vec{v}|| \tag{C.5}$$

If the above conditions are satisfied and $||\vec{u}|| = 0$ Then there will be an infinite number of solution as P_0 and P_d are both on the axis of rotation and are coincident. For the derivation refer to [60, 87]

Appendix D

INVERSE KINEMATICS: SUBPROBLEM TWO

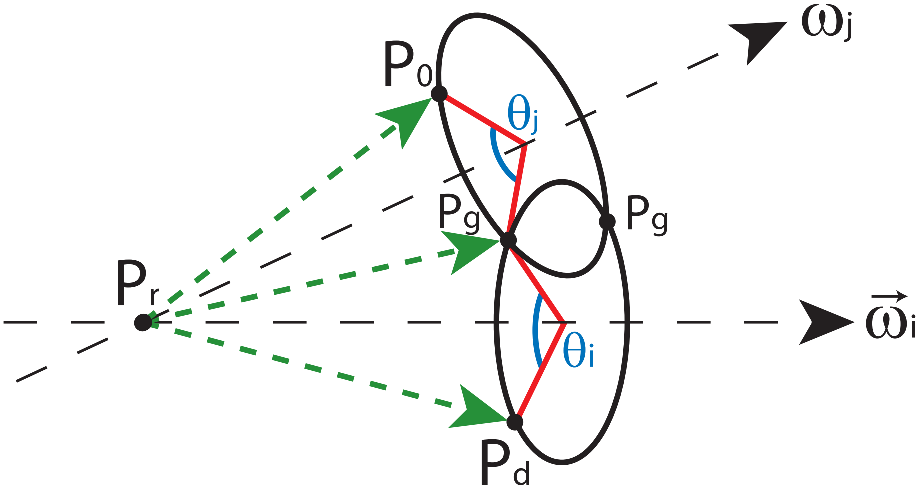

Figure D.1: The initial point P_0 rotated around the axis $\vec{\omega_j}$ by an angle of θ_j to the intermediate point P_g, then rotated about the axis $\vec{\omega}_i$ by θ_i to end at P_d the desired finial point. The two axes intersect at the point P_r. There are two possible solutions for P_g representing the intersections of the circles traced by P_0 around $\vec{\omega}_j$ and P_d around $\vec{\omega}_i$

Given the transformation matrix $T_i(\theta_i)T_j(\theta_j)$ where the rotation axis of T_i and T_j intersect at the point P_r, find θ_i and θ_j such that:

$$T_i(\theta_i)T_j(\theta_j)P_0 \quad = \quad P_d \tag{D.1}$$

This corresponds to rotating an initial point P_0 first about $\vec{\omega}_j$, the rotation axis of T_j, by θ_j then about $\vec{\omega}_i$, the rotation axis of T_i, by θ_i, so that the final location of the rotated point is coincident with P_d the desired final position. The solution to this problem is calculated by first finding P_g, the intersection point of the circles traced by rotating P_0 around $\vec{\omega}_j$ and P_d around $\vec{\omega}_i$ (Fig. D.1).

$$\begin{aligned} P_g &= \alpha\vec{\omega}_i + \beta\vec{\omega}_j \pm \sqrt{\gamma}(\vec{\omega}_i \times \vec{\omega}_j) + P_r \quad (D.2) \\ \alpha &= \frac{(\vec{\omega}_i^T\vec{\omega}_j)\vec{\omega}_j^T(P_0 - P_r) - \vec{\omega}_i^T(P_d - P_r)}{(\vec{\omega}_i^T\vec{\omega}_j)^2 - 1} \quad (D.3) \\ \beta &= \frac{(\vec{\omega}_i^T\vec{\omega}_j)\vec{\omega}_i^T(P_d - P_r) - \vec{\omega}_j^T(P_0 - P_r)}{(\vec{\omega}_i^T\vec{\omega}_j)^2 - 1} \quad (D.4) \\ \gamma &= \frac{||(P_0 - P_r)||^2 - \alpha^2 - \beta^2 - 2\alpha\beta\vec{\omega}_i^T\vec{\omega}_j}{||\vec{\omega}_i \times \vec{\omega}_j||^2} \quad (D.5) \end{aligned}$$

There may be zero, one or two real solution for P_g depending on the value of γ. If solutions exist, then θ_i and θ_j can be found with subproblem one (Appendix: C).

$$\begin{aligned} T_i(-\theta_i)P_d &= P_g \quad (D.6) \\ T_j(\theta_j)P_0 &= P_g \quad (D.7) \end{aligned}$$

For the derivation of this solution refer to [60, 87].

Appendix E

FORWARD KINEMATICS

E.1 Right Side

$$CC_R = \begin{bmatrix} & & & 0 \\ \vec{\omega}_{R1} & \vec{\omega}_{R2} & (\vec{\omega}_{R1} \times \vec{\omega}_{R1}) & 0 \\ & & & 0 \\ 0 & 0 & 0 & 1 \end{bmatrix} \tag{E.1}$$

$$T_{R1} = CC_R \begin{bmatrix} 1 & 0 & 0 & 0 \\ 0 & \cos(\theta_{R1}(t)) & -\sin(\theta_{R1}(t)) & 0 \\ 0 & \sin(\theta_{R1}(t)) & \cos(\theta_{R1}(t)) & 0 \\ 0 & 0 & 0 & 1 \end{bmatrix} CC_R^T \tag{E.2}$$

$$T_{R2} = CC_R \begin{bmatrix} \cos(\theta_{R2}(t)) & 0 & \sin(\theta_{R2}(t)) & 0 \\ 0 & 1 & 0 & 0 \\ -\sin(\theta_{R2}(t)) & 0 & \cos(\theta_{R2}(t)) & 0 \\ 0 & 0 & 0 & 1 \end{bmatrix} CC_R^T \tag{E.3}$$

$$T_{R3} = \begin{bmatrix} \cos(\theta_{R3}(t)) & -\sin(\theta_{R3}(t)) & 0 & 0 \\ \sin(\theta_{R3}(t)) & \cos(\theta_{R3}(t)) & 0 & 0 \\ 0 & 0 & 1 & 0 \\ 0 & 0 & 0 & 1 \end{bmatrix} \tag{E.4}$$

$$T_{R4} \quad = \quad \begin{bmatrix} 1 & 0 & 0 & 0 \\ 0 & \cos(\theta_{R4}(t)) & -\sin(\theta_{R4}(t)) & -U\sin(\theta_{R4}) \\ 0 & \sin(\theta_{R4}(t)) & \cos(\theta_{R4}(t)) & U(\cos(\theta_{R4}(t))-1) \\ 0 & 0 & 0 & 1 \end{bmatrix} \tag{E.5}$$

$$T_{R5} \quad = \quad \begin{bmatrix} \cos(\theta_{R5}(t)) & -\sin(\theta_{R5}(t)) & 0 & 0 \\ \sin(\theta_{R5}(t)) & \cos(\theta_{R5}(t)) & 0 & 0 \\ 0 & 0 & 1 & 0 \\ 0 & 0 & 0 & 1 \end{bmatrix} \tag{E.6}$$

$$T_{R6} \quad = \quad \begin{bmatrix} \cos(\theta_{R6}(t)) & 0 & \sin(\theta_{R6}(t)) & (U+L)\sin(\theta_{R6}(t)) \\ 0 & 1 & 0 & 0 \\ -\sin(\theta_{R6}(t)) & 0 & \cos(\theta_{R6}(t)) & (U+L)(cos(\theta_{R6}(t))-1) \\ 0 & 0 & 0 & 1 \end{bmatrix} \tag{E.7}$$

$$T_{R7} \quad = \quad \begin{bmatrix} 1 & 0 & 0 & 0 \\ 0 & \cos(\theta_{R7}(t)) & \sin(\theta_{R7}(t)) & -(U+L)\sin(\theta_4) \\ 0 & \sin(\theta_{R7}(t)) & \cos(\theta_{R7}(t)) & (U+L)(\cos(\theta_{R7}(t))-1) \\ 0 & 0 & 0 & 1 \end{bmatrix} \tag{E.8}$$

E.2 Left Side

$$CC_L \quad = \quad \begin{bmatrix} \vec{\omega}_{L1} & \vec{\omega}_{L2} & (\vec{\omega}_{L1} \times \vec{\omega}_{L1}) & \begin{matrix} 0 \\ 0 \\ 0 \end{matrix} \\ 0 & 0 & 0 & 1 \end{bmatrix} \tag{E.9}$$

$$T_{L1} = CC_L \begin{bmatrix} 1 & 0 & 0 & 0 \\ 0 & \cos(\theta_{L1}(t)) & -\sin(\theta_{L1}(t)) & 0 \\ 0 & \sin(\theta_{L1}(t)) & \cos(\theta_{L1}(t)) & 0 \\ 0 & 0 & 0 & 1 \end{bmatrix} CC_L^T \tag{E.10}$$

$$T_{L2} = CC_L \begin{bmatrix} \cos(\theta_{L2}(t)) & 0 & -\sin(\theta_{L2}(t)) & 0 \\ 0 & 1 & 0 & 0 \\ \sin(\theta_{L2}(t)) & 0 & \cos(\theta_{L2}(t)) & 0 \\ 0 & 0 & 0 & 1 \end{bmatrix} CC_L^T \tag{E.11}$$

$$T_{L3} = \begin{bmatrix} \cos(\theta_{L3}(t)) & \sin(\theta_{L3}(t)) & 0 & 0 \\ -\sin(\theta_{L3}(t)) & \cos(\theta_{L3}(t)) & 0 & 0 \\ 0 & 0 & 1 & 0 \\ 0 & 0 & 0 & 1 \end{bmatrix} \tag{E.12}$$

$$T_{L4} = \begin{bmatrix} 1 & 0 & 0 & 0 \\ 0 & \cos(\theta_{L4}(t)) & -\sin(\theta_{L4}(t)) & -U\sin(\theta_{L4}) \\ 0 & \sin(\theta_{L4}(t)) & \cos(\theta_{L4}(t)) & U(\cos(\theta_{L4}(t))-1) \\ 0 & 0 & 0 & 1 \end{bmatrix} \tag{E.13}$$

$$T_{L5} = \begin{bmatrix} \cos(\theta_{L5}(t)) & \sin(\theta_{L5}(t)) & 0 & 0 \\ -\sin(\theta_{L5}(t)) & \cos(\theta_{L5}(t)) & 0 & 0 \\ 0 & 0 & 1 & 0 \\ 0 & 0 & 0 & 1 \end{bmatrix} \tag{E.14}$$

$$T_{L6} = \begin{bmatrix} \cos(\theta_{L6}(t)) & 0 & -\sin(\theta_{L6}(t)) & -(U+L)\sin(\theta_{L6}(t)) \\ 0 & 1 & 0 & 0 \\ \sin(\theta_{L6}(t)) & 0 & \cos(\theta_{L6}(t)) & (U+L)(cos(\theta_{L6}(t))-1) \\ 0 & 0 & 0 & 1 \end{bmatrix} \tag{E.15}$$

$$T_{L7} = \begin{bmatrix} 1 & 0 & 0 & 0 \\ 0 & \cos(\theta_{L7}(t)) & \sin(\theta_{L7}(t)) & -(U+L)\sin(\theta_4) \\ 0 & \sin(\theta_{L7}(t)) & \cos(\theta_{L7}(t)) & (U+L)(\cos(\theta_{L7}(t))-1) \\ 0 & 0 & 0 & 1 \end{bmatrix} \tag{E.16}$$

Appendix F

INVERSE KINEMATICS

F.1 Right Side

Theta 4

$$\theta_{R4} = \pi \pm \arccos\left(\frac{L^2 + U^2 - ||P_w - P_s||^2}{2LU}\right) \tag{F.1}$$

Theta 1 and Theta 2

$P_0 = P_{e_0}$ and $P_d = P_e(\phi)$

$$\theta_{R1} = -atan2\left(\mp P_d \cdot \vec{\omega}_{R2}\ ,\ \mp P_d \cdot (\vec{\omega}_{R1} \times \vec{\omega}_{R2})\right) \tag{F.2}$$

$$\theta_{R2} = atan2\left(-P_d \cdot \vec{\omega}_{R1}\ ,\ \pm\sqrt{U^2 - (P_d \cdot \vec{\omega}_{R1})^2}\right) + acos(\vec{\omega}_1 \cdot \vec{\omega}_{R3}) - \frac{\pi}{2} \tag{F.3}$$

Theta 3

$P_0 = T_{R4} P_{w_0}$ and $P_d = (T_{R1} T_{R2})^{-1} g_d g_{st}^{-1} P_{w_0}$

$$\theta_{R3} = atan2(-(P_0)_y (P_d)_x\ ,\ (P_0)_y (P_d)_y) \tag{F.4}$$

Theta 5 and Theta 6

$P_0 = P_7$ and $P_d = (T_{R1} T_{R2} T_{R3} T_{R4})^{-1} g_d g_{st}^{-1} P_7$.

$$\theta_{R5} = -atan2(\mp(P_d)_y, \pm(P_d)_x) \tag{F.5}$$

$$\theta_{R6} = atan2\left(-((P_d)_z + U + L), \pm\sqrt{(P_0)_x^2 - ((P_d)_z + U + L)^2}\right) \tag{F.6}$$

Theta 7

$P_0 = P_s$ and $P_d = (T_{R1}T_{R2}T_{R3}T_{R4}T_{R5}T_{R6})^{-1} g_d g_{st}^{-1} P_s$

$$\theta_{R7} = atan2(-(P_d)_y, (P_d)_z + U + L) \tag{F.7}$$

F.2 Left Side

Theta 4

$$\theta_{L4} = \pi \pm \arccos\left(\frac{L^2 + U^2 - ||P_w - P_s||^2}{2LU}\right) \tag{F.8}$$

Theta 1 and Theta 2

$P_0 = P_{e_0}$ and $P_d = P_e(\phi)$

$$\theta_{L1} = -atan2\left(\pm P_d \cdot \vec{\omega}_{L2}\ ,\ \pm P_d \cdot (\vec{\omega}_{L1} \times \vec{\omega}_{L2})\right) \tag{F.9}$$

$$\theta_{L2} = atan2\left(P_d \cdot \vec{\omega}_{L1}\ ,\ \pm\sqrt{U^2 - (P_d \cdot \vec{\omega}_{L1})^2}\right) + acos(\vec{\omega}_{L1} \cdot \vec{\omega}_{L3}) - \frac{\pi}{2} \tag{F.10}$$

Theta 3

$P_0 = T_4 P_{w_0}$ and $P_d = (T_{L1}T_{L2})^{-1} g_d g_{st}^{-1} P_{w_0}$

$$\theta_{L3} = atan2((P_0)_y (P_d)_x\ ,\ (P_0)_y (P_d)_y) \tag{F.11}$$

Theta 5 and Theta 6

$P_0 = P_7$ and $P_d = (T_{L1}T_{L2}T_{L3}T_{L4})^{-1} g_d g_{st}^{-1} P_7$.

$$\theta_{L5} = -atan2(\pm(P_d)_y, \pm(P_d)_x) \tag{F.12}$$

$$\theta_{L6} = atan2\left(((P_d)_z + U + L), \pm\sqrt{(P_0)_x^2 - ((P_d)_z + U + L)^2}\right) \tag{F.13}$$

Theta 7

$P_0 = P_s$ and $P_d = (T_{L1} T_{L2} T_{L3} T_{L4} T_{L5} T_{L6})^{-1} g_d g_{st}^{-1} P_s$

$$\theta_{L7} = atan2(-(P_d)_y, (P_d)_z + U + L) \tag{F.14}$$

VITA

LEVI MAKAIO MILLER

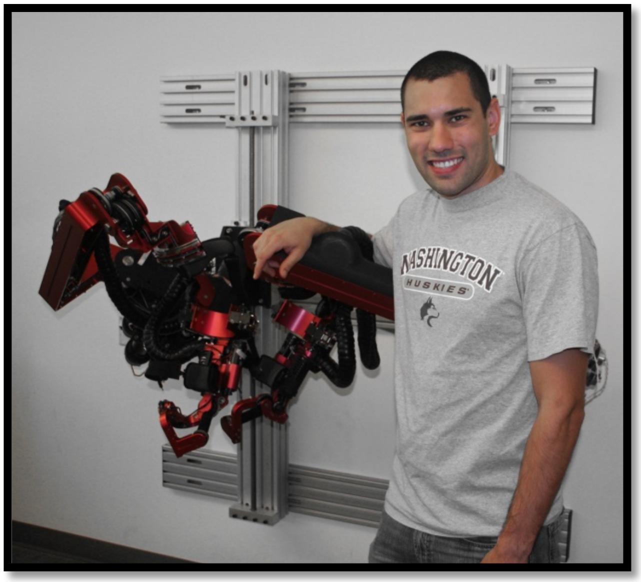

Extensive experience in robotics research in the area of human-centered, wearable and medical robots. Concentrating on the mechanical design of the human machine interface and the development and implementation of control algorithms using haptics, and neural interfaces and for seamless and intuitive integrations between man and machine.

EDUCATION

PhD in Mechanical Engineering 2012

University of Washington, Seattle, Washington

- PhD Dissertation: *Comprehensive Control Strategies for a Seven Degree of Freedom Upper Limb Exoskeleton Targeting Stroke Rehabilitation*
- Focus: Controls and Robotics
- 3.73 GPA
- Expected graduation in December 2011

MS in Mechanical Engineering 2006

University of Washington, Seattle, Washington

- Master's Thesis: *Gravity Compensation for a 7 Degree of Freedom Powered Upper Limb Exoskeleton*
- Focus: Controls and Robotics
- 3.71 GPA

BS in Manufacturing Engineering Technology 2004

Western Washington University, Bellingham, Washington

- Minor: Mathematics
- Minor: Physics
- Graduated Magna Cum Laude
- 3.85 GPA

WORK EXPERIENCE

Robotics Engineer, Carbon Design Group 2011-Present
1414 NE 42nd Street Suite 400, Seattle. Washington, 98105 http://www.carbondesign.com

- Mechanical design
- Systems integration
- Collaborative design integration with multidisciplinary team

Adjunct Professor, Seattle University 2012-Present
901 12th Avenue, Seattle. Washington 98122

- MEGR 372 - Machine Elements II SECTION 1-12SQ

Associate Specialist, Bionics Lab 2008-2011
University of California Santa Cruz, Santa Cruz, California http://bionics.soe.ucsc.edu

- Upper-Limb Exoskeleton EXO-UL7
  - Designed, developed, and implemented the control system to a level that is being used for clinical trials.
  - Delivered device to UC San Francisco for ongoing clinical trials targeting stroke rehabilitation.
  - Integrated haptics and virtual reality with medical robotic technologies for stroke rehabilitation.
  - Researched and developed a controller for motion prediction based on muscle modeling using EMG input signals.
  - Presented research on the human-machine interface at the 2010 IEEE BioRob Conference in Tokyo, Japan.
- LEX Lower-Limb Exoskeleton
  - Implemented initial design concept and performed dynamic simulations.
  - Directed personnel in the creation of the first-generation design.
- Raven 4 Surgical Robot
  - Advised a team and managed resources, resulting in increased collaboration between universities.

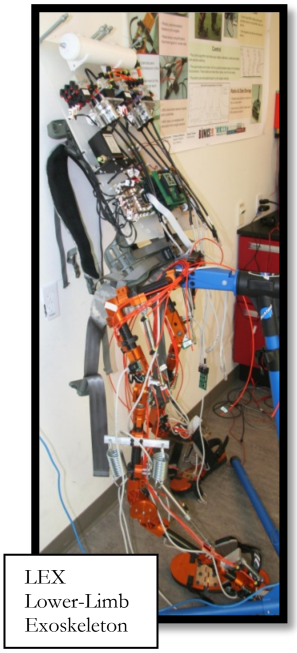

LEX
Lower-Limb
Exoskeleton

Graduate Researcher, Biorobotics Lab 2004-2008
University of Washington, Seattle, Washington http://brl.ee.washington.edu

- Conducted research on robotic dynamics, kinematics, and inverse kinematics.
- Became knowledgeable in human arm mechanics in order to develop control systems for wearable robotics.
- Applied control theory to wearable robotic systems.
- Assisted a team traveling to Simi Valley to test operations of Raven Surgical Robot in a remote and harsh environment.

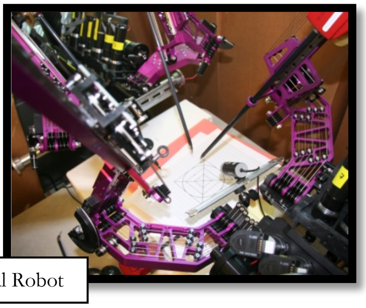

Raven 4 Surgical Robot

SKILLS

- Project and resource management
- Robotic dynamics, kinematics, and inverse kinematics
- Human arm mechanics
- Control theory
- Mechanical design
- Manufacturing
- Design of experiments
- Programming (C, C++, C#)
- Matlab/Simulink
- Mathematica
- CAD (Solidworks, Pro/Engineer, Catia)

Upper-Limb Exoskeleton EXO-UL7

PUBLICATIONS

Levi Makaio Miller, Hyunchul Kim and Jacob Rosen. *Redundancy and Joint Limits of a Seven Degree of Freedom Upper Limb Exoskeleton.* International Conference of the IEEE Engineering in Medicine and Biology Society. August 2011. Boston, Massachusetts.

Hyunchul Kim, **Levi Makaio Miller**, Aimen Al-Refai, Moshe Brand and Jacob Rosen. *Redundancy Resolution of a Human Arm for Controlling a Seven DOF Wearable Robotic System.* International Conference of the IEEE Engineering in Medicine and Biology Society. August 2011. Boston, Massachusetts.

Levi Makaio Miller and Jacob Rosen. *Comparison of Multi-Sensor Admittance Control in Joint Space and Task Space for a Seven Degree of Freedom Upper Limb Exoskeleton.* 3rd IEEE RAS & EMBS International Conference on Biomedical Robotics and Biomechatronics. September 2010. Tokyo, Japan.

H. Hawkeye King, Blake Hannafor, Ka-Wai Kwok, Guang-Zhong Yang, Paul Griffiths, Allison Okamura, Ildar Farkhatdinov, Jee-Hwan Ryu, Ganesh Sankaranarayanan, Venkata Arikatla, Suvranu De, Kotaro Tadano, Kenji Kawashima, Angelika Peer, Thomas Schuß, Martin Buss, **Levi Miller**, Daniel Glozman, Jacob Rosen, and Thomas Low. *Plugfest 2009: Global Interoperability in Telerobotics and Telemedicine.* IEEE International Conference on Robotics and Automation. May 2010. Anchorage, Alaska.

Levi Makaio Miller. *Master Thesis: Gravity Compensation for a 7 Degree of Freedom Powered Upper Limb Exoskeleton.* University of Washington. 2006. Seattle, Washington.

SELECTED PRESS

"Masters of Innovation: Biological Frontiers." Plum TV. January 2011.
(Begins 5 minutes 35 seconds into video.)
http://www.plumtv.com/videos/masters-of-innovation-biological-frontiers

"Robots to Aid Stroke Victims With Physical Therapy." CBS Smart Planet. August 2010.
http://www.smartplanet.com/technology/video/robots-to-aid-stroke-victims-with-physical-therapy-/460398/

"Turbo Powered Physical Therapy." Popular Science. June 2009.
http://www.popsci.com/scitech/article/2009-06/turbo-powered-physical-therapy

PERSONAL INTERESTS

- Playing with my son
- Triathlon competitions
- Marathon and ultra-marathon running
- Cycling
- Playing the Irish tin whistle
- Baking desserts

REFERENCES

References and letters of recommendation available upon request.